Studies of X-ray absorption spectroscopy for functional materials by using multiple scattering theory

January 2016

Akihiro Koide

Graduate School of

Advanced Integration Science

CHIBA UNIVERSITY

(千葉大学審査学位論文)

Studies of X-ray absorption spectroscopy for functional materials by using multiple scattering theory

January 2016

Akihiro Koide

Graduate School of

Advanced Integration Science

CHIBA UNIVERSITY

Contents

Acknowlegement

I would like to express my heartfelt gratitude to Prof. Takashi Fujikawa for his guidance, discussion, and encouragement.

I am deeply indebted to Prof. Takehisa Konishi whose guidance and comments strongly encouraged me to advance my studies.

I sincerely thank Prof. Kaori Niki whose supports proceed with my works.

I deeply thank to Prof. Shuichi Emura for his fruitful discussions and providing experimental data and oppotunities to measure XANES spectra.

I owe a very important debt to Dr. Seiji Sakai, Dr. Shiro Entani and Dr. Yoshihiro Matsumoto whose comments and experimental data made enormous contribution to my works.

I am truly thankful to Prof. Peter Kruger whose advice and useful codes progressed with my works.

I am grateful to Dr. Keisuke Hatada, who was formerly a member of Fujikawa Laboratory in Chiba University. He provided me oppotunities to visit University of Rennes 1 in France, and to receive a seminar in Czech Republic.

I wish to thank Kei Takahashi, Yuuske Ohori, Misato Kazama, Ming-Hui Shang, Ikuko Hojo and Takashi Maruyama, who were also formerly members of Fujikawa Laboratory. They encouraged me with a lot of advice to continue my works.

Funding by Grant-in-Aid for JSPS fellows Grant Number 15J07459 is gratefully acknowledged.

I thank all members of Konishi-Niki (Fujikawa) Laboratory for kindness and assistance.

Finally I would like to express my deep gratitude to my parents for their understanding and support.

Chapter 1

General introduction

1.1 X-ray absorption fine structure

Albert Einstein discovered that the photoelectric effect is a quantum mechanical phenomenon in 1905. The mysterious effect involved the electron excitation caused by lights. In the case of X-rays that was discovered by Wilhelm Conrad Röntgen in 1895, their high energy and short wavelength enable the excitation of strongly localized core electrons. The core-electron binding energy gives the threshold of the excitation, called the absorption edge or white line, where the absorption intensity suddenly and strongly increases. The absorption-edge energy substantially differs (100 eV $\sim$) in the atomic number and a kind of orbital; however it does not deviate largely (only a few eV) by environmental changes around the absorbing atom. This important feature provide us the elemental and orbital selectivities of the X-ray absorption. In addition, the local environmental changes affect spectral shapes of the X-ray absorption, called X-ray absorption fine structure (XAFS), because excited final states are correspond to bonding or more extended orbital in one-electron (quasi-particle) picture. Therefore, the X-ray absorption spectroscopy (XAS), which is investigation of the dependence of the X-ray absorption intensity on incident X-ray energies, can directly pick up the local information around the absorbing atom. The K- and L_1-edge X-ray absorption corresponds to the excitation from $1s$ and $2s$ orbital to unoccupied p state, respectively, in dipole transition. While, the $L_{2,3}$-edge one is from $2p_{1/2}$ and $2p_{3/2}$ orbital to unoccupied d state, respectively. XAFS is classified into two energy parts: X-ray absorption near edge structure (XANES) in the energy re-

gion up to about 100 eV above white line, and extended X-ray absorption fine structure (EXAFS) above the energy region of XANES. Figure 1.1(a) shows a typical Fe K-edge XAFS spectrum of iron foils [1].

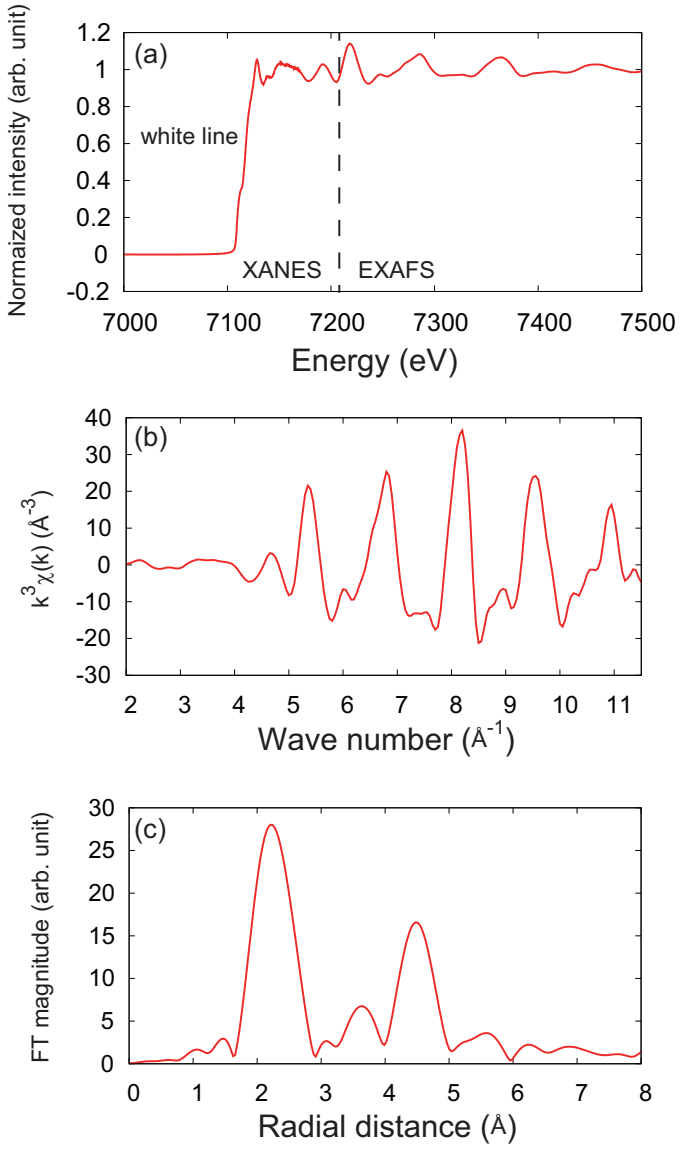

Figure 1.1: Observed Fe K-edge XAFS spectra of iron foils [1]. The top (a), middle (b) and bottom (c) panels show normalized XAFS and $\chi(k)$ spectra, and radial distribution function, respectively. The $\chi(k)$ spectrum are multiplied by k^3 factor. The radial distribution function is obtained by using $\chi(k)$ from $k = 3$ to 11 Å^{-1}.

The XANES corresponds to relatively lower energy excitation which is largely affected by valence electrons. Therefore, XANES spectra give us information of stereo local geometry and electronic structure around an absorbing atom. In particular, energy shifts of white line (chemical shift) associated with charge variation is used in many field, for

instance, evaluation of element oxidation in anodes and cathodes of lithium-ion batteries [2]. Moreover, main peak intensity near the absorption edge is used to estimate unoccupied d electrons of absorbing Pt atoms in Pt nano particles by comparison with the pure metal Pt during catalytic reaction [3]. In environmental analysis field, XANES spectra is used by finger print schemes: XANES spectra of unknown samples are compared with reference spectra to obtain composition of the samples. These analyses do not need theoretical XANES calculation. By using theoretical calculation, we can extract much more information about local structure around the absorbing atom. However, the excitation in relatively low energy region is strongly affected by electron configuration. This make XANES spectra complicated and difficult to fully understand them by only one theoretical approach.

EXAFS is well understood by using the concept of photoelectron scattering because the scattering theory is suitable for describing the continuum state with large wave number. EXAFS region is far above the threshold of the core excitation energy at least about 100 eV as shown in Fig. 1.1(a), then the excited state is treated as the photoelectron state dressing many-body effects. EXAFS spectra have the oscillation called EXAFS oscillation, which provide us with bond lengths between the absorbing atom and neighboring atoms usually up to the second nearest neighbor by using Fourier transformation and fitting to the EXAFS formula. Figures 1.1(b) and (c) show the EXAFS oscillation $\chi(k)$ and its Fourier transformation from wave number $k = 3$ to 11 (radial distribution function) of iron foils, respectively. The oscillation $\chi(k)$ is multiplied by a weight factor k^3 to compensate its amplitude decay. Peak positions and heights in the radial distribution function do not show the inter-atomic distance and coordination number directly. Thus, we need the fitting procedure by using the EXAFS formula to obtain correct information.

In general, the accuracy of interatomic distances determined by EXAFS is within 0.5-1.0% [4]. If we obtain high-quality EXAFS oscillation and good model compounds for analyses of unknown samples, the coordination numbers around the absorbing atom are determined within 10-30% accuracy [4]. We can obtain vibrational information through the Debye-Waller factor. Furthermore, by using the cummurant expansion, the anharmonicity can be also studied. Bond lengths in various materials are determined by EXAFS analyses.

There are several modes to observe XAFS spectra [5]. The most basic measurement is a transmission mode which detects the intensity of the incident and transmitted X-rays. A fluorescence mode detects characteristic X-rays instead of the transmitted X-rays for either dilute or very thin samples. An electron yield mode is similar to fluorescence yield in terms of using core-hole refilling, but electrons emitted from surface are detected instead of fluorescent X-rays. Therefore, the electron yield technique is surface sensitive because of inelastic mean free path, whereas the other modes are bulk sensitive.

1.2 X-ray magnetic circular dichroism

X-ray magnetic circular dichroism (XMCD) is the difference of the absorption of circularly polarized X-rays between ±helicity. The XMCD intensity ΔI is defined by the X-ray absorption intensity $I(m_p, \pm\mathbf{B})$ where m_p is the helicity of the incident X-rays, and $\pm\mathbf{B}$ represents a magnetization direction parallel and antiparallel to the incident X-rays.

$$\Delta I = I(+;-\mathbf{B}) - I(-;-\mathbf{B}) = I(-;+\mathbf{B}) - I(-;-\mathbf{B}) = I(+;-\mathbf{B}) - I(+;+\mathbf{B}). \quad (1.1)$$

These are equivalent because of time reversal symmetry. To obtain XMCD spectra, the spin-orbit interaction (SOI) plays an important role. A photoelectron receives orbital moments from the incident circularly polarized X-rays. The incident X-rays can excite a core electron for up and down spin. Photoelectron spin interacts with systems by the exchange scheme, and involves information of spin polarization. The SOI couples photoelectron spin to the orbital moments, and deviate up spin absorption from down spin one with same helicity (orbital moment). Therefore, XMCD spectra provide us local magnetic information because we can also use element and orbital selectivity of the X-ray absorption for XMCD. Indeed, no spin polarization in systems gives no XMCD intensity.

Sum rules for $L_{2,3}$-edge XMCD provide us with the spin and orbital magnetic moment separately in d orbital on the absorbing atom [6, 7, 8, 9, 10]. Thole et al. predicted the sum rules theoretically [9, 10]. After that, Chen at al. confirmed its applicability with magnetic experiments [7]. Nowadays, the sum rules have been one of the most important purpose to apply XMCD analyses. For K-edge XMCD, the sum rules give only p orbital moment since there is no spin-orbit interaction on the core state [8, 9].

While the sum rules is useful technique, integration of XMCD spectra neglects fine

structure in the spectra. By using theoretical calculation, we could extract much more information from XMCD spectra.

1.3 Theory for X-ray absorption spectroscopy

Many researchers have been studying the X-ray absorption spectra theoretically to understand them physically and extract much information from them. EXAFS oscillation of various materials is well understand by photoelectron scattering picture based on the scattering theory which has advantage to relatively higher energy excitation to continuum states. On the other hand, many theories have been developed to explain XANES spectra. Here, I briefly introduce them.

A multiple scattering (MS) theory describe the excitation state as photoelectron one emitted from an absorbing atom by using Green's functions [11, 12]. The photoelectron is affected by electronic and geometric structure surrounding the absorbing site through its migration in solids. To describe this, total potential is divided into atomic and interstitial region parts. Usually, we approximate the atomic parts by using spherical averaged atomic potential. This crude but important approximation is called the muffin-tin (MT) approximation. This enable us to treat the MS theory more easily. Many-body effects like plasmon excitation are involved as mean free path and effective potential in solids. Therefore, we can include long range effects up to about 10 Å from the absorbing site (of course it depends on systems) in calculated XANES spectra. This theory works well for K, L_1-edge XANES because of the delocalization of unoccupied p state even under existence of a core hole. The unique point of the MS scheme for XANES is the direct connection to the EXAFS formula due to the same scattering theory. Main difficulty of the MS theory is to take into account short range effects like the charge transfer caused by the core hole creation.

A multiplet theory for XANES spectra involves many-body effects in the absorption atom or the small calculation cluster by the configuration interaction [13, 14, 15]. This theory works well for $L_{2,3}$-edge XANES and XMCD spectra in particular open-shell transition-metal (TM) systems where the electron correlation is rather large. Moreover, comparison of the XAS spectral peaks calculated by using different electron configura-

tions gives physical interpretation of the XAS spectra. The disadvantage of the multiplet theory is the lack of long range effects further first nearest neighbor atoms because of tremendous basis sets to construct Slater determinants. This prevents the theory from including structural effects and the transition to continuum states. The configuration interaction enables us to consider the electron correlation in relatively localized state. The multiplet theory hence succeeds the $L_{2,3}$-edge XAS and XMCD calculation of TM systems.

Recently, Krüger *et al* has calculated Ca and Ti $L_{2,3}$-edge XANES spectra for Ca and Ti compounds by the multichannel MS theory, respectively [16, 17]. In light elements such as Ca and Ti, the core hole states at $2p_{1/2}$ and $2p_{3/2}$ are energetically close and merged each other. Unoccupied d states in Ca and Ti atoms is relatively delocalized and have less electron correlation than in TM such as Ni. The multichannel MS theory includes local multiplet and long-range MS effects simultaneously. Hence, this theory overcomes both difficulties in the multiplet and MS theory. The calculation showed importance of both the effects in the system which has delocalized final states with strongly merged $2p_{3/2,1/2}$ core hole states.

For other developments, Hatada *et al* has developed full potential MS theory beyond the muffin-tin approximation [18, 19, 20]. The potential in solids of dense-structural systems is well approximated by the muffin-tin approximation owing to the small interstitial region. In the full potential approach, interstitial region or surface are filled or covered by Voronoi polyhedron called empty cells. The most remarkable point of this theory is that potential shapes are exactly taken into account without any spherical harmonics expansion to avoid a convergence problem of partial waves, called the Gibbs phenomenon. This theory therefore improves the calculated XANES spectra for molecules and sparse structural systems such as $GeCl_4$ and α-quartz, respectively [19].

1.4 Outline of this thesis

By the development of XAS techniques and analyses, the local structure around an absorption atom can be investigated in a tremendous number of materials. However, to study new and complicate systems, we still need to struggle how to apply XAS methods

to them. Those novel systems include and make use of impurity, vacancy, surface, interface, complex of light and heavy elements, magnetism and so on. As a typical impurity system, impurity doped semiconductors are often discussed about its local properties. Moreover, in rare-earth (RE) doped GaN, detection of vacancies next to doped RE ion is an important issue. Meanwhile, graphene systems have attracted much attention as modern spintronic materials; however their interface properties make the analyses of the graphene complicate. Making the best use of the element and orbital selectivities of XAS is demanding for those materials.

In the present thesis, I analyze XANES spectra of RE doped GaN crystals to elucidate the local atomic structure and the nitrogen vacancy around a doped RE ion. In addition, I also develop the XMCD theory for light element absorption in magnetic systems on the basis of the MS theory. The organization of the thesis is as follows. In chapter 2, I briefly introduce the MS theory developed by Fujikawa et al [21]. To apply the MS theory to XMCD, relativistic effects are taken into account within a perturbation scheme of the Green's function. The intensity of $L_{2,3}$-edge XANES, and K, L_1-edge XANES and XMCD are described by the atomic and scattering terms. In chapter 3, Gd L_3-edge XANES spectra of the two GaN:Gd crystals under different crystal growth conditions are firstly analyzed to investigate the local structure around a doped Gd ion [22]. The GaN:Gd crystals show different XANES spectra each other. I discuss the shift of the Gd ion along to space created by nitrogen vacancies. Secondly, Dy L_3- and L_1-edge polarization-dependent XANES spectra of the two GaN:Dy crystals are analyzed. I observed that the spectral shape of GaN:RE does not depend on the RE elements, but on the crystal growth conditions. The anisotropy of the nitrogen vacancy adjacent to the RE ion is obtained by the polarization dependence of the spectra. In chapter 4, K, L_1-edge XMCD theory is developed to include the SOI on scatterer sites on the basis of the MS theory described in chap. 2. The previous and present results for BCC iron are compared analytically and numerically. The developed theory is also applied for graphene/Ni(111) systems. I find the importance of the SOI in scattering processes. These results shed light on a way to study functional materials including vacancies or magnetic species by using XAS methods.

Chapter 2

Multiple scattering theory

In this chapter, I will briefly introduce a MS theory [12, 21, 23, 24]. This theory adopts the relativistic corrections as the perturbation on the Green's function. Brouder et al. firstly adopt the idea of the perturbation expansion on the Green's function to the MS theory for powder crystal system [25, 26]. Fujikawa et al. improved the theory for arbitrary systems [21, 23, 24]. To calculate XMCD spectra, the spin-orbit interaction, which comes from the relativistic theory, is necessary. Thus, the treatment of the relativistic effect is quite important.

2.1 relativistic X-ray absorption theory

The Dirac hamiltonian h_D under the potential V_D is written by

$$h_D = c\alpha \cdot \boldsymbol{p} + \beta c^2 + V_D = \begin{pmatrix} V + c^2 & c\sigma \cdot \boldsymbol{p} \\ c\sigma \cdot \boldsymbol{p} & V - c^2 \end{pmatrix} \tag{2.1}$$

in atomic unit (Hartree). The Pauli matrix is represented by σ. The potential V_D and V are 4×4 and 2×2 matrices, respectively. If we assumed that the potential V does not include non-diagonal component in spin space, V is written as

$$V = \begin{pmatrix} V^+ & 0 \\ 0 & V^- \end{pmatrix}, \tag{2.2}$$

where $V^{+(-)}$ acts on the up (down) spin state. I define the one-electron Dirac Green's function g_D by using H_D in (2.1).

$$g_D(\varepsilon) = (\varepsilon + c^2 - H_D + i\eta)^{-1} = \begin{pmatrix} \varepsilon - V + i\eta & c\sigma\cdot\boldsymbol{p} \\ c\sigma\cdot\boldsymbol{p} & \varepsilon + 2c^2 - V + i\eta \end{pmatrix}^{-1}, \tag{2.3}$$

where ε is the total one-electron energy without the rest energy, and η is the infinitesimal to determine the boundary condition of G_D: here, $\eta \to +0$ and g_D is the out-going solution. By using the expansion proposed by Gesztesy et al. [29], g_D is represented by

$$g_D(\varepsilon) = (1-T)^{-1} \begin{pmatrix} g & gQ \\ Qg & QgQ + \frac{1}{2c^2} \end{pmatrix} = \sum_{n=0}^{\infty} T^n \begin{pmatrix} g & gQ \\ Qg & QgQ + \frac{1}{2c^2} \end{pmatrix} \tag{2.4}$$

Here, 2×2 matrices T, X, Y, Q and the one-electron non-relativistic Green's function g are defined as follows:

$$\begin{gathered} T = \begin{pmatrix} 0 & X \\ 0 & Y \end{pmatrix}, \quad X = gQ(V-\varepsilon), \quad Y = (QgQ + \frac{1}{2c^2})(V-\varepsilon), \\ Q = \frac{\sigma\cdot\boldsymbol{p}}{2c}, \qquad g \equiv g(\varepsilon) = \frac{1}{\varepsilon - T_e - V + i\eta}, \end{gathered} \tag{2.5}$$

where T_e is the electron kinetic energy. I abbreviate $g_D(\varepsilon)$ as g_D from here. The explicit form of T^n is obtained by

$$T^n = \begin{pmatrix} 0 & XY^{n-1} \\ 0 & Y^n \end{pmatrix} \tag{2.6}$$

The terms gQ, Qg and X are on the relativistic order of g/c, while the terms $QgQ + 1/2c^2$ and Y are on the order of g/c^2. We obtain the approximated g_D on the order of up to g/c^2.

$$g_D \approx \begin{pmatrix} g + gQ(V - \varepsilon - i\eta)Qg & gQ \\ Qg & QgQ + \frac{1}{2c^2} \end{pmatrix} \tag{2.7}$$

We will see that gQ, Qg and $gQ(V-\varepsilon-i\eta)Qg$ give the relativistic correction for X-ray absorption intensity soon afterward. In X-ray absorption, the core state $|c\rangle$ which absorbs the incident X-rays is well localized and energetically deep compared to the valence state. Thus, $|c\rangle$ is atomic like and written as in 4-spinor

$$|c\rangle = \begin{pmatrix} |\varphi_c\rangle \\ |\chi_c\rangle \end{pmatrix}. \tag{2.8}$$

The large (small) component $|\varphi_c\rangle$ ($|\chi_c\rangle$) is the eigenstate of J^2, L^2, S^2 and J_z. By using the Pauli spinor $y^l_{j,\mu}$ and the radial components g_c and f_c, the components $|\varphi_c\rangle$ and $|\chi_c\rangle$ are written as

$$\langle \boldsymbol{r}|\varphi_c\rangle = g_{j_c}(r) y^{l_c}_{j_c,\mu_c}(\hat{\boldsymbol{r}}), \tag{2.9}$$

$$\langle \boldsymbol{r}|\chi_c\rangle = i f_{j_c}(r)(\sigma\cdot\hat{\boldsymbol{r}}) y^{l_c}_{j_c,\mu_c}(\hat{\boldsymbol{r}}) \tag{2.10}$$

The Pauli spinor $y^l_{j,\mu}$ is obtained by

$$y^l_{j,\mu}(\hat{\boldsymbol{r}}) = \sum_{m_s=\pm 1/2} \langle\, \mu - m_s \, \frac{1}{2}\, m_s | j\mu\rangle \, Y_{l,\mu-m_s}(\hat{\boldsymbol{r}})\, |m_s\rangle\,, \tag{2.11}$$

where $\langle l_1 m_1 l_2 m_2 | l_3 m_3\rangle$ is the Clebsch-Gordan coefficient. The small component $|\chi_c\rangle$ is on the order of $|\varphi_c\rangle / c$. In one-electron approximation, the X-ray absorption intensity I is written by

$$I(\omega) = -2\mathrm{Im}\,\langle c|\Delta^* g_D(\varepsilon)\Delta|c\rangle\,, \tag{2.12}$$

where Δ is the electron-photon interaction operator. By using (2.7), the intensity I is written by

$$I(\omega) = T_{11}(\omega) + T_{12}(\omega) + T_{21}(\omega) + U_{11}(\omega) + \cdots \tag{2.13}$$

The terms $T_{11}(\omega)$, $T_{12}(\omega)$, $T_{21}(\omega)$ and $U_{11}(\omega)$ have forms each other as follows:

$$T_{11}(\omega) = -2\mathrm{Im}\,\langle\varphi_c|\Delta^* g \Delta|\varphi_c\rangle\,, \tag{2.14a}$$

$$T_{12}(\omega) = -2\mathrm{Im}\,\langle\varphi_c|\Delta^* g Q \Delta|\chi_c\rangle\,, \tag{2.14b}$$

$$T_{21}(\omega) = -2\mathrm{Im}\,\langle\chi_c|\Delta^* Q g \Delta|\varphi_c\rangle\,, \tag{2.14c}$$

$$U_{11}(\omega) = -2\mathrm{Im}\,\langle\varphi_c|\Delta^* g Q (V-\varepsilon) Q g \Delta|\varphi_c\rangle \tag{2.14d}$$

Since only T_{11} survive in the non-relativistic limit ($c \to \infty$), T_{11} is dominant in the intensity I. The relativistic correction terms T_{12}, T_{21} and U_{11} are the order of $(v/c)^2$ as described above. At the K- and L_1-edges, the initial core state is the s state, which has no spin-orbit interaction. T_{11} include the relativistic effect only on the core wave function. Thus it has no contribution to K- and L_1-edge. On the other hand, T_{12}, T_{21} and U_{11} have contribution to the XMCD because they include the spin-orbit interaction on the final (or photoelectron) state. At the $L_{2,3}$-edge, the initial core state is the p state, and has the spin-orbit interaction. Hence, T_{11} is dominant for the $L_{2,3}$-edge XMCD.

2.2 Theory of XAS

I assume that the spin dependent potential $V^{\pm}(\boldsymbol{r})$ is the sum of the spherical potential with no overlap between the neighbor sites (muffin-tin approximation).

$$V^{\pm}(\boldsymbol{r}) = \sum_{\alpha} v_{\alpha}^{\pm}(\boldsymbol{r}), \tag{2.15}$$

$$v_{\alpha}(\boldsymbol{r} - \boldsymbol{R}_{\alpha}) = v_{\alpha}(|\boldsymbol{r} - \boldsymbol{R}_{\alpha}|), \tag{2.16}$$

where $v_{\alpha}(\boldsymbol{r})$ is the spherical potential centered at the α atomic site located at $\boldsymbol{R}_{\alpha}$. In this approximation, the Green's function g^s (s is the spin index) is expanded by site t-matrix expansion (see Appendix A and C).

$$g^s = g_a^s + \sum_{\alpha} g_a^s t_{\alpha}^s g_a^s + \sum_{\alpha \neq \beta} g_a^s t_{\alpha}^s g_0^s t_{\beta}^s g_a^s + \cdots, \tag{2.17}$$

where the decay free propagator g_0^s and the propagator g_a^s including the v_a at site a is represented by

$$g_0 = \frac{1}{\varepsilon - T_e + i\Gamma}, \tag{2.18}$$

$$g_a = g_0 + g_0 v_a g_0 + g_0 v_a g_0 v_a g_0 + \cdots = g_0 + g_0 t_a g_0 = \frac{1}{\varepsilon - T_e - v_a + i\Gamma} \tag{2.19}$$

According to (2.14a), the intensity of linearly or circularly polarized X-ray absorption with the energy ω is obtained by

$$I(\omega, m_p) \approx T_{11}(\omega, m_p) = -2\mathrm{Im} \sum_{s} \langle \varphi_c | \Delta_{m_p}^* g^s \Delta_{m_p} | \varphi_c \rangle \,. \tag{2.20}$$

The index m_p represents the polarization. The circularly polarized X-rays incident to the z-direction with $\pm$ helicity is represented by $m_p = \pm$, while the linear polarization in z-direction is represented by $m_p = 0$. In this definition, we take the quantum- (or spin-) axis parallel to the incident circularly polarized X-rays or the direction of the linear polarization. The electron-photon interaction operator Δ_{m_p} is written by

$$\Delta_{m_p} \propto r Y_{1m_p}(\hat{\boldsymbol{r}}), \quad (m_p = 1,\ 0,\ -1) \tag{2.21}$$

in the dipole approximation. For linearly polarized X-rays, the incident direction does not matter until we consider the quadrupole transition; however, the quantization axis is still important and defined parallel to the z-axis. Substitute (2.17) to (2.20), we can

interpret the first, second and third term as the atomic absorption, the single and double scattering terms. The higher order terms correspond to the higher order scattering. The renormalization of the scattering terms provides all scattering including the infinity scattering.

2.2.1 Atomic term

From (2.11) $\sim$ (2.21), the spin-dependent atomic term $I^{(0)}$ is written by

$$\begin{aligned} I^{(0)s}(\omega, m_p) &= -2\mathrm{Im}\,\langle\varphi_c|\Delta^*_{m_p} g^s_A(\varepsilon)\Delta_{m_p}|\varphi_c\rangle \\ &= -2\mathrm{Im}\sum_{\mu_c, L}\left\langle l_c\mu_c - m_s\,\frac{1}{2}\,m_s|j_c\mu_c\right\rangle^2 G(l_c\mu_c - m_s 1 m_p|L)^2\sigma^s_l(\varepsilon) \quad (2.22) \end{aligned}$$

The spin magnetic quantum number m_s is $\pm\frac{1}{2}$ for the spin index $s = \pm$. The azimuthal quantum number j_c for total angular momentum is $\frac{1}{2}$ ($\frac{3}{2}$) at L_2-edge (L_3-edge). The Gaunt integral $G(l_1m_1l_2m_2|l_3m_3)$ is defined by

$$\begin{aligned} G(l_1m_1l_2m_2|l_3m_3) &= \int d\hat{\boldsymbol{r}} Y^*_{l_3m_3}(\hat{\boldsymbol{r}}) Y_{l_1m_1}(\hat{\boldsymbol{r}}) Y_{l_2m_2}(\hat{\boldsymbol{r}}) \\ &= \sqrt{\frac{(2l_1+1)(2l_2+1)}{4\pi(2l_3+1)}}\,\langle l_1 0 l_2 0|l_3 0\rangle\,\langle l_1m_1l_2m_2|l_3m_3\rangle \end{aligned} \quad (2.23)$$

The radial integral $\sigma^s_l(\varepsilon)$ represents infinite scattering inside the absorbing atom.

$$\sigma^s_l(\varepsilon) = \int g_{j_c}(r) g^s_{A,l}(r, r'; \varepsilon) g_{j_c}(r') r^3 r'^3 dr dr', \quad (2.24)$$

$$g^s_{A,l}(r, r'; \varepsilon) \sim \int \frac{\tilde{R}^s_{A,l}(pr)\tilde{R}^s_{A,l}(pr')}{\varepsilon - \varepsilon_p + i\eta} p^2 dp, \quad (2.25)$$

where $g_{A,l}$ is the l component of g_A in angular momentum representation. The radial wave function of the large component g_{j_c} is described at (2.9). The radial wave function $\tilde{R}_{A,l}(pr)$ is the real part of the regular solution of the Schrödinger equation in the atomic (or muffin-tin) sphere at the absorbing site. After the integration by the photoelectron momentum p, $\sigma^s_l(\varepsilon)$ is written by the radial integral $\rho^s_c(l)$ ($= \int \tilde{R}^s_l(kr) g_{j_c}(r) r^3 dr$) as

$$\mathrm{Im}\sigma^s(l) = -2k\rho^s_c(l)^2 \quad (2.26)$$

2.2.2 Infinite scattering term

At first, I calculate the single scattering term. When $\boldsymbol{r} \in \alpha$, $\boldsymbol{r}' \in A$ in $g_A(\boldsymbol{r}, \boldsymbol{r}')$, the Green's function $g_A(\boldsymbol{r} + \boldsymbol{R}_\alpha, \boldsymbol{r}')$ is represented by

$$\begin{aligned} g_A(\boldsymbol{r} + \boldsymbol{R}_\alpha, \boldsymbol{r}') &= g_A(\boldsymbol{r}', \boldsymbol{r} + \boldsymbol{R}_\alpha) \\ &= 2\sum_{L'L} i^{l'-l} e^{i\delta_l^A} G_{L',L}(k\boldsymbol{R}_\alpha) j_{l'}(kr) Y_{L'}(\hat{\boldsymbol{r}}) \tilde{R}_l(kr') Y_L^*(\hat{\boldsymbol{r}'}), \end{aligned} \quad (2.27)$$

where the complex wave number of the photoelectron is defined by $k = \sqrt{2(\varepsilon + \mathrm{i}\Gamma)}$ in atomic unit. The free decay propagator $G_{L,L'}(k\boldsymbol{R}_\alpha)$ is written by

$$G_{L'L}(k\boldsymbol{R}_\alpha) = -4\pi ik \sum_{L_1} i^{l_1} h_{l_1}(kR) Y_{L_1}(\hat{\boldsymbol{R}}) G(L_1 L'|L),$$

As a result, the single scattering term is written by

$$\begin{aligned} &\sum_\alpha \langle \varphi_c | \Delta^*_{m_p} g^s_A(\varepsilon) t^s_\alpha(\varepsilon) g^s_A(\varepsilon) \Delta_{m_p} | \varphi_c \rangle \\ &= 2\sum_{\mu_c} \sum_{L,L'} i^{l'-l} e^{i(\delta_l^{As} + \delta_{l'}^{As})} \rho^s_l(\varepsilon) \rho^s_{l'}(\varepsilon) \left\langle l_c \mu_c - m_s \frac{1}{2}\, m_s | j_c \mu_c \right\rangle \\ &\qquad \times G(l_c\mu_c - m_s 1 m_p | L) G(l_c \mu_c - m_s 1 m_p | L') \hat{G}^s_{L',L}(\varepsilon) \end{aligned} \quad (2.28)$$

The propagator $\hat{G}^s_{L1,L}$ is defined as

$$\hat{G}^s_{L1,L}(\varepsilon) = \sum_{\alpha,L'} G_{L_1 L'}(-k\boldsymbol{R}_\alpha) t^{\alpha s}_{l'}(k) G_{L'L}(k\boldsymbol{R}_\alpha). \quad (2.29)$$

The propagator $\hat{G}^s_{L1,L}$ describes that the photoelectron goes from the absorbing atom A, and returns to the A site after the scattering at the site α. The site t-matrix $t^{\alpha s}_l$ is represented in orbital moment representation at the site α for the spin s. This site t-matrix written by the phase shift $\delta^{\alpha,s}$ with l-th partial wave as

$$t^{\alpha s}_l(k) = -\frac{\exp(2i\delta^{\alpha s}_l - 1)}{2ik} \quad (2.30)$$

The similar procedure enable us to consider the infinite scattering term. As a result, $\hat{G}_{L1,L}$ in the single scattering term is replaced by $Z_{L1,L}$ to obtained the infinite scattering term. The spin index s is omitted here. The infinite scattering propagator is described by

$$\begin{aligned} Z_{L_1 L} &= [GtG]^{AA}_{L_1 L} + [GtGtG]^{AA}_{L_1 L} + \cdots \\ &= [G(tG)^0]^{AA}_{L_1 L} + [G(tG)^1]^{AA}_{L_1 L} + [G(tG)^2]^{AA}_{L_1 L} + \cdots \\ &= [G(1-X)^{-1}]^{AA}_{L_1 L} \end{aligned} \quad (2.31)$$

$$X^{\alpha\beta}_{L'L''} = t^{\alpha}_{l'}(k) G_{L'L''}(k\boldsymbol{R}_\alpha - k\boldsymbol{R}_\beta)(1-\delta_{\alpha\beta})$$

The terms in the braket $[\cdots]^{AA}_{L_1 L}$ describe the photoelectron migration from the A site with the angular momentum L to the A site after the MS. The element $X^{\alpha\beta}_{L'L''}$ means that the photoelectron goes from α to β, and is scattered by α. When $\alpha = \beta$, $G_{L'L''}(k\boldsymbol{R}_\alpha - k\boldsymbol{R}_\beta) = 0$. Since $[G]^{AA} = 0$, Z can be written by the inverse matrix by adding $[G]^{AA} = 0$. The t-matrix and the free decay propagator G involve electronic and geometric structures, respectively. According to (2.17), the infinite scattering term arises from $g - g_A$,

$$\begin{aligned} I^{(\infty)s}(\omega, m_p) &= -2\mathrm{Im} \sum_{\alpha} \langle \varphi_c | \Delta^*_{m_p} (g^s(\varepsilon) - g^s_A(\varepsilon)) \Delta_{m_p} | \varphi_c \rangle \\ &= -4\mathrm{Im} \sum_{\mu_c} \sum_{L,L'} i^{l'-l} e^{i(\delta^{As}_l + \delta^{As}_{l'})} \rho^s_l(\varepsilon) \rho^s_{l'}(\varepsilon) \left\langle l_c \mu_c - m_s \, \frac{1}{2} \, m_s | j_c \mu_c \right\rangle^2 \\ &\qquad \times G(l_c\mu_c - m_s 1 m_p | L) G(l_c \mu_c - m_s 1 m_p | L') Z^s_{L',L}(\varepsilon) \end{aligned} \tag{2.32}$$

2.3 Formula of XANES

In this section, I derive more explisit expresion for XANES spectra. The incident linearly polarized X-rays are assumed, which corresponds to $m_p = 0$.

2.3.1 $L_{2,3}$-edge XANES

- L_2-edge ($j_c = 1/2$)

From (2.22), if we neglect the s state ($l = 0$) contribution, the atomic XANES spectrum at the L_2-edge is written by

$$\begin{aligned} I^{(0)+}_{L_2}(\omega, 0) &= -2\mathrm{Im}\, \sigma^+_2(\varepsilon) \left(\left\langle 10 \, \frac{1}{2} \frac{1}{2} \, | \, \frac{1}{2} \frac{1}{2} \right\rangle^2 G(1010|20)^2 \right. \\ &\qquad \left. + \left\langle 1 - 1 \, \frac{1}{2} \frac{1}{2} \, | \, \frac{1}{2} - \frac{1}{2} \right\rangle^2 G(1-110|2-1)^2 \right) \\ &= -2\mathrm{Im} \frac{\sigma^+_2(\varepsilon)}{6\pi}, \end{aligned} \tag{2.33}$$

$$\begin{aligned} I^{(0)-}_{L_2}(\omega, 0) &= -2\mathrm{Im}\, \sigma^-_2(\varepsilon) \left(\left\langle 11 \, \frac{1}{2} - \frac{1}{2} \, | \, \frac{1}{2} \frac{1}{2} \right\rangle^2 G(1110|21)^2 \right. \\ &\qquad \left. + \left\langle 10 \, \frac{1}{2} 1 \frac{1}{2} \, | \, \frac{1}{2} - \frac{1}{2} \right\rangle^2 G(1010|20)^2 \right) \\ &= -2\mathrm{Im} \frac{\sigma^-_2(\varepsilon)}{6\pi}. \end{aligned} \tag{2.34}$$

Although the unoccupied density of state of the s state is small compared to that of the d state in most of cases, the justification of this approximation is depend on the system. From (2.32), the scattering part of the L_2-edge XANES spectrum is given by

$$\begin{aligned} I_{L_2}^{(\infty)+}(\omega,0) &= -4\mathrm{Im}\left[e^{2i\delta_2^{A+}}\rho_2^+(\varepsilon)^2\left(\langle 10\,\frac{1}{2}\frac{1}{2}|\frac{1}{2}\frac{1}{2}\rangle^2 G(1010|20)^2 Z^+_{20,20}(\varepsilon)\right.\right. \\ &\qquad \left.\left. + \langle 1-1\,\frac{1}{2}\frac{1}{2}|\frac{1}{2}-\frac{1}{2}\rangle^2 G(1-110|2-1)^2 Z^+_{2-1,2-1}(\varepsilon)\right)\right] \\ &= -4\mathrm{Im}\left[e^{2i\delta_2^{A+}}\rho_2^+(\varepsilon)^2\frac{1}{30\pi}\left(2Z^+_{20,20}(\varepsilon)+3Z^+_{2-1,2-1}(\varepsilon)\right)\right] \qquad (2.35) \\ I_{L_2}^{(\infty)-}(\omega,0) &= -4\mathrm{Im}\left[e^{2i\delta_2^{A-}}\rho_2^-(\varepsilon)^2\left(\langle 11\,\frac{1}{2}-\frac{1}{2}|\frac{1}{2}\frac{1}{2}\rangle^2 G(1110|21)^2 Z^-_{21,21}(\varepsilon)\right.\right. \\ &\qquad \left.\left. + \langle 10\,\frac{1}{2}-\frac{1}{2}|\frac{1}{2}-\frac{1}{2}\rangle^2 G(1010|20)^2 Z^-_{20,20}(\varepsilon)\right)\right] \\ &= -4\mathrm{Im}\left[e^{2i\delta_2^{A-}}\rho_2^+(\varepsilon)^2\frac{1}{30\pi}\left(2Z^-_{20,20}(\varepsilon)+3Z^-_{21,21}(\varepsilon)\right)\right] \qquad (2.36) \end{aligned}$$

Here, the infinite scattering terms including s state ($l=0$) terms are neglected again. The symmetrical relation of the propagator is

$$\begin{aligned} Z_{L,L'} &= (-1)^{l+m+l'+m'} Z_{\bar{L}',\bar{L}}, \\ &(L=(l,m),\ \bar{L}=(l,-m)). \end{aligned} \qquad (2.37)$$

Thus, we obtain the relation $Z_{2+1,2+1} = Z_{2-1,2-1}$. To summarize the L_2-edge XANES formula, the total spin-dependent L_2-edge absorption $I_{L_2} = I_{L_2}^{(0)} + I_{L_2}^{(\infty)}$ is given by

$$I^{\pm}_{L_2}(\omega,0) = -2\mathrm{Im}\left[\frac{1}{6\pi}\sigma_2^{\pm}(\varepsilon) + e^{2i\delta_2^{A\pm}}\rho_2^{\pm}(\varepsilon)^2\frac{1}{15\pi}\left(2Z^{\pm}_{20,20}(\varepsilon)+3Z^{\pm}_{21,21}(\varepsilon)\right)\right] \qquad (2.38)$$

- L_3-edge ($j_c = 3/2$)

We can obtain the formula of the L_3-edge XANES spectrum through the same procedure as the L_2-edge.

$$\begin{aligned} I_{L_3}^{(0)+}(\omega,0) &= -2\mathrm{Im}\left[\sigma_2^+(\varepsilon)\left(\langle 11\,\frac{1}{2}\frac{1}{2}\,|\,\frac{3}{2}\frac{3}{2}\,\rangle^2 G(1110|21)^2\right.\right. \\ &\qquad + \langle 10\,\frac{1}{2}\frac{1}{2}\,|\,\frac{3}{2}-\frac{1}{2}\,\rangle^2 G(1010|20)^2 \\ &\qquad \left.\left. + \langle 1-1\,\frac{1}{2}\frac{1}{2}\,|\,\frac{3}{2}-\frac{1}{2}\,\rangle^2 G(1-110|2-1)^2\right)\right] \\ &= -2\mathrm{Im}\frac{\sigma_2^+(\varepsilon)}{3\pi}, \qquad (2.39) \end{aligned}$$

$$
\begin{aligned}
I_{L_3}^{(0)-}(\omega,0) = -2\mathrm{Im}\Bigg[\sigma_2^-(\varepsilon)\Bigg(&\langle\, 11\,\frac{1}{2}-\frac{1}{2}\,|\,\frac{3}{2}\frac{1}{2}\,\rangle^2\, G(1110|21)^2 \\
&+\langle\, 10\,\frac{1}{2}-1\frac{1}{2}\,|\,\frac{3}{2}-\frac{1}{2}\,\rangle^2\, G(1010|20)^2\Bigg) \\
&+\langle\, 1-1\,\frac{1}{2}1-\frac{1}{2}\,|\,\frac{3}{2}-\frac{3}{2}\,\rangle^2\, G(1-110|2-1)^2\Bigg)\Bigg] \\
= -2\mathrm{Im}&\frac{\sigma_2^-(\varepsilon)}{3\pi}. \qquad (2.40)
\end{aligned}
$$

$$
\begin{aligned}
I_{L_3}^{(\infty)+}(\omega,0) = -4\mathrm{Im}\Bigg[e^{2i\delta_2^{A+}}\rho_2^+(\varepsilon)^2\Bigg(&\langle\, 11\,\frac{1}{2}\frac{1}{2}|\frac{3}{2}\frac{3}{2}\rangle^2\, G(1110|21)^2 Z^+_{21,21}(\varepsilon) \\
&+\langle\, 10\,\frac{1}{2}\frac{1}{2}|\frac{1}{2}\frac{1}{2}\rangle^2\, G(1010|20)^2 Z^+_{20,20}(\varepsilon) \\
&+\langle\, 1-1\,\frac{1}{2}\frac{1}{2}|\frac{3}{2}-\frac{1}{2}\rangle^2\, G(1-110|2-1)^2 Z^+_{2-1,2-1}(\varepsilon)\Bigg)\Bigg] \\
= -4\mathrm{Im}&\left[e^{2i\delta_2^{A+}}\rho_2^+(\varepsilon)^2\frac{1}{15\pi}\left(2Z^+_{20,20}(\varepsilon)+3Z^+_{2+,2+}(\varepsilon)\right)\right] \qquad (2.41) \\
I_{L_3}^{(\infty)-}(\omega,0) = -4\mathrm{Im}\Bigg[e^{2i\delta_2^{A-}}\rho_2^-(\varepsilon)^2\Bigg(&\langle\, 11\,\frac{1}{2}-\frac{1}{2}|\frac{3}{2}\frac{1}{2}\rangle^2\, G(1110|21)^2 Z^-_{21,21}(\varepsilon) \\
&+\langle\, 10\,\frac{1}{2}-\frac{1}{2}|\frac{3}{2}-\frac{1}{2}\rangle^2\, G(1010|20)^2 Z^-_{20,20}(\varepsilon) \\
&+\langle\, 1-1\,\frac{1}{2}-\frac{1}{2}|\frac{3}{2}-\frac{3}{2}\rangle^2\, G(1-110|2-1)^2 Z^-_{2-1,2-1}(\varepsilon)\Bigg)\Bigg] \\
= -4\mathrm{Im}&\left[e^{2i\delta_2^{A-}}\rho_2^+(\varepsilon)^2\frac{1}{15\pi}\left(2Z^-_{20,20}(\varepsilon)+3Z^-_{21,21}(\varepsilon)\right)\right] \qquad (2.42)
\end{aligned}
$$

$$
I_{L_3}^{\pm}(\omega,0) = -2\mathrm{Im}\left[\frac{1}{3\pi}\sigma_2^{\pm}(\varepsilon)+e^{2i\delta_2^{A\pm}}\rho_2^{\pm}(\varepsilon)^2\frac{2}{15\pi}\left(2Z^{\pm}_{20,20}(\varepsilon)+3Z^{\pm}_{21,21}(\varepsilon)\right)\right] \qquad (2.43)
$$

If we neglect the relativistic effect (spin-orbit coupling) on the core radial wave function, which means $|\varphi^{2p}_{1/2}\rangle = |\varphi^{2p}_{3/2}\rangle$, the branching ratio L_3/L_2 is just $L_3/L_2 = 2$ because the local correlation effect such as the multiplet effect is not included. The relatively localized d orbital in strong correlated 3d TM systems deviate the branching ratio from $L_3/L_2 = 2$. Krüger and Natoli developed the multichannel theory which involves the MS and the multiplet, simultaneously [16]. This theory improved calculated spectra of TiO_2 at $L_{2,3}$-edge [17]. The $2p_{1/2}$ and $2p_{3/2}$ energies of Ti are quite close. Therefore, the created core hole at L_2- or L_3-edge is merged with the other. Even the strong correlation system, the multichannel theory works very well due to the inclusion of the long (MS) and short (multiplet) range effects. In addition, the branching ratio on heavy elements also differs

from $L_3/L_2 = 2$ due to the splitting of the d-orbital energy by the jj-coupling. In the above $I^{\pm}_{L_3}$, the relativistic effect is only included at the core state. The spin-orbit splitting of the $2p$ core radial wave function changes the branching ratio, but the change is not large. I only consider the relativistic effect as a perturbation: the correction terms up to the order of $(v/c)^2$ affect the XANES spectra negligibly. Nevertheless, this perturbation technique is useful when we do not care about the branching ratio cased by the spin-orbit interaction on the photoelectron state. To go beyond that situation, we should obtain the photoelectron wave function by solving the Dirac equation directly.

The radiation field effect also improves the calculated branching ratio reported by Ankudinov et al [30]. Fujikawa included the radiation field screening in the MS theory for XAS and XMCD spectra [31, 32]. In the present thesis, we do not refer the branching ratio problem any further.

2.3.2 K, L_1-edge XANES

$$\begin{aligned} I^{(0)+}_{K,L_1}(\omega,0) &= -2\mathrm{Im}\left[\sigma^+_1(\varepsilon)\left\langle 00\,\frac{1}{2}\frac{1}{2}\,|\,\frac{1}{2}\frac{1}{2}\right\rangle^2 G(0010|10)^2\right] \\ &= -2\mathrm{Im}\frac{\sigma^+_1(\varepsilon)}{4\pi}, \end{aligned} \tag{2.44}$$

$$\begin{aligned} I^{(0)-}_{K,L_1}(\omega,0) &= -2\mathrm{Im}\left[\sigma^-_1(\varepsilon)\left\langle 00\,\frac{1}{2}-\frac{1}{2}\,|\,\frac{1}{2}-\frac{1}{2}\right\rangle^2 G(0010|10)^2\right] \\ &= -2\mathrm{Im}\frac{\sigma^-_1(\varepsilon)}{4\pi}, \end{aligned} \tag{2.45}$$

$$I^{(\infty)+}_{K,L_1}(\omega,0) = -4\mathrm{Im}\left[e^{2i\delta_1^{A+}}\rho^+_1(\varepsilon)^2\left(\left\langle 00\,\frac{1}{2}\frac{1}{2}|\frac{1}{2}\frac{1}{2}\right\rangle^2 G(0010|10)^2 Z^+_{10,10}(\varepsilon)\right)\right] \tag{2.46}$$

$$= -4\mathrm{Im}\left[e^{2i\delta_1^{A+}}\rho^+_1(\varepsilon)^2\frac{1}{4\pi}Z^+_{10,10}(\varepsilon)\right], \tag{2.47}$$

$$I^{(\infty)-}_{K,L_1}(\omega,0) = -4\mathrm{Im}\left[e^{2i\delta_1^{A-}}\rho^-_1(\varepsilon)^2\left(\left\langle 00\,\frac{1}{2}\frac{1}{2}|\frac{1}{2}\frac{1}{2}\right\rangle^2 G(0010|10)^2 Z^-_{10,10}(\varepsilon)\right)\right] \tag{2.48}$$

$$= -4\mathrm{Im}\left[e^{2i\delta_1^{A-}}\rho^-_1(\varepsilon)^2\frac{1}{4\pi}Z^-_{10,10}(\varepsilon)\right] \tag{2.49}$$

$$I^{\pm}_{K,L_1}(\omega,0) = -2\mathrm{Im}\left[\frac{1}{4\pi}\sigma^{\pm}_1(\varepsilon) + e^{2i\delta_2^{A\pm}}\rho^{\pm}_1(\varepsilon)^2\frac{1}{2\pi}Z^{\pm}_{10,10}(\varepsilon)\right] \tag{2.50}$$

The K, L_1-edge XMCD theory is discussed in Chap. 4.

Chapter 3

XANES analyses for vacancies in GaN:RE

3.1 Introduction

Intentional formation of vacancies as well known in the classic F-center [33] or modern vacancy centers [34] is sometimes addressed in fundamental and application fields. Imperfections including vacancies make crystal quality poor, while, in some cases, they have advantages to supply the carriers such as electrons and holes in semiconductors. It is well known that the nitrogen vacancy in GaN behaves as a donor. Recently, a nitrogen-vacancy center in the nitrogen-doped diamond has attracted much interest as a source of single-photon emission, for instance, in quantum dots [34].

GaN:Gd was formerly the first candidate in the room-temperature-operative dilute magnetic semiconductors [35]. After that, a colossal magnetic moment as large as $4000\mu_B$/Gd was reported in low Gd doped samples [36, 37]. However, theoretical conclusive results have not been obtained to explain this extremely high moment [38, 39, 40]. In addition, X-ray magnetic circular dichroism (XMCD) [41] and electron paramagnetic resonance (EPR) [42] measurements have indicated that the GaN:Gd system is paramagnetic at room temperature. The magnetic behavior of GaN:RE is therefore not clear. Meanwhile, RE-compounds or RE-doped materials present the luminescence involving the interesting properties originating in intra-4f transitions. RE-doped GaN (GaN:RE) also has rather strong and sharp intra-atomic luminescence lines as well as exciton-involved

luminescence. The energy of the intra-$4f$ luminescence is insensitive on temperature since the well localized $4f$-orbitals are shielded by the outer $5s$ and $5p$ shells, resulting in the weak affect of crystal field. These properties enable us to use GaN in multi- or full-color light emitted diodes (LED) by doping various RE ions. To understand deeply the physical properties of RE-doped GaN, and to feed back to the fine processing of the crystal growth, the knowledge of the local geometry around the doped RE-ion is strongly desired.

While the GaN:Gd system has been well studied due to its historical aspects and colossal magnetic moments, the GaN:RE doped by other RE elements has been relatively unexplored. A few authors have investigated the properties of GaN:Dy quantum wells [43, 44, 45]. Dy atoms has the largest magnetic moment (10.6 μ_B) among the RE elements. The GaN:Dy/GaN double-barrier magnetic tunnel junction showed ferromagnetism at room temperature [44]. The double-barrier structure for spintronic materials was originally found in (Ga,Mn)As systems. It showed a current rectification depending on the mangetic alignment, which can be switched with a very low current-junction threshold at zero field [46]. The GaN:Dy/GaN double-barrier structure had a middle free magnetic GaN:Dy layer sandwiched by top and bottom magnetic tunnel junctions GaN/GaN:Dy/GaN. Interestingly, the thickeness of the middle GaN:Dy layer affected the in-plane and out-of-plane easy-axes, indicating the interaction between the GaN:Dy layers beyond GaN layers [44]. Thus, GaN:RE dilute magnetic semiconductors could provide a novel functional materials.

Two different types of the GaN:Gd crystals have been found under the Ga- and N-rich crystal growth conditions [22]. This definition is more clearly described in following Sections. Figure 3.1 shows XRD profiles from the Ga-rich (Type-1) and N-rich (Type-2) samples [22]. No diffraction from Gd metal and GdN was observed. The Type-1 reflection shows two peaks caused from a GaN template (higher angles) and a GaN:Gd sample layer (lower angles). In many alloys, diffraction peak energies linearly shift from a pure metal one to another pure metal one with their composition, which is well known as Vegard's law [47]. The such peak shift also observed in InGaN systems [48]. The peak shift of the Ga-rich sample therefore implies that the doped Gd ion caused the lattice expansion of the matrix GaN in the Ga-rich sample layer. On the other hand, the N-rich one has only

the GaN template peak. Thus, the same lattice constant seems to be maintained as the undoped crystal in spite of the Gd doping. One possibility of this origin is relaxation of the lattice expansion due to vacancies, especially nitrogen ones adjacent to the doped Gd ions. The positron annihilation is the most possible candidate to detect atomic defects based on their size; however, it has difficulty to determine the configuration around the vacancy, for instance, whether adjacent to a doped ion or not [49, 50]. EXAFS analyses based on the substitution at a Ga site by a Gd ion determined the RE-N and -Ga distances [51]. However, EXAFS spectra show no prominent difference between the Ga- and N-rich crystals except for amplitude of EXAFS oscillation. The coordination number around RE ions in thin GaN:RE crystals is hardly obtained by EXAFS because of short available k range due to noises [51]. In addition we have few appropriate model compounds for GaN:RE crystals: RE nitride has the rock-salt structure [52, 53], while GaN:RE probably has local tetragonal structure around the RE ion [22, 41, 54, 55]. Alternatively, XANES spectra provide us the stereo local structural information around the absorbing atom. It is worth studying vacancies adjacent to the doped RE ion by using XANES analyses at RE absorbing edge.

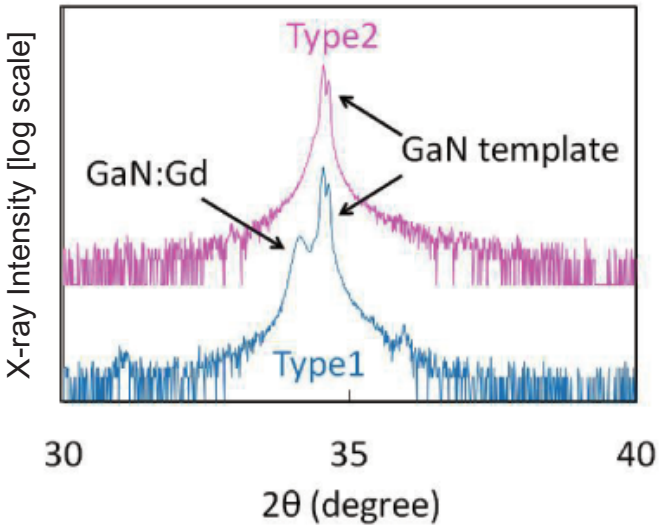

Figure 3.1: Observed XRD profiles of the Ga-rich (Type-1) and N-rich (Type-2) GaN:Gd samples. Reprinted from [22] with permission from the Surface Science Society of Japan.

RE L_1-edge XANES spectra are found in only a few cases. The RE L_1-edge spectra for RE phosphate glasses have been reported by Mountjoy et al. [56]. Usually, RE L_3-edge absorption is adopted in the investigation related to RE elements because the RE

K-edges are too high to receive the possibly analytical spectra. The lowest case is 40443 eV at Ce K-edge. The RE L_1-edge XANES spectra slightly overlaps with a RE L_2-edge EXAFS spectra, which disturbs L_1-edge EXAFS analyses. While the RE L_2-edge EXAFS oscillation, which oscillates slowly and weakly at L_1-edge energy, might affect less to L_1-edge XANES analyses. At the L_1-edge absorption, a $2s$ core electron is excited to an unoccupied p state in dipole selection, whereas a $2p$ core electron is mainly excited to an unoccupied d state at L_3-edge. This difference in the final state provides us with the different structural information in some systems. Mountjoy et al. found the local atomic geometry around the RE ion to be non-centrosymmetric by the pre-edge of RE L_1-edge XANES spectra. Although the RE L_1-edge XANES analyses provide us with the useful information about the local geometry, such reports for the GaN:RE spectra are not found in literatures as far as we know.

For analyses of XANES spectra, a real-space MS theory [11, 12] is useful for the absorption edge whose final (unoccupied) state is delocalized, such as K, L_1-edge and heavier element $L_{2,3}$-edge. This theory has advantage for impurity systems because of no requirement of the periodic boundary condition. While, a multiplet theory is a powerful tool to analyze TM $L_{2,3}$- and RE $M_{4,5}$-edge XANES spectra, particularly in strong correlated systems [57]. Generally, if multiplet splitting is small relative to band width, we can neglect its effect on XANES spectra, and adopt MS calculations.

In this chapter, I firstly analyze Gd L_3-edge XANES spectra of GaN:Gd using the real-space MS calculations (FEFF8.4 code) [27, 28] on the Ga- and N-rich GaN:RE crystals to study the stereo structure around doped RE ions. Secondly, I perform Dy L_3- and L_1-edge polarization-dependent XANES measurements and calculations for the Ga- and N-rich GaN:Dy crystals. Finally, results for GaN:Dy are feedbacked to the discussion for nitrogen vacancies in GaN:Gd.

3.2 GaN:Gd

3.2.1 Experimental

Figure 3.2 shows a schematic image of a sample structure. The Gd-doped samples were prepared on (0001)-plane sapphire substrates laminated with an n-type GaN template by

a radio frequency molecular beam epitaxy. The Gd cell temperature is selected at 1100°C to contain the favorable Gd concentration (∼1.0 at%) for the crystals. The Ga vapor pressures were 1.8×10^{-7} and 0.7×10^{-7} Torr for the Ga- and N-rich GaN:Gd crystals, respectively. The crystal layers were grown along the c-axis of the wurtzite GaN. The GaN:Gd layers about 150 nm thick were finally covered by a 3-nm-thick GaN cap layer. The Gd concentration in the GaN:RE sample layer was estimated to be about 1.0 at% ($\sim Ga_{99}Gd_1N_{100}$) by a fluorescent X-ray analysis method.

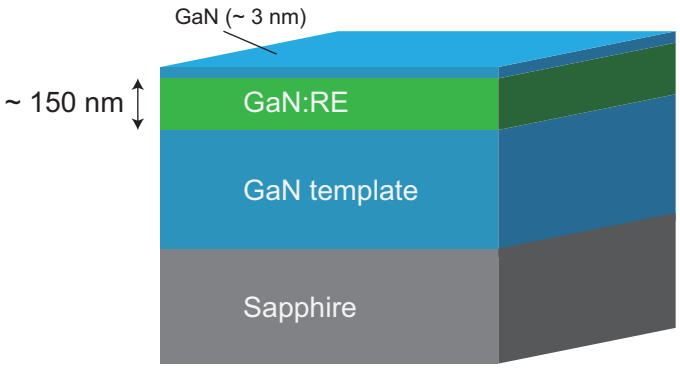

Figure 3.2: A schematic image of a sample structure. Layers of GaN template and sapphire are sufficiently thicker than a GaN:RE layer.

The Gd L_3-edge XANES measurements of GaN:Gd were performed at a beamline BL9A in PF, KEK: the edge energy in literature is 7252 eV [58]. The $L_{\alpha_{1,2}}$ fluorescence line of Gd (L_{α_1}:6057.2 eV and L_{α_2}:6025.0 eV [59]) was detected by using a solid-state detector (SSD, Ge:Li) with 19 elements to obtain the L_3-edge spectra with a fluorescence mode. The X-ray energy was calibrated at the pre-edge of the Cu foil (12.7185°). The incident X-ray is linearly polarized in the horizontal direction normal to the crystal growth direction, in other words, parallel to the c-axis of the wurtzite structure. The measurements were performed at room temperature.

3.2.2 Calculation

Multiplet effects

Before introducing a basic MS calculation models in this chapter, I discuss multiplet effects on RE $L_{2,3}$-edge XANES spectra of GdN as a general RE nitrogen compound.

GdN is one of spintronic materials with a rock-salt structure to show semiconductor-metal transition and huge negative magnetoresistance [60]. X-ray photoemission spectroscopic measurements showed trivalent ionic behavior of Gd due to itinerant character of its 5d and 6s electrons [60]. The behavior of Gd^{3+} was also found in GdX (X = Bi, Sb, As, P) [61]. Thus, Gd atoms in a solid is often mentioned as Gd^{3+}. The unoccupied d-band width of Gd in GdN is about $7 \sim 8$ eV in according to the calculated l-projected density of states [62]. I employ the CTM4XAS5.5 code [63] to calculate XANES spectra with a multiplet scheme. Since this code cannot treat the p-d dipole transition of RE ions directly, Sc^{3+} are chosen as a basis of the RE^{3+} calculation. The Coulomb and exchange integrals F^k and G^k are obtained by using the MCDFGME code [64]. The exchange integral between 4f and 5d orbitals are approximated by applied magnetic fields (~ 1 eV). The crystal field parameter 10Dq is estimated from the l-projected density of states [62] and set to 5 eV. The half width at half maximum of the Lorentzian function is 2 eV as the lifetime broadening at L_3-edge of Gd [65]. I adjust the spin-orbit interaction on the 2p core orbital to obtain the L_2- and L_3-edge splitting about 700 eV in reported spectra [66] Figure 3.3 shows the calculated Gd L_3-edge XANES spectra of Gd^{3+}. The crystal parameter 10Dq splits the spectrum of the only 2p SOI term to t_{2g} and e_g configurations. The Coulomb and exchange integrals FG between 2p and 5d, and the 4f exchange M also split SOI + 10Dq; however that effects is smaller than the crystal field one and buried by the lifetime broadening. Although the SOI on 5d orbital is not included, it is too small to overcome the 10Dq and lifetime effects. Moreover, the observed Gd L_3-edge XANES spectra of GdN has only single peak [66]. This could be explained by band effects which broaden the spectra with the band width about 7 eV [62]. The band broadening also buries the multiplet effects. Therefore, we safe to use ordinary MS calculations for RE nitride. From this result, we could analyze RE L_3-edge XANES spectra by using the MS theory.

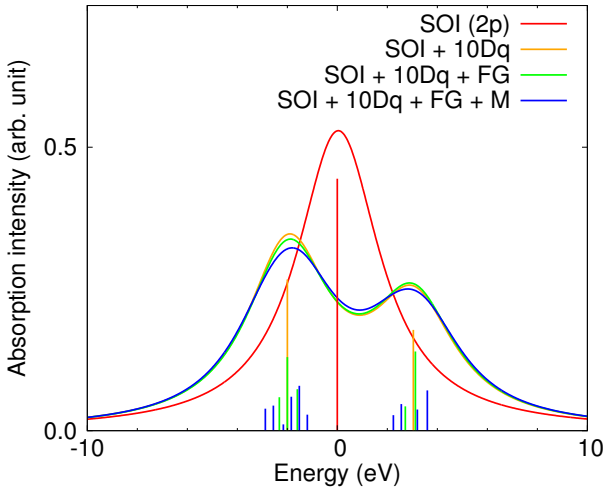

Figure 3.3: The calculated Gd L_3-edge XANES spectra of Gd^{3+} ion. The crystal field parameter is represented by 10Dq, and FG shows the Coulomb and exchange integrals between 2p and 5d orbitals. The approximated exchange integral as magnetic fields show by M. The spectra of SOI (2p), SOI + 10Dq, SOI + 10Dq + FG and SOI + 10Dq + FG + M are shown by red, orange, green and blue lines, respectively. Peak energies are shifted to set the SOI (2p) term at zero. No-broadened line spectra are also shown.

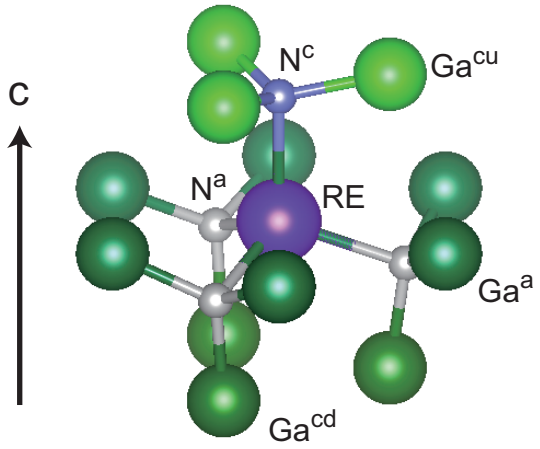

Figure 3.4: Coordination around a RE ion in the basic model cluster shown up to the near Ga shell. The nitrogen sites next to the RE ion are defined as N^c on the c-axis, and N^a not on the c-axis. The Ga sites close to the RE ion are defined as Ga^{cu} and Ga^{cd} in the c-axis direction, and Ga^a in normal direction to the c-axis.

MS cluster models

In this section, I introduce model clusters to calculate XANES spectra by the FEFF8.4 code [27, 28]. The model clusters are constructed referring to GaN structures, wurtzite structure, $P_{6_3mc}(C_{6v}^4)$ [68]. For all the models, I employ a cluster less than 8 Å radii including about 165 atoms around the Gd ion, which occupies a Ga ion site in GaN to consider the substitution. Other researchers also reported the Gd substitution in GaN:Gd [41, 54, 55]. Figure 3.4 shows the basic model cluster for the Gd XANES calculation in this chapter. The nitrogen sites next to the RE ion are defined as N^c on the c-axis, and N^a not on the c-axis. Moreover, the Ga sites close to the RE ion are defined as Ga^{cu} and Ga^{cd} in the c-axis direction, and Ga^a in normal direction to the c-axis. The distance of the first and second nearest N and Ga ions from the RE ion in Fig. 3.4 is referred by the results of EXAFS analyses with assuming the RE substitution [43, 51]. The coordination from the RE ion further the Ga ions is kept as the GaN matrices.

In the previous result [22], the lattice constant of GaN reported as $a = 3.18907(8)$ and $c = 5.1855(2)$ in the ideal wurtzite structure ($u = 0.3750$) was used [67]. In this thesis, I adopt later reported lattice constant and u parameter [68] ($a = 3.18940(8)$ $c = 5.18614(2)$ with $u = 0.3789$). This difference changes bond lengths of Ga-N^c and Ga-N^a: Ga-N^c 1.945 Å is shorter than Ga-N^a 1.955 Å in $u = 0.375$, while Ga-N^c 1.965 Å is longer than Ga-N^a 1.945 Å in $u = 0.3789$. Generally, effects of bond length changes in the order of 0.01 Å are negligible for XANES spectra, but we unify parameters to later ones to keep consistency with GaN:Dy section.

To investigate the Ga-rich GaN:Gd sample involving lattice expansion, I introduce bond expansion between the centered Gd ion and neighboring nitrogen ions: Gd-N^a 2.224 Å and Gd-N^c 2.247 Å have the same ratio between Ga-N^a 1.945 Å and Ga-N^c 1.965 Å in GaN, as shown in Table 3.1. For comparison, Table 3.1 represents atomic distances in GdN [53]. Moreover, expanded distances between the Gd ion and neighboring Ga ions are also considered: Gd-Ga^a 3.314 Å and Gd-Ga^{cu} and -Ga^{cd} 3.305 Å have the same ratio between Ga-Ga^a 3.189 Å and Ga-Ga^{cu} and -Ga^{cd} 3.180 Å in GaN. These distances are also shown in Table 3.1. Their averaged Gd-N and -Ga distances 2.23 and 3.31 Å were determined by EXAFS analyses with a Gd substitution at a Ga site in GaN [51]. Therefore, other models which a Gd ion locates at an interstitial site may not be

Table 3.1: Atomic distances in Gd systems and GaN.

Atomic pairs	GaN:Gd (Å) [51]	GaN (Å) [68]	GdN (Å) [53]
Gd(Ga)-N^a	2.224	1.945	2.499
Gd(Ga)-N^c	2.247	1.965	2.499
RE(Ga)-Ga^a(RE)	3.314	3.189	3.534
RE(Ga)-Ga^c(RE)	3.305	3.180	3.534

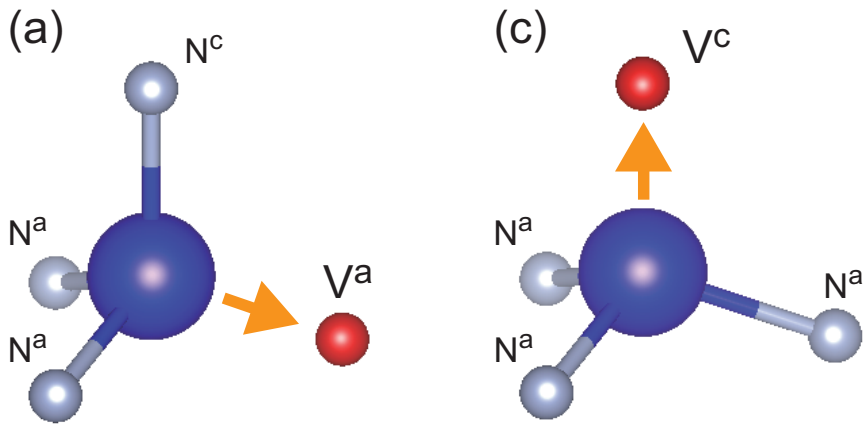

Figure 3.5: Calculated models (a) and (c) which have nitrogen vacancies V^a and V^c at a N^a and the N^c, respectively. The arrows show that the Gd ion shifts 0.0, 0.3, 0.5 and 1.0 Å to nitrogen vacancies.

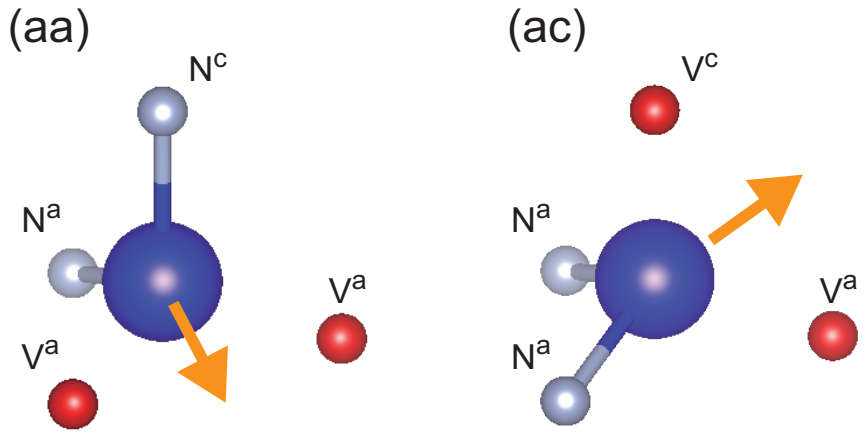

Figure 3.6: Calculated models (aa) and (ac) which have two nitrogen vacancies. The model (aa) has two V^a vacancies, while the model (ac) has one V^a and V^c. The arrows show that the Gd ion shifts 0.0, 0.3, 0.5 and 1.0 Å to bisection of two nitrogen vacancies.

dominant. This model is defined as the expansion model. For analyses of the N-rich XANES spectra, we adopt vacancy models. All the vacancy models have the same coordination as GaN except for the Gd ion and nitrogen vacancies. I consider four configuration of nitrogen vacancies: (a) one N^a vacancy (V^a); (c) one N^c vacancy (V^c); (aa) two V^a; (ac) one V^a and one V^c. Then, the models (a) and (c) ((aa) and (ac)) are classified as one vacancy (two vacancies) models. Figures 3.5 and 3.6 shows the models up to nitrogen sites next to the Gd ion. The nitrogen sites N^a has three equivalent ones, so that I obtain calculated spectra involving N^a vacancies by averaging the V^a sites. To consider the lattice relaxation conceived from the XRD profiles of N-rich GaN:Gd [22], the Gd ion is shifted 0.0, 0.3, 0.5 and 1,0 Å toward the space due to the vacancy creation as shown in Figs. 3.5 and 3.6. Note that these vacancy models are based on the non-expansion structure to consider no lattice expansion.

3.2.3 Results and Discussion

Figure 3.7 shows the observed L_3-edge XANES spectra of the Ga- and N-rich GaN:Gd samples. The Ga-rich spectrum has a shoulder and hump at about 7252 eV and 7268 eV, respectively. This spectrum is similar to other reported spectra [54, 55]. On the other hand, the N-rich spectrum shows no shoulder and hump. The spectrum looks like the one of free atoms, but free Gd ions in GaN:Gd crystals are not feasible. Thus, the Ga- and N-rich GaN:Gd crystals show the difference of XANES spectra as well as XRD profiles [22].

To investigate the Ga-rich spectrum, I calculate XANES spectra by using no vacancy models described above to consider the lattice expansion. Figure 3.8 shows the calculated XANES spectra with and without the Gd-N and -Ga distance expansion. The observed Ga-rich spectrum is also shown for comparison. The expansion spectra show better agreement with the observed one than the no-expansion one. In the no-expansion model, the Gd-N distances are too short and not realistic because of the larger Gd ion radius than the Ga ion one. Thus, the discrepancy of the no-expansion model is reasonable. The observed spectral features are well represented by the expansion spectra, especially the hump. Moreover, the Gd-Ga distance expansion improves the intensity ratio between the main peak and shoulder compared with the model with only the Gd-N expansion.

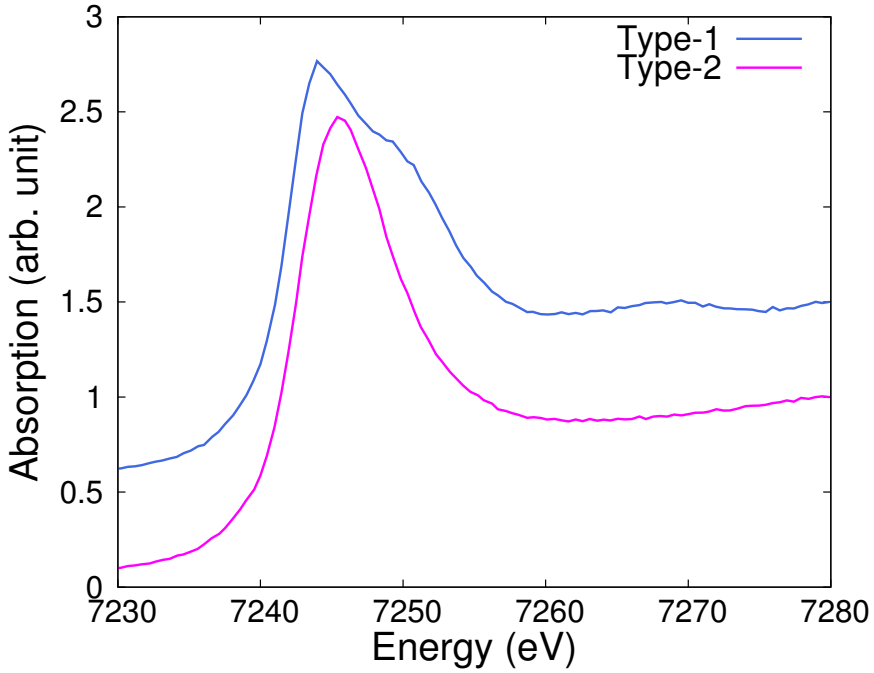

Figure 3.7: The observed Gd L_3-edge XANES spectra of the Ga-rich (Type-1) and N-rich (Type-2) GaN:Gd samples [22]. Reprinted from [22] with permission from the Surface Science Society of Japan.

The expansion spectra are similar to the calculated spectra reported before [41, 54, 55]. Therefore, I conclude that doped Gd ions substitute Ga sites of wurtzite GaN in the Ga-rich GaN:Gd crystal. I also check the effect of a Ga vacancy on the spectral shape. Releasing the distortion around doped Gd ions by Ga vacancies could be more difficult than nitrogen ones adjacent to the Gd ions. Hence, Ga vacancies does not contradict with the lattice expansion suggested by XRD profiles. Figure 3.9 shows the calculated spectra with a vacancy occupied at the Ga^a, Ga^{cu} and Ga^{cd} site described in Fig. 3.4. I average the calculated Ga vacancy spectra for each equivalent Ga site. For comparison, the experimental and calculated no Ga vacancy spectra are also shown in Fig. 3.9. Remarkably, the Ga^{cd} vacancy normal to the polarization direction change the intensity ratio between the main peak and shoulder though Ga^a and Ga^{cu} vacancies does not affect on the spectra. However, the spectral change by Ga^{cd} does not improve the calculated result substantially, and is small to conclude the existence of the Ga vacancy. In addition, creation energy of a Ga vacancy is higher than that of a nitrogen vacancy adjacent to a doped Gd ion [69]. Hence, I do not put stress on Ga vacancies in the present thesis.

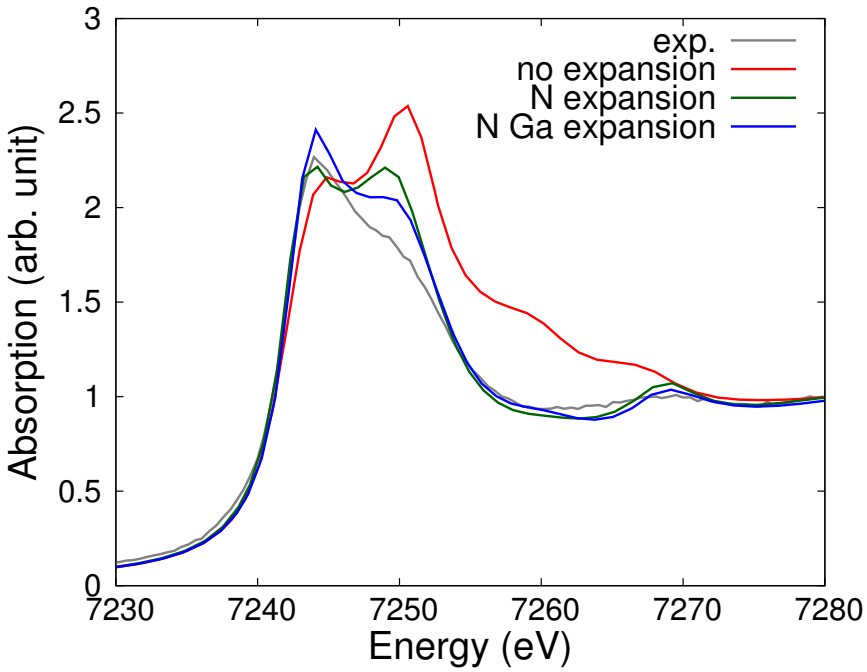

Figure 3.8: The calculated Gd L_3-edge XANES spectra by using the no vacancy model with no expansion, only the Gd-N bond expansion, and the Gd-N and -Ga distance expansion. The observed Ga-rich spectrum is also shown for comparison.

For the N-rich spectrum, I calculate XANES spectra by using the vacancy models. Figures 3.10(i) and (ii) show the XANES spectra calculated with the one vacancy models (a) and (c) in various Gd ion shifts, respectively. The Gd ion shift decrease the calculated shoulder intensity in both the one vacancy models because space around the Gd ion increase to approach the free atom state. The calculated tail above the shoulder is also improved by the Gd ion shift. In Fig. 3.10(i), the main peak intensity shows complicate changes as increasing shifted distances in contrast to that in Fig. 3.10(ii). This may reflect the local site symmetry around the Gd ion: the C_{3v} symmetry is broken in the model (a), but kept in the model (c). Note that Gd-Ga distances ($\sim$ 2.43 Å) are closer than Gd-N ones ($\sim$ 2.46 Å) in the Gd ion shifts 1.0 Å, so that the shifts should be less than 1.0 Å to keep consistency with the EXAFS result (Gd-N 2.23 Å [51]). The calculated shoulder in the model (a) is weaker than that in the model (c) with Gd ion shift less than 1.0 Å.

Figures 3.11(i) and (ii) show the XANES spectra calculated with the two vacancies

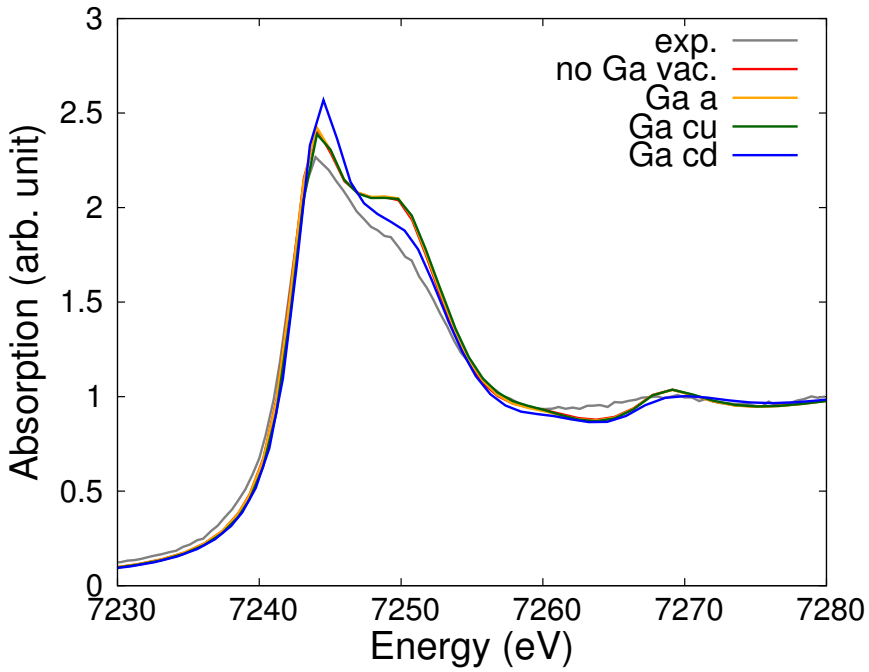

Figure 3.9: The calculated Gd L_3-edge XANES spectra by using the one Ga vacancy model with the Gd-N and -Ga distance expansion. The Ga site indices are defined in Fig. 3.4. The observed Ga-rich spectrum is also shown for comparison.

models (aa) and (ac) in various Gd ion shifts, respectively. In the case of the models (aa) and (ac), the Gd ion is shifted to bisection between the two nitrogen vacancies as shown in Fig. 3.6. The Gd ion shift changes the calculated spectra in both the two vacancies models in the same tendency as in the one vacancy models. The calculated main peak width in the two vacancies models shows better agreement than that in the one vacancy model. The calculated shoulder in the model (aa) is weaker than that in the model (ac) with Gd ion shift less than 1.0 Å.

If I focus on agreement of the calculated shoulder intensity with the observed one, I conclude that a nitrogen vacancy preferentially occupies at a N^a site than at the N^c site in the N-rich GaN:Gd sample. In particular, the calculated spectra by using the model (aa) with 0.5 Å shifts show the smooth spectral shape similar to the observed one. However, two nitrogen vacancies creation seems not to be feasible in terms of their creation energy. Furthermore, a first principle calculation suggests that the Gd ion shift due to the vacancy creation is small and the change of bond lengths is less than 1.5 % [69].

I also find that large Gd ion shifts in the order of 0.1 Å are required to change a calculated spectral structure substantially. This indicates that nitrogen vacancies adjacent to doped Gd ions does not relate to lattice-expansion relaxation, and could not explain the XRD profile of the N-rich GaN:Gd crystal [22]. Therefore, it is difficult to determine the best calculation model by shoulder intensity in XANES spectra of GaN:Gd crystals with only horizontal X-ray polarization. Alternatively, I performe polarization-dependent XANES analyses to obaing more information about vacancies in the next section.

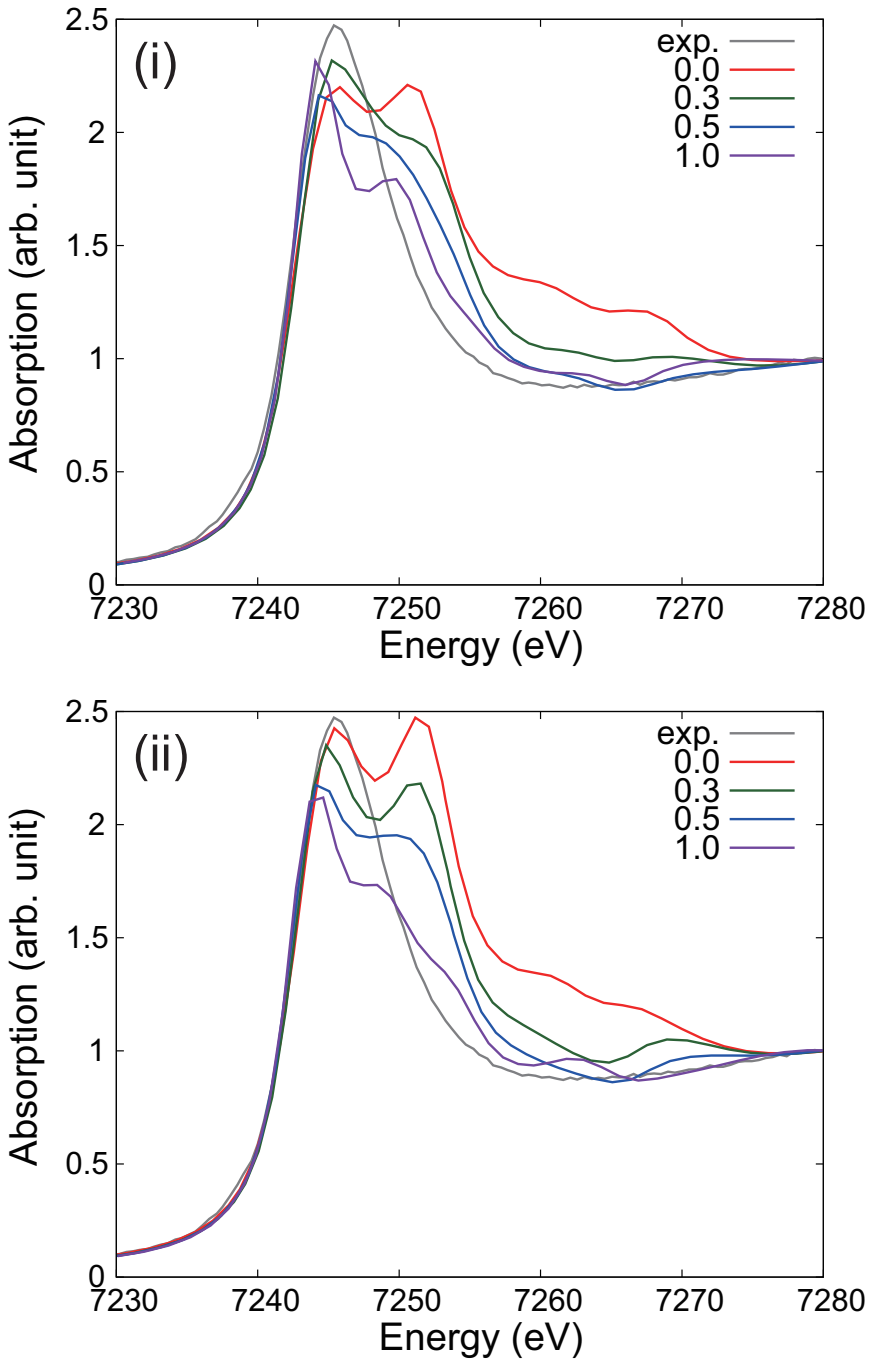

Figure 3.10: The calculated Gd L_3-edge spectra by using the model (a) and (c) ((i) and (ii), respectibely) with Gd shifts 0.0, 0.3, 0.5 and 1.0 Å toward the vacancy. The observed N-rich spectrum also shown.

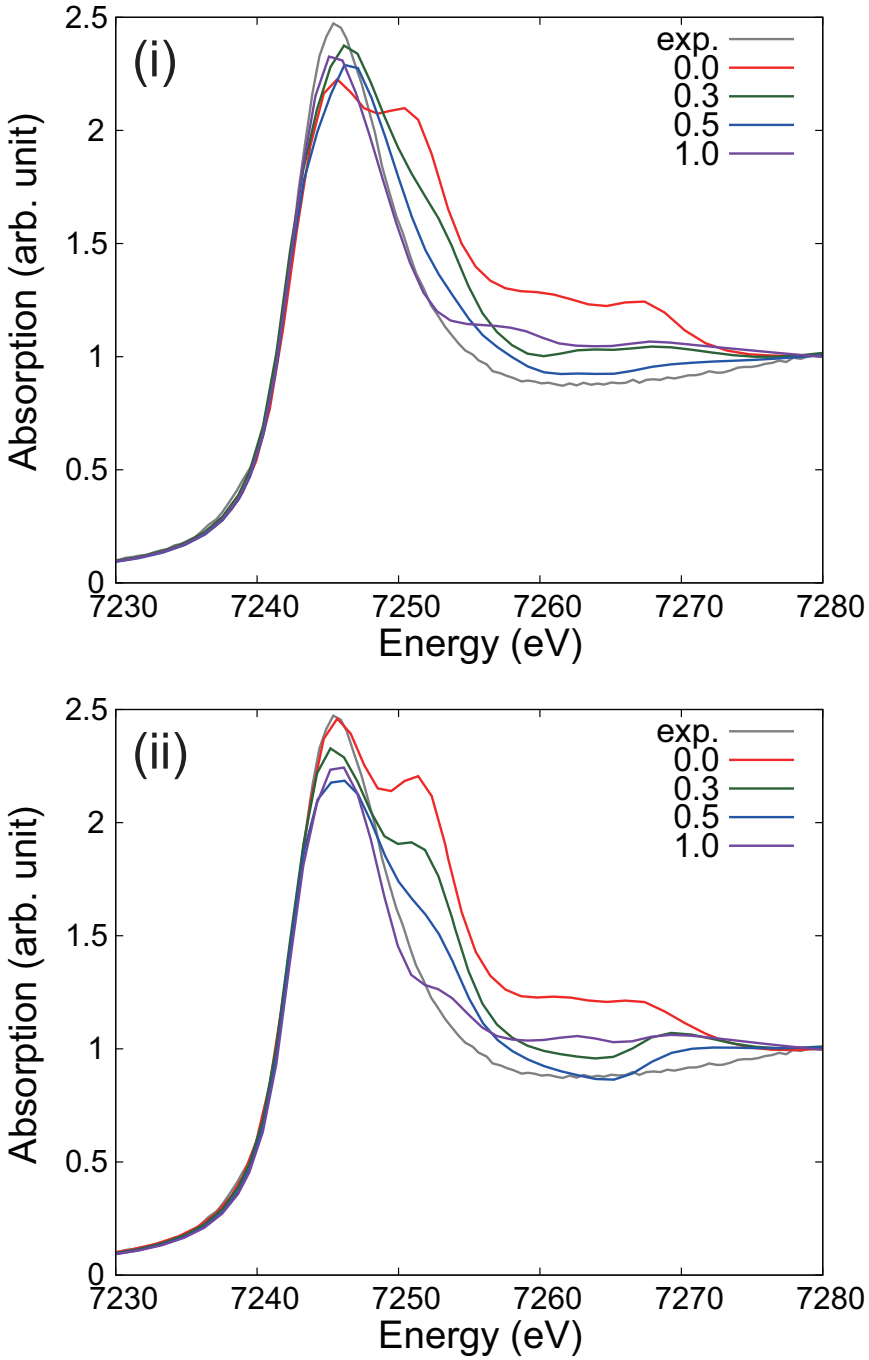

Figure 3.11: The calculated Gd L_3-edge spectra by using the model (aa) and (ac) ((i) and (ii), respectibely) with Gd shifts 0.0, 0.3 0.5 and 1.0 Å toward the bisection between the two vacancies. The observed N-rich spectrum also shown.

3.3 GaN:Dy

3.3.1 Experimental

The Ga-rich and N-rich GaN:Dy samples were prepared under the same condition as the GaN:Gd ones described in Sec. 3.2.1. I observed Dy L_3- and L_1-edge polarization-dependent XANES spectra of the Ga- and N-rich GaN:Dy samples, and DyN as a reference at a beamline BL9A in PF, KEK The Dy L_3- and L_1-edge energies in literature are 7850 and 9083 eV, respectively [58]. The $L_{\alpha_{1,2}}$ fluorescence lines of Dy (L_{α_1}:6057.2 eV and L_{α_2}:6025.0 eV [59]) were detected by using a solid-state detector (SSD, Ge:Li) with 19 elements to obtain the L_3-edge spectra with a fluorescence mode. In the same way as the L_3-edge, the $L_{\beta_{3,4}}$ fluorescence line of Dy (L_{β_3}:7203.9 eV and L_{β_4}:7370.2 eV [59]) were detected for the L_1-edge spectra. The synchrotron radiation storage ring ran at electron energy of 2.5 GeV and in an electron current of 450 mA in top-up operation. The beamline BL9A was installed with a Si (111) double-crystal monochromator and a pseudo-conical shape mirror to collimate incident X-rays. Monochromatized synchrotron radiation was focused on the sample by a second pseudo-conical shape mirror with a 1 mm×1 mm beam size. The X-ray energy was calibrated at the pre-edge of the Cu foil (12.7185°). Figure 3.12 shows a schematic image of experimental settings. The spectra were recorded by using a solid-state detector (SSD, Ge:Li) with 19 elements. A high purity (99.95%) aluminum pipe with a length of about 250 mm and a diameter of about 30 mm was introduced just before and after the sample and ion chamber I0, respectively, to prevent the detector from counting X-rays scattered by air in the incident X-ray path to the sample. The typical sample size is 5 mm in width and 10 mm in length. A sample was set on a stand surface angled 7° to the incident X-ray beam to widely expose the sample to X-rays. The incident X-ray is linearly polarized in the horizontal direction parallel to the ground. To obtain the polarization dependence of the XANES spectra, the sample stand moves around the incident X-ray path in a crescent (semicircular) arc centered on the X-ray beam and sample position. Rotating the crystal in the crescent (semicircular) arc enables us to change polarization angles to the crystal surfaces and perform polarization-dependent measurements. Figure 3.13 shows the crescent arc and definition of polarization angles.

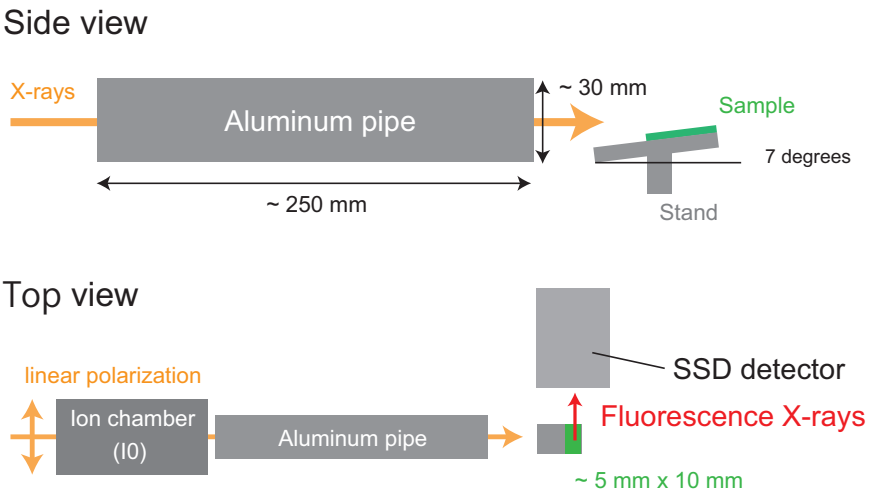

Figure 3.12: A schematic image of experimental settings from side (upper part) and top (lower part) views.

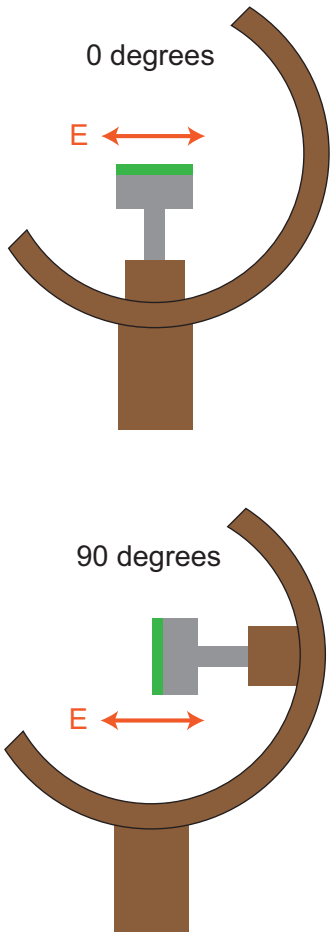

Figure 3.13: A crescent arc to obtain polarization-dependent XANES spectra. The polarization direction of incident X-rays and definition of polarization angles are also shown.

Incident X-rays were linearly polarized parallel to the ground. The polarization angle 0° is defined as parallel to the sample surfaces or normal to the c-axis of the crystal layers. Other angles, such as 30°, 60°, and 90°, indicated hereafter give the rotating angles from the 0° on the crescent arc. Thus, defined angles differed slightly from the actual angles between the polarization and the c-axis because of the slope of the stand surface. XANES spectra were recorded in 0.35 eV energy steps accumulated over 10 s per point at room temperature.

3.3.2 Calculation

To investigate the local structure around a doped Dy ion from the XANES analyses, four structure models are examined. Figure 3.14 shows the nitrogen sites next to a Dy ion in the no-vacancy (n) and three one-vacancy models. The models (a) and (c) have one V^a and V^c (c) vacancy, respectively. Since there are three equivalent V^a sites, we average the calculated results for each V^a sites in the model (a). The average model (av) uses the averaged XANES spectra obtained by

$$\sigma(\mathrm{av}) = \frac{3}{4}\sigma(\mathrm{a}) + \frac{1}{4}\sigma(\mathrm{c}) \tag{3.1}$$

where σ(a), σ(c) and σ(av) are those for the one-vacancy models (a), (c) and (av). The average is taken on the assumption that the N^a and N^c vacancies can be found with the same probability. All the models are based on the wurtzite structure of GaN. The lattice constant and atomic coordination of the GaN unit cell are obtained from XRD measurements [68] . One Dy atom substitutes a Ga site at the center of the model clusters, which is composed of about 165 atoms. Table 3.2 shows the Dy-N^a and -N^c distances are 2.240 and 2.263 Å, respectively. Their averaged distance is 2.246 Å, which is determined by EXAFS analyses [43]. Similarly, in Table 3.2 the Dy-Ga^a and -Ga^c distances in the second Ga shell are chosen as 3.306 and 3.297 Å, respectively: their average distance is 3.302 Å by EXAFS analyses [43]. The structures beyond the third shell in the cluster are set to be the same as those of GaN [68]. In the calculations, polarizations of 0° and 90° designated the linear polarization normal (0°) and parallel (90°) to the c-axis.

Table 3.2: Atomic distances in Dy systems and GaN.

Atomic pairs	GaN:Dy (Å) [43]	GaN (Å) [68]	DyN (Å) [52]
Gd(Ga)-N^a	2.240	1.945	2.450
Gd(Ga)-N^c	2.263	1.965	2.450
RE(Ga)-Ga^a(RE)	3.306	3.189	3.464
RE(Ga)-Ga^c(RE)	3.297	3.180	3.464

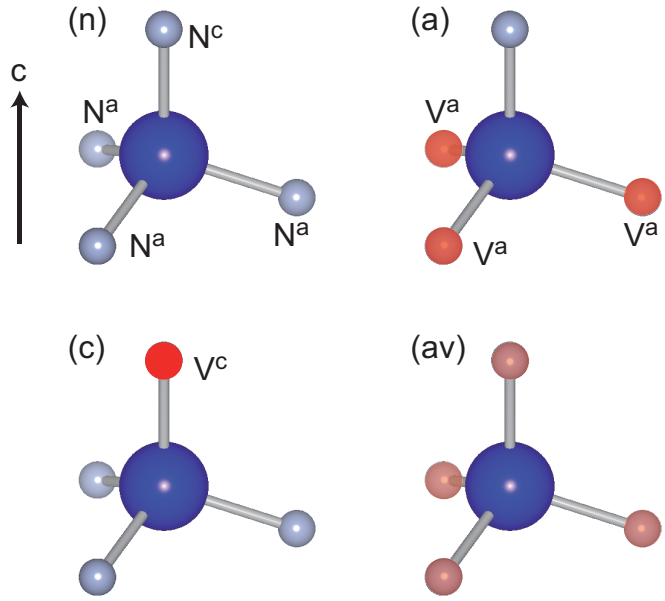

Figure 3.14: Nitrogen and its vacancy sites next to a Dy ion in calculation models: no vacancy (n); one V^a (a) and one V^c (c) vacancies. In the model (a), the calculated spectra are averaged for three equivalent V^a sites. The calculated spectra averaged for all the nitrogen vacancies corresponds to the average model (av) one.

3.3.3 Results

The observed DyL_3-edge XANES spectra of the Ga- and N-rich samples are compared with the Gd ones for the polarization normal to the c-axis in Figure 3.15. For the comparison, the energy position of the spectra is shifted. Fig. 3.15 shows that the Dy spectra reproduce the Gd ones. This indicates that the spectral difference between the Ga- and N-rich crystals is not sensitive to the RE elements. Therefore, we can discuss

GaN:Dy spectral feature in the same way as the GaN:Gd ones, and vice versa. The small spectral difference supports that multiplet effects are not dominant as described in Sec. 3.2.2 because the difference of the number of 4f electrons has only small contribution to the spectra.

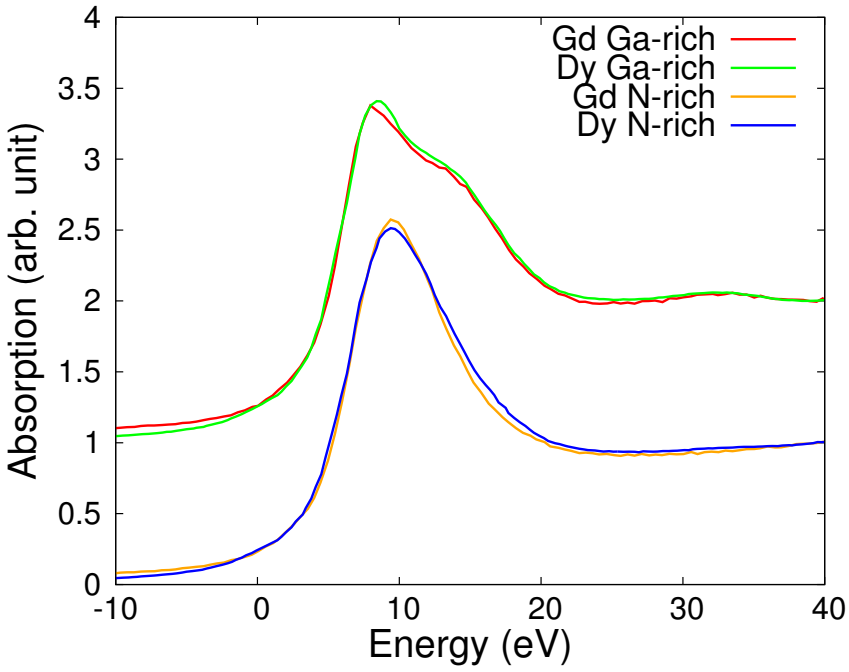

Figure 3.15: Observed Gd and Dy L_3-edge XANES spectra of the Ga- and N-rich GaN:RE samples for the polarization normal to the c-axis. The main peak energy of both the N-rich samples is adjusted to 10 eV. The energy interval between the Ga- and N-rich spectra is kept. All the spectra are normalized to the intensity at 40 eV.

The observed Dy L_3-edge XANES spectra of the all samples are shown for the polarization 0° and 90° in Figure 3.16(i), which are normalized to the intensity at 7814 eV. DyN has a NaCl structure, and should show no polarization dependence. Unfortunately, I observed Dy L_3-edge spectra only for the polarization 0°, and show it in Fig. 3.16(i). The Ga-rich spectra gives a shoulder around 7797 eV and a hump around 7815 eV, whereas the N-rich one gives no shoulder and only a tiny hump around 7815 eV. These samples show different energy positions of a main peak. Spectral differences are also observed in the L_1-edge XANES spectra. Figure 3.16(ii) shows the observed XANES spectra at Dy L_1-edge in the same way as Fig. 3.16(i). The L_1-edge spectra are normalized to the main

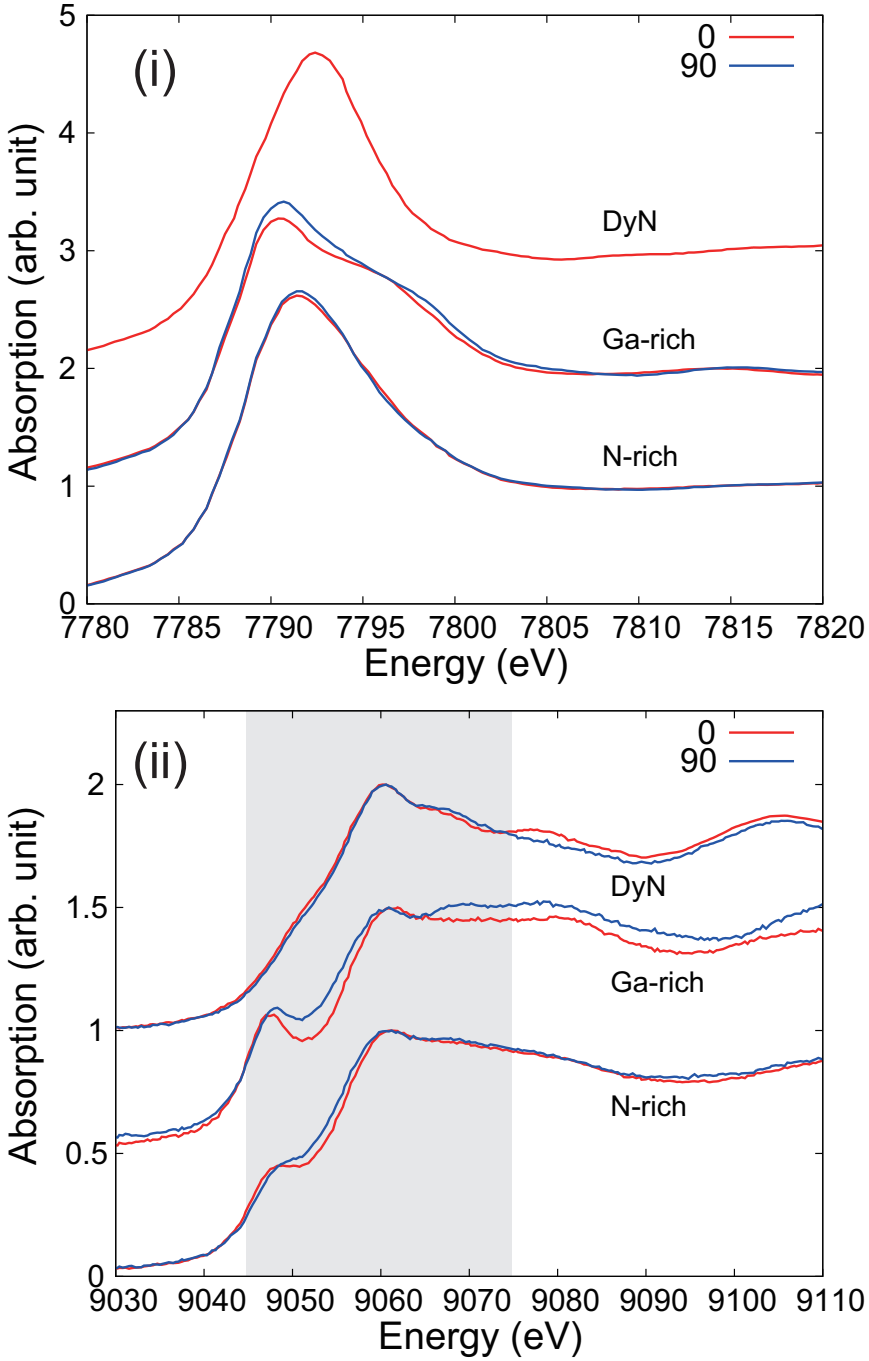

Figure 3.16: Observed Dy (i) L_3- and (ii) L_1-edge XANES spectra of the Ga- and N-rich GaN:Dy samples, and DyN crystal.

peak intensity at 9000 eV. Owing to somewhat rippled background below 9030 eV (not shown), I do not take the background subtraction. Therefore, it is hard to discuss the change of spectral intensities in these spectra. Furthermore, the Dy L_1-edge spectra of DyN show polarization dependence that should not be appears for the rock-salt structure. I thus focus on the behavior in the shaded region where effects of the background and the DyN polarization dependence are small in Fig. 3.16(ii). Remarkable features in the Ga- and N-rich spectra are prominent pre-edge peaks at about 9047 eV: comparing with the Ga-rich spectra, we notice that the pre-edge peak of the N-rich spectra is smaller. On the other hand, the observed DyN spectrum shows a negligibly small pre-edge peak.

The appearance of the pre-edge peaks can be interpreted by a simple molecular orbital picture. The X-ray absorption at L_1-edge is generally assigned to electron dipole and quadrupole transitions from the $2s$ core orbital. The dipole (quadrupole) transitions give rise to the excitation from the $2s$ core orbital to an unoccupied p (d) orbital. Pre-edge peaks typically correspond to the transitions to bound states, and reflect the local electronic structure through the orbital hybridization within the framework of the molecular orbital picture. If local tetrahedral symmetry is assumed around a trivalent Dy ion doped in GaN, the structure has no centrosymmetry and induces the orbital hybridization between the $5d$ and $6p$ orbitals through the static crystal field. Although the electron-phonon interaction providing strong temperature dependence also contributes to the orbital hybridization, the vibrational effect should be weaker than the symmetrical one [70]. Since the dipole transition is dominant in comparison with the quadrupole one (usually, $100 \sim 1000$ times less than the dipole), the p-d hybridization enhances the pre-edge peak intensity in K and L_1-edge XANES spectra. The enhancement has been reported for trivalent iron chloride compounds, which have the local tetrahedral structure [71]. The pre-edge peak in the iron K-edge spectra of those systems was assigned to the $1s$-$3d$ dipole forbidden transition because the p-d orbital hybridization partially allows the parity forbidden transitions. In addition, the almost zero occupancy of $5d$ electron in trivalent Dy ion also enhances the pre-edge intensity. Thus, we can assign the observed strong pre-edge peak to the $2s$-($5d$+$6p$) dipole transition.

The final state effect related to pre-edge peaks in K-edge XANES spectra has been well studied for various Cu compounds which have a plane or a linear structure [72, 73, 74].

However, doped RE ions hardly take such low dimensional structures in the wurtzite GaN. In addition, the localized $4f$ orbital in RE ions never contribute to direct dipole and quadrupole transitions, has negligible orbital hybridization owing to its strong atomic character. Thus, I conclude that the $5d$-$6p$ hybridization gives rise to the prominent pre-edge peak for the Ga- and N-rich GaN:Dy crystals. On the other hands, the rock-salt DyN has centrosymmetry and the $5d$-$6p$ hybridization is caused only by electron-phonon interaction. This interaction only induces a weak transition moment. Consequently, the L_1-edge DyN spectrum has a negligible pre-edge peak. These interpretations from the pre-edge only indicate non inversion symmetry of Dy ion sites accutually, which suggests that Dy ions are successfully doped in wurtzite GaN. However, EXAFS analyses provided us acceptable results by using the local quasi-tetrahedron centered by a Dy ion [43]. The L_1 pre-edge result hence has no contradiction to and supports Dy ion substitution at Ga sites in GaN, which occupies the center of a quasi-tetrahedron. This conclusion agrees with the GaN:Gd case described above, and the previous reports [22, 41].

Polarization dependences are observed in the L_3- and L_1-edge XANES spectra in Fig. 3.16(i) and (ii), respectively. For the L_3-edge XANES spectra, the polarization dependence is clearly observed for the Ga-rich sample, and slightly for the N-rich one. For L_1-edge XANES spectra, the similar polarization dependence is also observed. This polarization dependence is not broken at the polarization angles 30° and 60° (not shown), and analyzed by using multiple scattering calculations in the next section.

3.3.4 Discussion

As described in 3.3.2, I study the four calculation models (n), (a), (c) and (av), which involve the two nitrogen vacancy sites on N^a sites, and on the N^c site. Figures 3.17(i) and (ii) show the calculated Dy L_3- and L_1-edge XANES spectra normalized to the intensities at 7814 and 9062 eV, respectively. The observed Ga-rich spectra are also shown in Fig. 3.17.

In Fig. 3.17(i), all of the calculated spectra show a shoulder and a hump similarly to the observed Ga-rich spectra. In Fig. 3.17(ii), the spectral shapes of all the L_1-edge spectra calculated at 0° are similar to those of the observed ones. In particular, all the calculated L_1-edge spectra show the prominent pre-edge structure below 9050 eV.

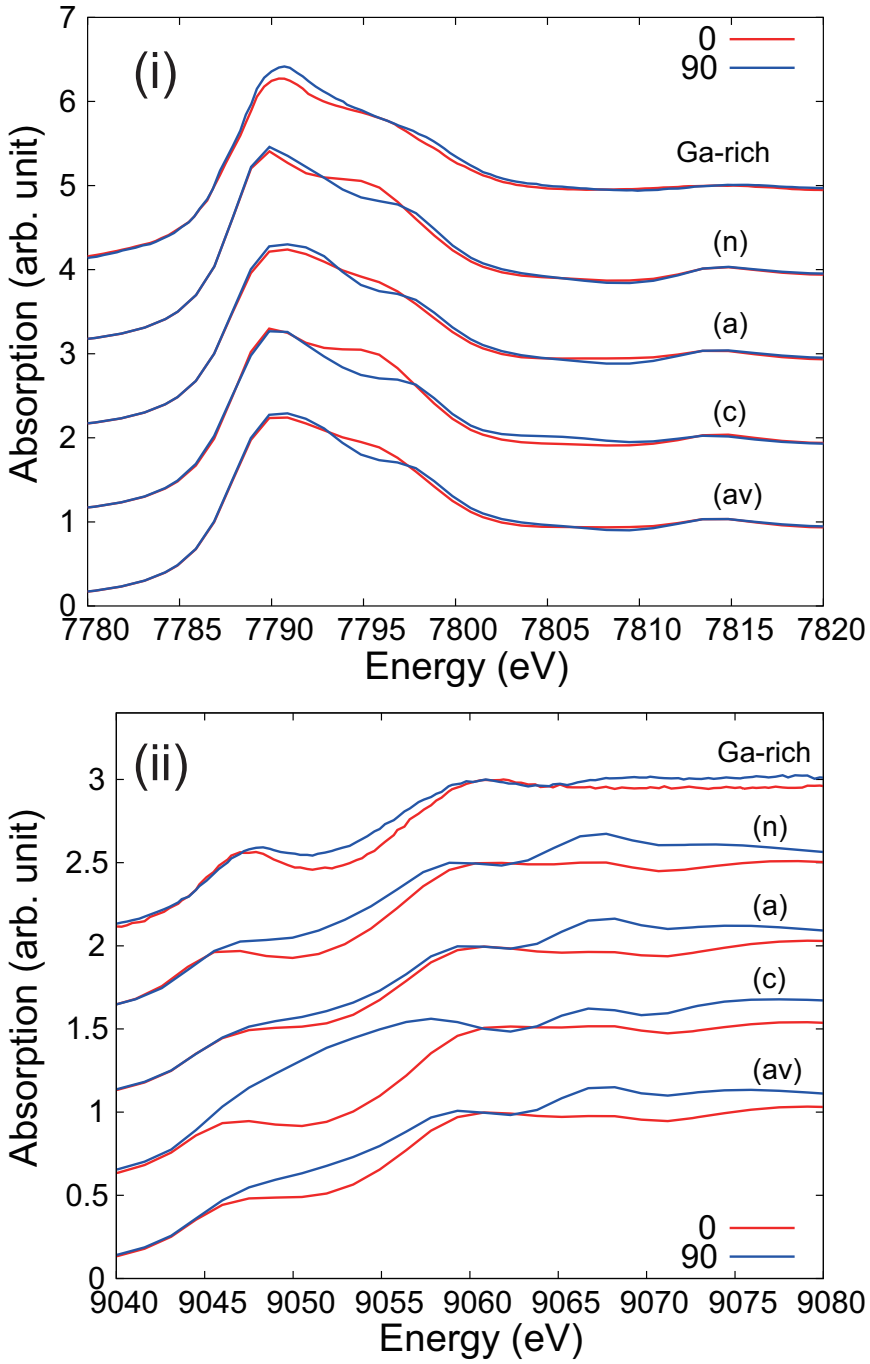

Figure 3.17: The calculated Dy L_3- (i) and L_1-edge (ii) spectra by using the models (n), (a), (c) and (av) compared with the observed one for the Ga-rich sample.

The MS calculations here do not include the quadrupole transition, the electron-phonon interaction and the final state effects, which give rise to pre-edge peaks in some particular transition metal compounds [72, 73, 74]. The present calculations only include the local geometrical effect to enhance the pre-edge peak. The above result suggests that the observed pre-edge peak should originate from local structural symmetry around a doped Dy ion. Hence, the MS calculations support the pre-edge consideration described in the previous section: a Dy ion is located at a center of local quasi-tetrahedron.

The calculated polarization dependence gives information of the nitrogen vacancy site in GaN:Dy. The spectra calculated with the model (c), which has a nitrogen vacancy on the c-axis, as shown in Figs. 3.17(i) and (ii) show the different polarization dependence compared with the observed Ga-rich spectra. In Fig. 3.17(i), the main peak at 7790 eV is nearly the same for both polarizations, and the intensity at about 7795 eV at 0° is too strong in the calculated XANES for the model (c). Moreover, in Fig 3.17(ii), the calculated spectra (c) show too large polarization dependence. These features differ from the observed ones. The model including only the N^c vacancy therefore cannot explain the observed spectral feature for the Ga-rich crystal. On the other hand, the calculated spectra (a), (c) and (av) show the comparatively good agreement with the observed Ga-rich spectra. The models for (n) and (a) have no-vacancy and one N^a-vacancy, respectively, while for (av) has some weights of (a) and (c) averaged over the N^a and N^c vacancy sites. The model (av) represents a randomly occupied nitrogen vacancy next to a doped Dy ion, i.e. contribution of V^a to XANES spectra is 3 times as large as that of V^c because of three equivalent V^a sites. I conclude eventually that a N^a site is more plausible than the N^c site as a position of a nitrogen vacancy if it exists adjacent to a doped RE ion in the Ga-rich GaN:RE crystal. This vacancy anisotropy reflects Ga-N bond distances. The nitrogen site N^a connects with Dy, $Ga^a$and Ga^{cd}, while N^c with Dy and Ga^{cu}.

The N-rich sample was expected to be nitrogen-vacancy rich by the consideration from XRD profiles of N-rich GaN:Gd [22, 77]; a GaN substrate reflection was only observed in the XRD profile and appears to arise from cancellation of local atomic disorder by lattice relaxation through vacancies. However, in Figs. 3.17(i) and (ii), all the calculated spectra show clear polarization dependence which is influenced by a nitrogen vacancy.

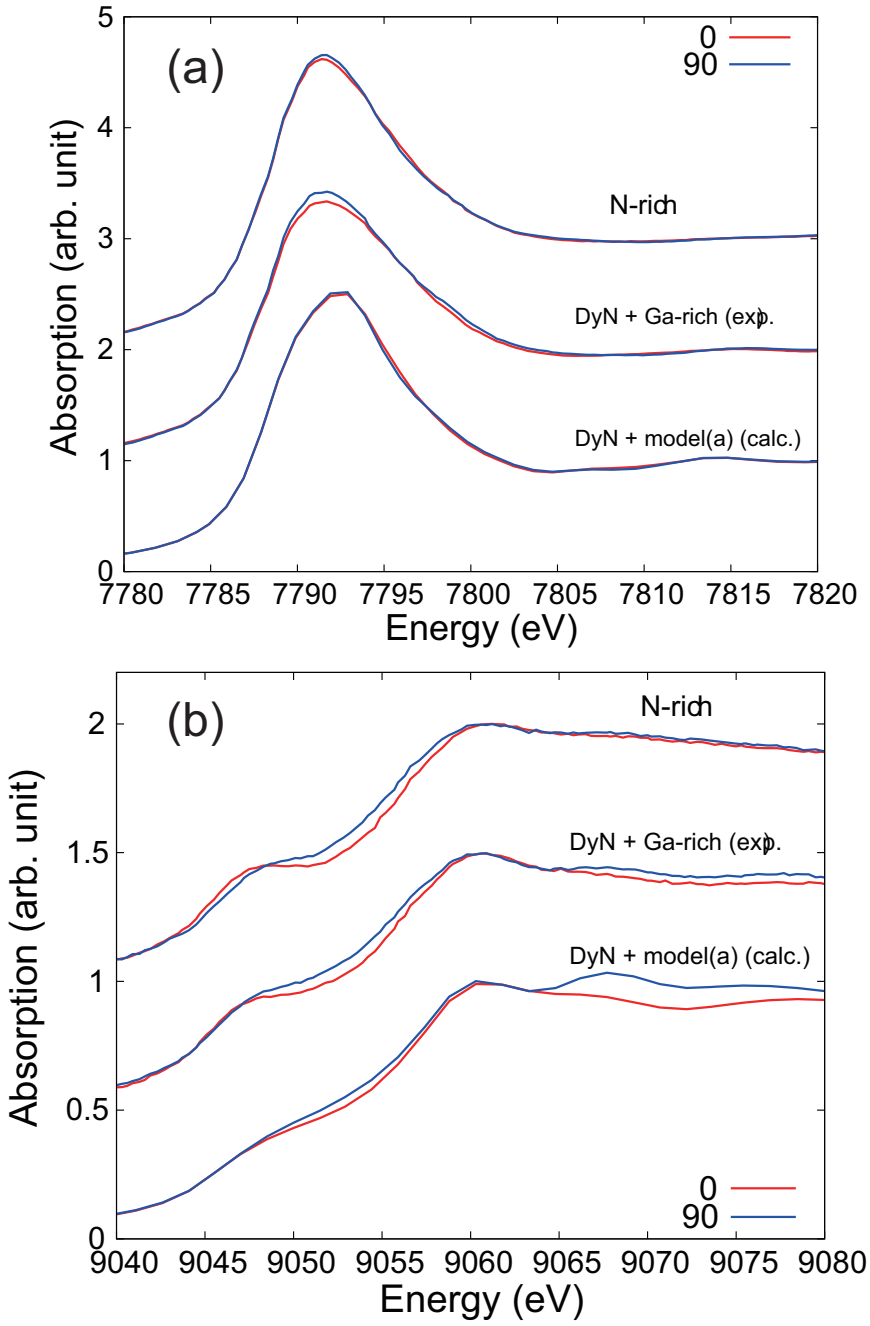

Figure 3.18: The observed and calculated Dy L_3- (a) and L_1-edge (b) spectra averaged over the Ga-rich GaN:Dy sample and DyN. The observed N-rich spectra also shown for comparison.

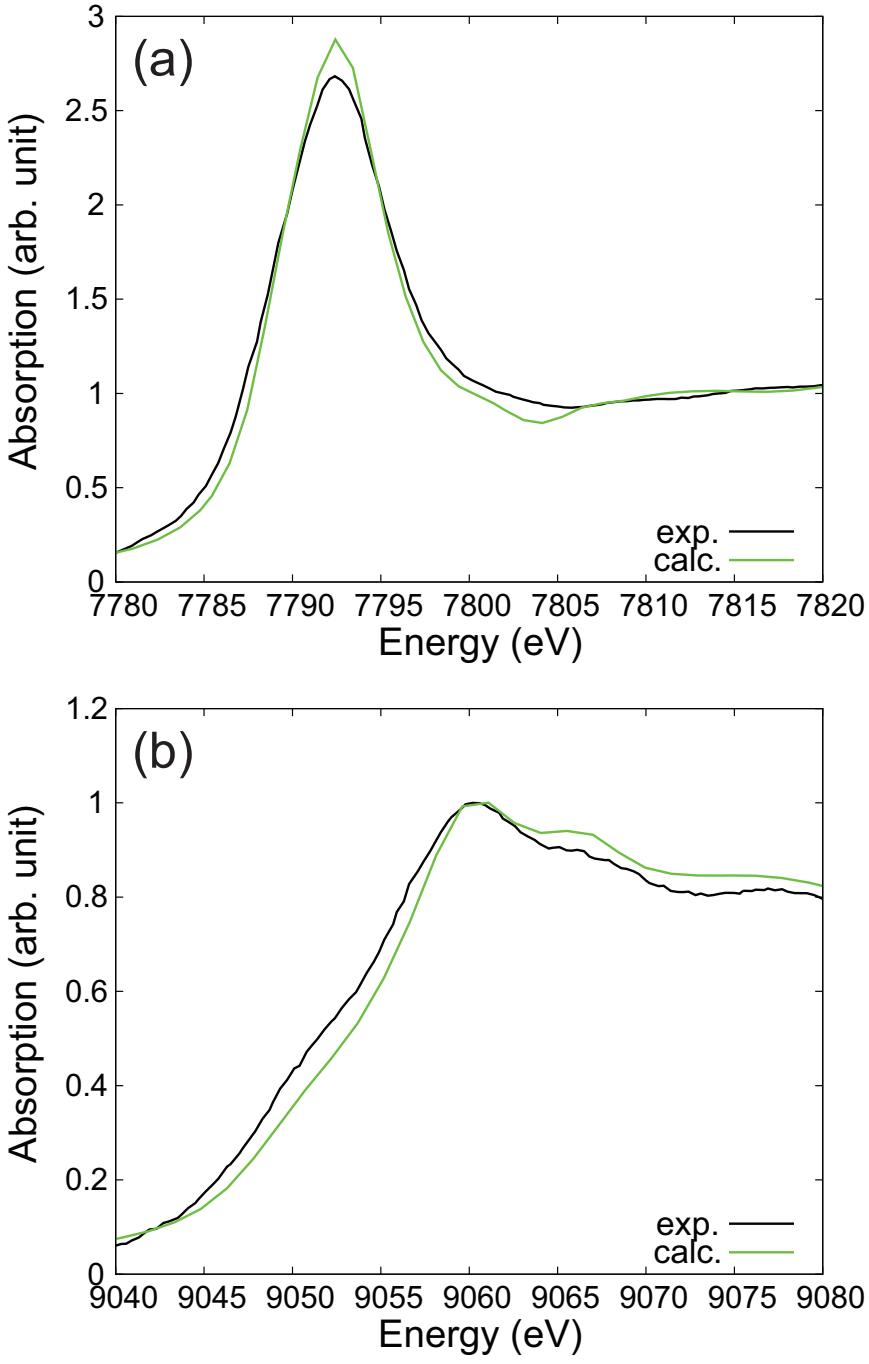

Figure 3.19: The calculated Dy L_3- (a) and L_1-edge (b) spectra of DyN. The observed spectra with the polarization normal to the c-axis (0°) are also shown for comparison.

The N-rich crystal gives rise to the weak polarization dependence as shown in Fig. 3.16(i). One possibility of the origin of the weak dependence is mixture of spectra for isotropic structural compounds. To explain the observed spectral features shown in Fig. 3.16 for the N-rich crystal, I focus on effects of DyN segregation to the XANES spectra. Figure 3.18(a) (3.18(b)) shows the L_3-edge (L_1-edge) XANES spectra mixed with the Ga-rich GaN:Dy and DyN ones with the same weights. The experimental mixed spectra used the sum of the observed Ga-rich GaN:Dy and DyN spectra; however the DyN spectra for 0° was only chosen to construct the mixed spectra because of the absence of the DyN L_3-edge spectra for 90°. The calculated mixed spectra used the calculated DyN spectra and N^a-vacant model (model (a)) ones as the Ga-rich. They show good agreement with the observed N-rich spectra: they have the small polarization dependence at L_3- and L_1-edges. The weak polarization dependence is well explained by the mixture of the DyN spectra because I assume the DyN spectra have no polarization dependence, which is justified in principle for the rock-salt structure. Although the DyN L_1-edge spectra slightly have polarization dependence as shown in Fig. 3.16, the deviation is sufficiently small to reduce the polarization dependence. Moreover, the N-rich crystal growth condition seems to support the DyN generation. Figures 3.19(a) and (b) show the calculated DyN spectra, which well agree with the observed ones. Thus, the discrepancy, which is small but remain, between the observed and calculated mixed spectra is mainly caused by the calculated Ga-rich (model (a)) spectra. However, perfect agreement of calculated results is impossible and not realistic because I do not include complicate distortions, other structural small contribution and anharmonic oscillation arisen from vacancies. In addition, segregated DyN crystals in the N-rich GaN:Dy sample may deviate from pure DyN ones. The present calculations sufficiently provide us information about dominant contribution to the observed XANES spectra.

I also consider the meaning of the 1:1 superposition of the Ga-rich GaN:Dy and DyN spectra. In this discussion, the followings are assumed for simplicity: i) the Dy ion doped in the GaN matrix substitute a Ga site without volume changes in the supercell of Ga99DyN100; ii) the state of GaN:Dy (N-rich) before DyN segregation is the same as that of GaN:Dy (Ga-rich); iii) the total volume of GaN:Dy (N-rich) and the number of the Dy ions are conserved before and after the segregation.

Table 3.3: Volume of a unit cell and the number of atoms.

Compound	Volume of a unit cell (Å^3)	Atoms in a unit cell
GaN	45.672	Ga_2N_2
GaN:Dy (Ga-rich)	2283.6 (50 GaN cells)	$Ga_{99}Dy_1N_{100}$
DyN	117.65	Dy_4N_4

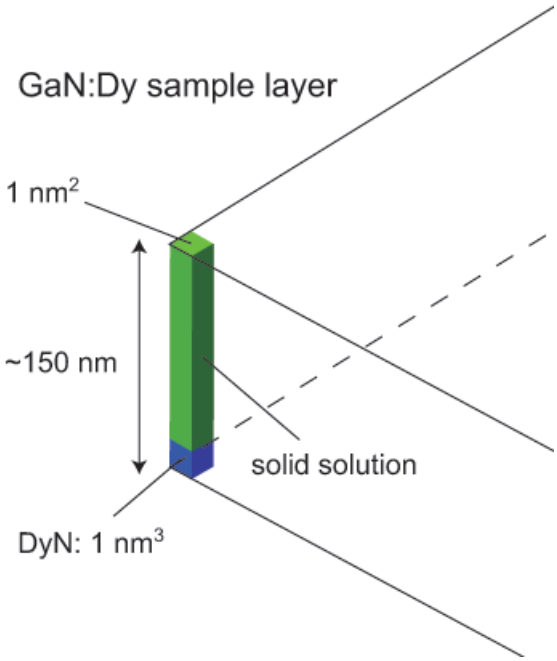

Figure 3.20: A schematic image of segregated DyN nanocrystals in the N-rich sample.

Table 3.3 gives the volume of a unit cell of GaN, GaN:Dy (Ga-rich) and DyN, and the number of atoms in the unit cell. The same weight of the GaN:Dy (Ga-rich) and DyN corresponds to the same number of Dy ions in the two phases. From Table 3.3, the volumes occupied by one Dy ion in GaN:Dy (N-rich) before the segregation and in DyN are 2283.6 and 29.412 Å^3, respectively. Therefore, the volume of the segregation of DyN is 0.643 % of the total volume of GaN:Dy (N-rich). This percentage is nearly the same as that of a 1 nm^3 cube in a 1 nm × 1nm × 150 nm pillar: 0.666 %. The height 150 nm corresponds to the thickness of the present GaN:Dy sample layer. A schematic image of the segregation is depicted in Figure 3.20. The EXAFS analysis and the XRD profiles show no clear segregation in GaN:RE crystals [22, 43]. Therefore, I could conclude that

DyN disperses as nanocrystals in the N-rich sample. The segregation may lower the crystal quality, and broaden the reflection intensity from the sample layers. It is known that crystal growth of high quality GaN under N-rich conditions is more difficult than under Ga-rich or stoichiometric conditions. In addition, deviation of reflection peak energy from a GaN template one according to Vegard'law [47] is reduced because RE ions in GaN:RE phase are drained by RE nitride phase. These effects may bury the N-rich crystal reflection in a GaN substrate one.

I discuss energetic aspects of DyN segregation by using the law of mass action. I consider following equilibrium states.

$$\mathrm{Ga_{99}Dy_1N_{100}} + \Delta G \;\rightleftarrows\; 99\,\mathrm{GaN} + \mathrm{DyN}, \tag{3.2}$$

where ΔG is the Gibbs free energy increase. From the law of mass action,

$$\frac{[\mathrm{GaN}]^{99}[\mathrm{DyN}]}{[\mathrm{Ga_{99}Dy_1N_{100}}]} = e^{-\frac{\Delta G}{RT}}, \tag{3.3}$$

where $[\cdots]$ is amount of substance for each compound, and R is the gas constant (R=8.3145). For simplicity, I approximate ΔG by a sum of standard enthalpies of formation. Table 3.4 shows each standard enthalpies of formation ΔH_f^0 and estimated bond-dissociation energiesΔH_b^0, for instance, $\Delta H_{b,GaN}^0 = -\Delta H_{f,GaN}^0/2$ because of 4 bonds per atom in GaN. By using $\Delta H_{b,GaN}^0$, I also estimate ΔH_f^0 of $\mathrm{Ga_{99}Dy_1N_{100}}$ defined as

$$\Delta H_{f,GaDyN}^0 = 100\ \Delta H_{f,GaN}^0 + 4\ \Delta H_{b,GaN}^0 - 4\ \Delta H_{b,DyN}^0. \tag{3.4}$$

The obtained $\Delta H_{f,GaDyN}^0$ is also shown in Table 3.4. The approximated ΔG is then written as

$$\Delta G = 99\ \Delta H_{f,GaN}^0 + \Delta H_{f,DyN}^0 - \Delta H_{f,GaDyN}^0. \tag{3.5}$$

For RE = Dy, ΔG_{Dy} = -75.648 kJ/mol is obtained within the approximation. I assume that final amount of substance of DyN is x mol, and initial amount of substance of GaN:Dy is 1.0 mol. In other words, final amounts of substance of GaN and GaN:Dy are $99x$ and 1-x mol, respectively. Thus, a desired equation is

$$\frac{99x^{100}}{1-x} = e^{-\frac{\Delta G}{RT}}. \tag{3.6}$$

Table 3.4: standard enthalpies of formation and bond-dissociation energies.

Compound	ΔH_f^0 (kJ/mol)	ΔH_b^0 (kJ/mol)
GaN	-129.29 [75]	64.6445
GdN	-157.88 [76]	52.6267
DyN	-160.92 [76]	53.6400
$Ga_{99}Gd_1N_{100}$	-12880.9	
$Ga_{99}Dy_1N_{100}$	-12885.0	

The positive real solution $x \sim 1.0$ for RE = Dy is obtained at $T = 298.15$ K, indicating that GaN:Dy inherently prefer the DyN segregation. The contribution of the entropy to the Gibbs energy of formation $\Delta G^0_{f,GaN}$ is 30.548 kJ/mol at 298.15 K [75], which is the order of 10^{-1} with respect to $\Delta H^0_{f,GaN}$. Therefore, the contribution of the entropy to ΔG_{Dy} is the order of 1 kJ/mol. Furthermore, this rough estimate does not include effects of vacancies, pressure of nitrogen gas and and so on. However, even if those contributions is the same order of $\Delta H^0_{f,GaN}$, $\exp(-\Delta G/RT) >> 1$ at 298.15 K, leading to the same conclusion of $x \sim 1$. Indeed, x is 0.93002 when $\exp(-\Delta G/RT) = 1$. In addition, GaN:RE samples are prepared by the molecular beam epitaxy technique in non-equilibrium processes because GaN:Dy is unstable compared with GaN in terms of ΔH^0_f. Therefore, I only mention that DyN could segregate in GaN:Dy.

3.4 Discussion for GaN:Gd

The previous section 3.2.3 shows that large Gd shifts ($\sim$ 0.5 Å) to space created by vacancies are needed to explain the no-shoulder spectrum of the N-rich GaN:Gd sample. The such large shifts may not be feasible from energetic aspects [69]. In the GaN:Dy section 3.3.4, I have discussed polarization dependence and DyN segregation in GaN:Dy samples. Now I go back to the spectrum of the N-rich GaN:Gd crystal to consider nitrogen vacancies and GdN segregation.

To discuss the N-rich GaN:Gd spectra, I adopt the same procedure as the N-rich GaN:Dy ones: the Ga-rich GaN:Gd and GdN spectra are mixed. The calculated GdN spectrum is obtained by using the lattice constant 4.998 Å [53].

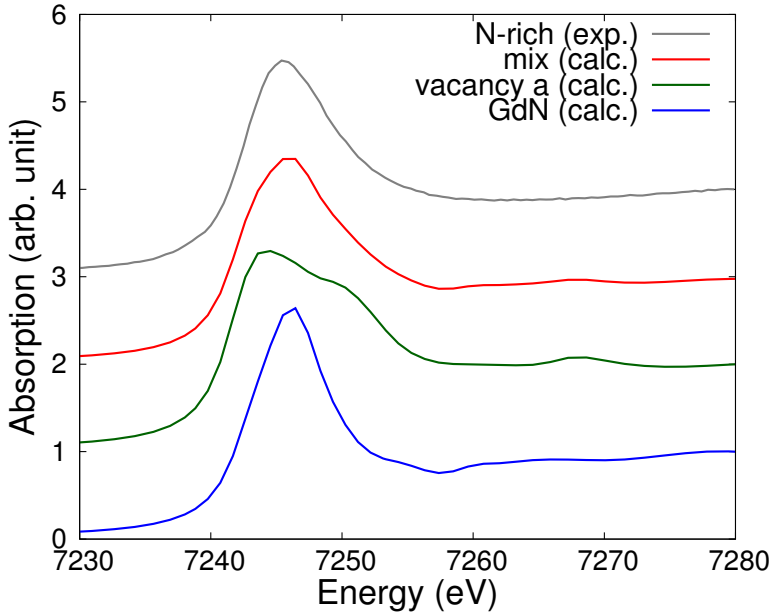

Figure 3.21: Mixed calculated Gd L_3-edge XANES spectra of the Ga-rich GaN:Gd and GdN. For comparison, the observed N-rich GaN:Gd spectrum and the calculated model(a) and GdN spectra are also shown.

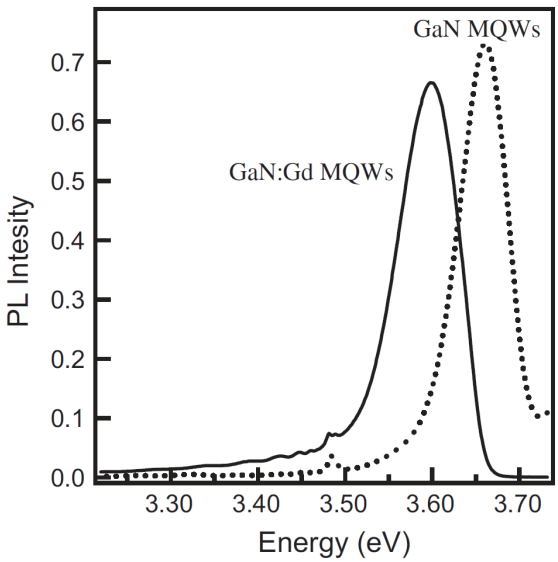

Figure 3.22: Observed PL spectra from the GaN/AlGaN (dotted line) and GaGdN/AlGaN MQWs (solid line) at 10 K. Reprinted from [77] with permission from Elsevier.

Figure 3.21 shows the mixed calculated Gd L_3-edge XANES spectra with the Ga-rich GaN:Gd and GdN. For comparison, the observed N-rich GaN:Gd and calculated Ga-rich GaN:Gd (model (a): V^a) and GdN spectra are also shown. In Fig. 3.21, the calculated mixed spectrum well agrees with the observed N-rich spectrum in the same way as the GaN:Dy case. I also estimate GdN segregation in GaN:Gd by using Table 3.4. The calculated amount of substance of GdN is almost 1.0 mol if the initial amount of substance of GaN:Gd 1.0 mol. Therefore, the same conclusion as GaN:Dy is obtained: the N-rich GdN sample has the solid solution and GdN phases.

Recently, photoluminescence (PL) spectra from the GaN(1 nm) / AlGaN and GaGdN(1 nm) / AlGaN multi-quantum wells (MQW) were compared [77]. The stoichiometry of AlGaN and GaGdN is $Al_{0.12}Ga_{0.88}N$ and $Ga_{0.88}Gd_{0.02}N$, respectively. Figure 3.22 shows PL spectra from those MQWs at 10 K. The GaN(1 nm) / AlGaN MQWs showed blue shift of the main peak (exciton peak) at 3.664 eV relative to the GaN template (3.483 eV) because of the quantum confinement effect of the 1 nm thick GaN layers. The GaGdN(1 nm) / AlGaN MQWs had the exciton peak at 3.598 eV: it also showed the blue shift relative to the GaN template, but red shift relative to the GaN(1 nm) / AlGaN MQWs. This red shift supports existence of the Gd-V_N complex because the blue shift is originated from interlayer compression, which may be released by V_N partially. Furthermore, temperature dependence of the exciton peak energy in the GaGdN / AlGaN MQWs was larger than that in the GaN / AlGaN ones. The red shifts of exciton peak from 50 to 300 K were 42 and 46 meV in the GaN/AlGaN and GaGdN / AlGaN MQWs, respectively. This temperature dependence is arisen from compressive effects by thermal expansion. The slightly larger red shift in GaGdN / AlGaN indicates that the Gd-V_N complex absorbs the a certain amount of the compression. The small relaxation (4 meV) of the compression in the GaGdN / AlGaN consistent with the small shift of the substituted Gd ion to V_N under no compressive condition. Combining this with the result of XANES analyses for GaN:RE, the existence of V^a are plausible.

3.5 Conclusion

I perform Gd L_3-edge XANES analyses, and Dy L_3- and L_1-edge polarization-dependent XANES measurements and calculations. The observed XANES spectra of GaN:RE are not sensitive to kinds of the RE elements. Large shift value of a RE ion is required to explain the N-rich spectra by only using the RE ion shift, which seems to be not feasible. A pre-edge peak of L_1-edge XANES spectra are more sensitive to local inversion symmetry around an absorbing atom than spectral shapes at L_3-edge, and can be used to detect it. Calculated spectra with only GaN:RE phase show good agreement with the observed Ga-rich ones. I find the anisotropy of a nitrogen vacancy next to a doped RE ion by using polarization-dependent spectra: N^a nitrogen sites are preferentially selected. For the reason of the weak polarization dependence of the N-rich sample, I propose RE nitride segregation: the mixture of Ga-rich and RE nitride spectra show good agreement with the observed N-rich spectra. XANES analyses at several edges with different X-ray polarization direction are useful to investigate vacancies around impurity atoms.

Chapter 4

SOI at scatterer sites for K-edge XMCD spectra

4.1 Introduction

The K-edge XMCD is a useful technique to obtain information about the local magnetic structure. We can obtain sensitive M-H curve without the diamagnetic term. In particular the transition metal, the energy at K-edge is located at hard X-ray region, which does not need vacuum conditions to measure X-ray absorption spectra. BCC iron and $Fe_{0.5}Co_{0.5}$ under extremly high pressures causes a phase transition to HCP structures and looses its ferromagnetism confirmed by K-edge XMCD spectra [78, 79, 80]. For other purposes, magnetic properties of light elements composing of magnetic materials are also investigated [81]. The magnetic moment on light elements relies on their p orbital. The X-ray absorption at K-edge has the information on unoccupied p state which is more or less related ground state ones.

There are several reports for light element XMCD spectra. The O K-edge XMCD spectra were reported for adsorbing oxygen atoms on thin film of transition meal on Cu substrate [82, 83, 84]. Nevertheless the smallness of the SOI of oxygen atoms, the XMCD spectra showed rather large intensity compared with well known BCC iron. Sorg et al. addressed that the hybridization between O $2p_z$ and TM $3d$ enhances the XMCD intensity [82, 83, 84]. From the sign of the XMCD signal, they concluded that the magnetic moment on O atoms is parallel to that on TM surface [83]. Band calculations

support the magnetic order with the strong orbital hybridization. Leuenberger et al. reported the N K-edge XMCD spectra for a bulk GdN crystal [60]. They mentioned that usual band theory could not reproduce the XMCD spectra. Other calculated results showed that the inclusion of the spin-orbit interaction on Gd atoms through the N $2p$-Gd ($4f$,$5d$) hybridizaton play crucial roles [85]. The C K-edge XMCD spectra were reported for graphene on TM substrate [86]. Similarly to the O K-edge case, the smallness of the spin-orbit interaction confuses us to interpret the XMCD spectra.

Several relativistic MS codes are implemented. The FEFF9 code [87] treats full relativistic core functions and semi-relativistic photoelectron states. The SPR-KKR code [88] is based on relativistic MS theory in reciprocal space. The FDMNES code [89] also include relativistic effect. However, there is no intensive work to investigate effects of SOI on each site as far as I know.

Here, I develop the MS theory including the spin-orbit interaction on scatterer atoms. I also study XMCD spectra of BCC iron as a simple system, and graphene/Ni(111) as a complicate system with the developed MS theory.

4.2 Theory

At first, I briefly introduce a K,L_1-edge XMCD theory based on MS described at Chap. 2. [24, 21]. In the XMCD theory, the relativistic effects on a photoelectron state is taken into account as a perturbation via an expansion of a relativistic Green's function with non-relativistic Green's function developed by Gesztesy *et al* [29]. The core-state wave function which emits a photoelectron is obtained by the Dirac equation, and fully includes relativistic effects.

Next, I describe how the spin-orbit interaction on scatterer sites is included. The previous method [21, 23, 24] considered the spin-orbit interaction only on the absorbing atom. This interpretation was conceived from a result of a single scattering calculation for BCC iron in MEXAFS energy region (100 eV $\sim$) [23]. However, the privious scatterer-site SOI terms have less site T-matrices than the absorbing-atom SOI term: the order of the site T-matrix is not same. Furthermore, in XMCD energy region, inclusion of MS is inevitable. I therefore take the SOI on scattering sites into account, and calculate its

effects carefully.

4.2.1 K, L_1-edge XMCD

For the K, L_1-edge, T_{11} defined in eq. (2.14a) does not contribute to XMCD intensity owing to no SOI, while the other terms T_{12}, T_{21}, U_{11} provide XMCD spectra.

$$T_{12}(\omega) = -2\mathrm{Im}\,\langle\varphi_c|\Delta^* g Q \Delta|\chi_c\rangle\,, \tag{2.14b}$$

$$T_{21}(\omega) = -2\mathrm{Im}\,\langle\chi_c|\Delta^* Q g \Delta|\varphi_c\rangle\,, \tag{2.14c}$$

$$U_{11}(\omega) = -2\mathrm{Im}\,\langle\varphi_c|\Delta^* g Q (V-\varepsilon) Q G \Delta|\varphi_c\rangle \tag{2.14d}$$

$$Q = \frac{\sigma\cdot\boldsymbol{p}}{2c} \tag{2.5}$$

I firstly focus on U_{11}. If we assume the total potential V is superposition of each spherical site potential, the operator $Q(V-\varepsilon)Q$ gives the SOI (see Appendix B). Then,

$$\begin{aligned} U_{11}(\omega) &= -2\mathrm{Im}\,\langle\varphi_c|\,\Delta^* g(\varepsilon) Q (V-\varepsilon) Q g(\varepsilon)\Delta\,|\varphi_c\rangle \\ &= -2\mathrm{Im}\sum_\alpha \langle\varphi_c|\,\Delta^* g(\varepsilon)\delta v_\alpha g(\varepsilon)\Delta\,|\varphi_c\rangle\,, \end{aligned} \tag{4.1}$$

where δv_α is the SOI on the site α. The propagator g can be represented by the site T-matrix expansion.

$$g = g_A + g_A \sum_{\alpha(\neq A)} t_\alpha g_A + g_A \sum_{\beta(\neq\alpha,A)} t_\beta g_0 \sum_{\alpha(\neq A)} t_\alpha g_A + \cdots \tag{4.2}$$

$$= g_A + g_B v_B g_A + g_B \sum_{\alpha(\neq A,B)} t_\alpha g_A + g_B \sum_{\beta(\neq\alpha,B)} t_\beta g_0 \sum_{\alpha(\neq A)} t_\alpha g_A + \cdots \tag{4.3}$$

$$= g_A + g_A v_B g_B + g_A \sum_{\alpha(\neq A,B)} t_\alpha g_B + g_A \sum_{\beta(\neq\alpha,A)} t_\beta g_0 \sum_{\alpha(\neq B)} t_\alpha g_B + \cdots\,. \tag{4.4}$$

The extra term $g_B v_B g_A$ only appears when $A \neq B$. In both the expansion, we can write g as $g_A + (g - g_A)$. Then, U_{11} becomes:

$$U_{11} = -2\mathrm{Im}\sum_\alpha \langle\varphi_c|\,\Delta^*\{g_A + (g-g_A)\}\delta v_\alpha\{g_A + (g-g_A)\}\Delta\,|\varphi_c\rangle \tag{4.5}$$

$$= -2\mathrm{Im}\sum_\alpha (\langle\varphi_c|\,\Delta^* g_A \delta v_\alpha g_A \Delta\,|\varphi_c\rangle + \langle\varphi_c|\,\Delta^*(g-g_A)\delta v_\alpha g_A\Delta\,|\varphi_c\rangle \tag{4.6}$$

$$+ \langle\varphi_c|\,\Delta^* g_A \delta v_\alpha (g-g_A)\Delta\,|\varphi_c\rangle + \langle\varphi_c|\,\Delta^*(g-g_A)\delta v_\alpha(g-g_A)\Delta\,|\varphi_c\rangle) \tag{4.7}$$

Furthermore, I separate U_{11} into $U_{11,A}$ and $U_{11,sc}$ in terms of δv.

$$\begin{aligned} U_{11} = &-2\mathrm{Im}\big[\langle\varphi_c|\,\Delta^* g_A \delta v_A g_A \Delta\,|\varphi_c\rangle + 2\,\langle\varphi_c|\,\Delta^*(g-g_A)\delta v_A g_A\Delta\,|\varphi_c\rangle\big] \\ &- 2\mathrm{Im}\sum_{B(\neq A)}\big[\langle\varphi_c|\,\Delta^* g_A\delta v_B g_A\Delta\,|\varphi_c\rangle \\ &\quad + \langle\varphi_c|\,\Delta^*(g-g_A)\delta v_B g_A\Delta\,|\varphi_c\rangle + \langle\varphi_c|\,\Delta^* g_A\delta v_B(g-g_A)\Delta\,|\varphi_c\rangle\big] \\ &- 2\mathrm{Im}\sum_{\alpha}\langle\varphi_c|\,\Delta^*(g-g_A)\delta v_\alpha(g-g_A)\Delta\,|\varphi_c\rangle \qquad (4.8) \\ \equiv\ & U_{11,A} + U_{11,sc} \qquad (4.9) \end{aligned}$$

where

$$\begin{aligned} U_{11,A} &= -2\mathrm{Im}[\langle\varphi_c|\,\Delta^* g_A\delta v_A g_A\Delta\,|\varphi_c\rangle + 2\,\langle\varphi_c|\,\Delta^*(g-g_A)\delta v_A g_A\Delta\,|\varphi_c\rangle] \qquad (4.10) \\ &\equiv U_{11,A}^{(0)} + U_{11,A}^{(\infty)}, \qquad (4.11) \\ U_{11,sc} &= -2\mathrm{Im}\sum_{B(\neq A)}\big[\langle\varphi_c|\,\Delta^* g_A\delta v_B g_A\Delta\,|\varphi_c\rangle \\ &\quad + \langle\varphi_c|\,\Delta^*(g-g_A)\delta v_B g_A\Delta\,|\varphi_c\rangle + \langle\varphi_c|\,\Delta^* g_A\delta v_B(g-g_A)\Delta\,|\varphi_c\rangle\big] \\ &\quad - 2\mathrm{Im}\sum_{\alpha}\langle\varphi_c|\,\Delta^*(g-g_A)\delta v_\alpha(g-g_A)\Delta\,|\varphi_c\rangle\,. \qquad (4.12) \end{aligned}$$

In the case of $(g-g_A)\delta v_A g_A$, the order inversion term has the same value. On the other hand, that is not always guaranteed for $(g-g_A)\delta v_B g_A$. In the previous theory [23, 21, 24], $U_{11,A}$ was only taken into account. I discuss the neglected term $U_{11,sc}$ in the next section. To obtain the explicit form of $U_{11,A}$, the expansion of eq. (4.2) is adequate.

$U_{11,A}$

When photoelectron positions $\mathbf{r}$ and $\mathbf{r}'$ in site A ($\mathbf{r},\mathbf{r}' \in A$), g_A is written by

$$g_A(\mathbf{r},\mathbf{r}';k) = \sum_L g_A^l(r,r';k) Y_L(\hat{\mathbf{r}}) Y_L^*(\hat{\mathbf{r}}'), \qquad (4.13)$$

$$g_A^{l\pm}(r,r';k^\pm) = -2ik^\pm R_l^\pm(k^\pm r_<)\hat{f}_l^\pm(k^\pm r_>) \qquad (4.14)$$

$$(r_< = min(r,r'),\ r_> = max(r,r')).$$

The regular (irregular) solution R_l ($\hat{f}_l$) has asymptotic form ($r\to\infty$):

$$R_l(kr) \approx e^{i\delta_l}\sin(kr - l\pi/2 + \delta_l)/kr, \qquad (4.15)$$

$$\hat{f}_l(kr) \approx i^{-l-1}\exp(ikr)/kr. \qquad (4.16)$$

The large component of the 1s core state is obtained by eqs. (2.9) and (2.11):

$$|\varphi_c^{\pm}\rangle = g_{j_c}(r) y^{l_c}_{j_c,\mu_c}(\hat{\mathbf{r}})\,|\pm\rangle = g_{1s}(r) y^0_{1/2,\pm 1/2}(\hat{\mathbf{r}})\,|\pm\rangle = g_{1s}(r) Y_{00}\,|\pm\rangle\,. \tag{4.17}$$

The atomic absorption term $U^{(0)}_{11}$ is written by

$$U^{(0)}_{11,A}(m_p) = -2\mathrm{Im}\,\langle\varphi_c|\,\Delta^*_{m_p} g_A \delta v_A g_A \Delta_{m_p}\,|\varphi_c\rangle = \frac{2m_p}{\pi}\sum_s s\mathrm{Im}k^{s2}\delta\rho^s_0, \tag{4.18}$$

$$\begin{aligned}\delta\rho^{\pm}_0 = &\int g_{1s}(r) r^3 dr \int R^{\pm}_{A,1}(r_<) f^{\pm}_{A,1}(r_>)\xi^{\pm}_A(r') r'^2 dr' \\ &\times \int R^{\pm}_{A,1}(r'_<) f^{\pm}_{A,1}(r'_>) g_{1s}(r'') r''^3 dr''.\end{aligned} \tag{4.19}$$

Therefore, The atomic XMCD intensity $\Delta U^{(0)}_{11,A}$ is written by

$$\begin{aligned}\Delta U^{(0)}_{11,A}(\omega) &= U^{(0)}_{11,A}(\omega,+) - U^{(0)}_{11,A}(\omega,-) \\ &= \frac{4}{\pi}\mathrm{Im}[k^{+2}\delta\rho^+_0(\varepsilon) - (+spin \to -spin)].\end{aligned} \tag{4.20}$$

The SOI ζ mixes spin and orbital state, and provide difference of the absorption with $\pm$helicity. The single scattering term $U^{(1)}_{11,A}$ is written by

$$\begin{aligned}U^{(1)}_{11,A}(m_p) &= -4\mathrm{Im}\sum_{\alpha(\neq A)}\langle\varphi_c|\,\Delta^*_{m_p} g_A t_\alpha g_A \delta v_A g_A \Delta_{m_p}\,|\varphi_c\rangle \\ &= -\frac{2m_p}{\pi}\sum_s s\mathrm{Im}\rho^s_{>,1}\hat{G}^{(1)s}_{1m_p,1m_p}\delta\rho^s,\end{aligned} \tag{4.21}$$

$$\delta\rho^{\pm} = \int R^{\pm}_{A,1}(r)\xi^{\pm}_A(r) r^2 dr \int R^{\pm}_{A,1}(r_<)\hat{f}^{\pm}_{A,1}(r_>) g_{1s}(r') r'^3 dr' \tag{4.22}$$

The single scattering XMCD $\Delta U^{(1)}_{11,A}$ becomes:

$$\Delta U^{(1)}_{11,A}(\omega) = U^{(1)}_{11,A}(\omega,+) - U^{(1)}_{11,A}(\omega,-) \tag{4.23}$$

$$= -\frac{4}{\pi}\mathrm{Im}\left[\rho^+_{>,1}(\varepsilon)\delta\rho^+(\varepsilon)\hat{G}^{(1)+}_{11,11}(\varepsilon) - (+spin \to -spin)\right] \tag{4.24}$$

The infinite scattering XMCD $\Delta U^{(\infty)}_{11,A}$ is obtained by the replacement of $\hat{G}$ to Z described.

$$\Delta U^{(\infty)}_{11,A}(\omega) = -\frac{4}{\pi}\mathrm{Im}\left[\rho^+_{>,1}(\varepsilon)\delta\rho^+(\varepsilon) Z^+_{11,11}(\varepsilon) - (+spin \to -spin)\right] \tag{4.25}$$

From these results, I drive $\Delta U_{11,A}$.

$$\Delta U_{11,A}(\omega) = \Delta U^{(0)}_{11,A}(\omega) + \Delta U^{(\infty)}_{11,A}(\omega) \tag{4.26}$$

$$= \frac{4}{\pi}\mathrm{Im}\left[\left(k^{+2}\delta\rho^+_0(\varepsilon) - \rho^+_{>,1}(\varepsilon)\delta\rho^+(\varepsilon) Z^+_{11,11}(\varepsilon)\right) - (+spin \to -spin)\right] \tag{4.27}$$

T_{12} and T_{21}

The intensity T_{12} and T_{21} are the same value, so I discuss only the former. From eqs. (2.10) and (B.20), T_{12} in eq. (2.14b) are represented by using the orbital moment operator $\mathbf{L}$.

$$\begin{aligned} T_{12}(m_p) &= -2\mathrm{Im}\left\langle\varphi_c\right| \Delta^* g Q \Delta \left|\chi_c\right\rangle \qquad (2.14b)\\ &= -2\mathrm{Im}\sum_s \int g_{1s}(r) Y_{00} r Y^*_{1m_p}(\hat{\mathbf{r}}) d\mathbf{r} \\ &\quad \times \int g^s(\mathbf{r},\mathbf{r}') Q(\sigma\cdot\mathbf{r}') r' Y_{1m_p}(\hat{\mathbf{r}}') i f_{1s}(r') Y_{00} d\mathbf{r}' \\ &\sim \frac{1}{c}\mathrm{Im}\sum_s \int g_{1s}(r) Y_{00} r Y^*_{1m_p}(\hat{\mathbf{r}}) d\mathbf{r} \\ &\quad \times \int g^s(\mathbf{r},\mathbf{r}')(\sigma\cdot\mathbf{L}') r' Y_{1m_p}(\hat{\mathbf{r}}') f_{1s}(r') Y_{00} d\mathbf{r}' \qquad (4.28) \end{aligned}$$

Similarly to $U_{11,A}$, I separate T_{12} to the atomic term $T_{12}^{(0)}$ and the scattering term $T_{12}^{(\infty)}$.

$$\begin{aligned} T_{12}^{(0)}(m_p) &= -2\mathrm{Im}\left\langle\varphi_c\right| \Delta^* g_A Q \Delta \left|\chi_c\right\rangle \qquad (4.29)\\ &\sim \frac{m_p}{2\pi c}\sum_s s\mathrm{Im}\left[ik\int g_{1s}(r) r^3 dr \int R^s_{A,1}(r_<)\hat{f}^s_{A,1}(r_>) f_{1s}(r') r'^3 dr'\right] \\ &= \frac{m_p}{2\pi c}\sum_s s\mathrm{Im}\left[ik\rho^s_{><,1}\right], \qquad (4.30) \end{aligned}$$

$$\begin{aligned} \Delta T_{12}^{(0)}(\omega) &= T_{12}^{(0)}(\omega,+) - T_{12}^{(0)}(\omega,-) \qquad (4.31)\\ &= \frac{1}{\pi c}\mathrm{Im}\left[ik\rho^+_{><,1}(\varepsilon) - (+spin\to -spin)\right], \qquad (4.32)\\ \rho^\pm_{><,1} &= \int g_{1s}(r) r^3 dr \int R^\pm_{A,1}(r_<)\hat{f}^\pm_{A,1}(r_>) f_{1s}(r') r'^2 dr'. \qquad (4.33) \end{aligned}$$

The scattering terms $T_{12}^{(1)}(m_p)$ and $T_{12}^{(\infty)}(m_p)$ become:

$$\begin{aligned} T_{12}^{(1)}(m_p) &= -2\mathrm{Im}\sum_\alpha \left\langle\varphi_c\right| \Delta^* g_A t_\alpha g_A Q \Delta \left|\chi_c\right\rangle \qquad (4.34)\\ &= -\frac{m_p}{2\pi c}\sum_s s\mathrm{Im}\rho^s_{>,1}\hat{G}^{(1)s}_{1m_p,1m_p}\rho^s_{<,1}, \qquad (4.35)\\ T_{12}^{(\infty)}(m_p) &= -\frac{m_p}{2\pi c}\sum_s s\mathrm{Im}\rho^s_{>,1} Z^s_{1m_p,1m_p}\rho^s_{<,1}, \qquad (4.36) \end{aligned}$$

$$\begin{aligned} \Delta T_{12}^{(\infty)}(\omega) &= T_{12}^{(\infty)}(\omega,+) - T_{12}^{(\infty)}(\omega,-) \qquad (4.37)\\ &= -\frac{1}{\pi c}\mathrm{Im}\left[\rho^+_{>,1}(\varepsilon)\rho^+_{<,1}(\varepsilon) Z^+_{11,11}(\varepsilon) - (+spin\to -spin)\right], \qquad (4.38)\\ \rho^\pm_{<,1} &= \int R^\pm_{A,1}(r) f_{1s}(r) r^2 dr. \qquad (4.39) \end{aligned}$$

We obtain the XMCD intensity ΔT_{12}.

$$\Delta T_{12}(\omega) = \Delta T_{12}^{(0)}(\omega) + \Delta T_{12}^{(\infty)}(\omega) \tag{4.40}$$

$$= \frac{1}{\pi c}\mathrm{Im}\left[\left(ik\rho^{+}_{><,1}(\varepsilon) - \rho^{+}_{>,1}(\varepsilon)\rho^{+}_{<,1}(\varepsilon)Z^{+}_{11,11}(\varepsilon)\right) - (+spin \to -spin)\right] \tag{4.41}$$

4.2.2 Including spin-orbit interaction on scatterer sites

Here, I discuss the scattering term $U_{11,sc}$ in (4.12) constituted by the five ingredients.

$$\begin{aligned} U_{11,sc} = -2\mathrm{Im}\sum_{B(\neq A)} \big[&\langle\varphi_c|\,\Delta^* g_A \delta v_B g_A \Delta\,|\varphi_c\rangle \\ &+ \langle\varphi_c|\,\Delta^*(g-g_A)\delta v_B g_A \Delta\,|\varphi_c\rangle + \langle\varphi_c|\,\Delta^* g_A \delta v_B (g-g_A)\Delta\,|\varphi_c\rangle\big] \\ &- 2\mathrm{Im}\sum_{\alpha}\langle\varphi_c|\,\Delta^*(g-g_A)\delta v_\alpha (g-g_A)\Delta\,|\varphi_c\rangle\,. \end{aligned} \tag{4.12}$$

I firstly summarize partial wave expansions of propagators. The position vector $\mathbf{r}$ is inside an atomic site, while $\mathbf{R}$ describes position of an atomic site.

$$g_0(\mathbf{r}+\mathbf{R}_\beta, \mathbf{r}'+\mathbf{R}_\alpha) = g_0(\mathbf{r}+\mathbf{R}_{\beta\alpha}, \mathbf{r}') \tag{4.42}$$

$$= 2\sum_{LL'} i^{l-l'} G_{LL'}(k\mathbf{R}_{\beta\alpha}) j_l(kr) Y_L(\hat{\mathbf{r}}) j_{l'}(kr') Y_{L'}(\hat{\mathbf{r}}') \tag{4.43}$$

$$= 2\sum_{LL'} i^{l-l'} G_{LL'}(k\mathbf{R}_{\alpha\beta}) j_l(kr) Y_L(-\hat{\mathbf{r}}) j_{l'}(kr') Y_{L'}(-\hat{\mathbf{r}}') \tag{4.44}$$

$$= g_0(\mathbf{r}', \mathbf{r}+\mathbf{R}_{\beta\alpha}), \tag{4.45}$$

$$g_A(\mathbf{r}+\mathbf{R}_\beta, \mathbf{r}'+\mathbf{R}_A) = 2\sum_{LL'} i^{l-l'} e^{i\delta^A_{l'}} G_{LL'}(k\mathbf{R}_{\beta A}) j_l(kr) Y_L(\hat{\mathbf{r}}) \tilde{R}_{A,l'}(kr') Y_{L'}(\hat{\mathbf{r}}') \tag{4.46}$$

$$= g_A(\mathbf{r}'+\mathbf{R}_A, \mathbf{r}+\mathbf{R}_\beta), \tag{4.47}$$

$$g_A(\mathbf{r},\mathbf{r}')\,(\mathbf{r},\mathbf{r}'\in A) = -2ik\sum_{L} e^{i\delta^A_l} \tilde{R}_{A,l}(kr_<) \hat{f}_{A,l}(kr_>) Y_L(\hat{\mathbf{r}}) Y_L(\hat{\mathbf{r}}'), \tag{4.48}$$

where

$$G_{LL'}(k\mathbf{R}) = -4\pi ik \sum_{L''} i^{l''} h^{(1)}_{l''}(kR) Y_{L''}(\hat{\mathbf{R}}) G(L''L|L'), \tag{4.49}$$

$$G_{LL'}(-k\mathbf{R}) = (-1)^{l+l'} G_{LL'}(k\mathbf{R}), \tag{4.50}$$

$$G_{\bar{L}\bar{L}'}(k\mathbf{R}) = (-1)^{m+m'} G_{L'L}(k\mathbf{R}). \tag{4.51}$$

The scatterer site term $U_{11,sc}$ is obtained from eq. (4.12).

$$\begin{aligned} U_{11,sc} = -2\mathrm{Im} \sum_{B(\neq A)} & [\langle\varphi_c| \Delta^* g_A \delta v_B g_A \Delta |\varphi_c\rangle \\ & + \langle\varphi_c| \Delta^* (g - g_A) \delta v_B g_A \Delta |\varphi_c\rangle + \langle\varphi_c| \Delta^* (g - g_A) \delta v_B g_A \Delta |\varphi_c\rangle] \\ & - 2\mathrm{Im} \sum_{\alpha} \langle\varphi_c| \Delta^* (g - g_A) \delta v_\alpha (g - g_A) \Delta |\varphi_c\rangle \,. \end{aligned} \tag{4.12}$$

By using eq. (4.4), the second ingredient is classified to the single scattering at B site, and the semi infinite scattering.

$$\begin{aligned} & \langle\varphi_c| \Delta^* (g - g_A) \delta v_B g_A \Delta |\varphi_c\rangle \\ & = \langle\varphi_c| \Delta^* g_A v_B g_B \delta v_B g_A \Delta |\varphi_c\rangle \\ & \quad + \langle\varphi_c| \Delta^* g_A \left(\sum_{\alpha(\neq A,B)} t_\alpha + \sum_{\beta(\neq\alpha,A)} t_\beta g_0 \sum_{\alpha(\neq B)} t_\alpha + \cdots \right) g_B \delta v_B g_A \Delta |\varphi_c\rangle \end{aligned} \tag{4.52}$$

Similarly, the third ingredient in eq. (4.12) is separated to three components by using the expansions of eqs. (4.3) and (4.4).

$$\begin{aligned} & \langle\varphi_c| \Delta^* (g - g_A) \delta v_\alpha (g - g_A) \Delta |\varphi_c\rangle \\ & = (1 - \delta_{A\alpha}) \Bigg[\langle\varphi_c| \Delta^* g_A v_\alpha g_\alpha \delta v_\alpha g_\alpha v_\alpha g_A \Delta |\varphi_c\rangle \\ & \quad + \langle\varphi_c| \Delta^* g_A \left(\sum_{\beta(\neq A,\alpha)} t_\beta + \sum_{\gamma(\neq\beta,A)} t_\gamma g_0 \sum_{\beta(\neq\alpha)} t_\beta + \cdots \right) g_\alpha \delta v_\alpha g_\alpha v_\alpha g_A \Delta |\varphi_c\rangle \\ & \quad + \langle\varphi_c| \Delta^* g_A v_\alpha g_\alpha \delta v_\alpha g_\alpha \left(\sum_{\beta(\neq A,\alpha)} t_\beta + \sum_{\gamma(\neq\beta,\alpha)} t_\gamma g_0 \sum_{\beta(\neq A)} t_\beta + \cdots \right) g_A \Delta |\varphi_c\rangle \Bigg] \\ & \quad + \langle\varphi_c| \Delta^* g_A \left(\sum_{\beta(\neq A,\alpha)} t_\beta + \sum_{\gamma(\neq\beta,A)} t_\gamma g_0 \sum_{\beta(\neq\alpha)} t_\beta + \cdots \right) \\ & \qquad \times g_\alpha \delta v_\alpha g_\alpha \left(\sum_{\beta'(\neq A,\alpha)} t_\beta + \sum_{\gamma'(\neq\beta',\alpha)} t_\gamma g_0 \sum_{\beta'(\neq A)} t_\beta + \cdots \right) g_A \Delta |\varphi_c\rangle \end{aligned} \tag{4.53}$$

We divide $U_{11,sc}$ into $U^{GG}_{11,sc}$, $U^{Z'G}_{11,sc}$ and $U^{Z'Z'}_{11,sc}$ in terms of photoelectron scattering processes.

$$U^{GG}_{11,sc} = -2\mathrm{Im}\sum_{B(\neq A)}\left[\langle\varphi_c|\,\Delta^* g_A \delta v_B g_A \Delta\,|\varphi_c\rangle\right.$$
$$\left.+2\,\langle\varphi_c|\,\Delta^* g_A v_B g_B \delta v_B g_A \Delta\,|\varphi_c\rangle + \langle\varphi_c|\,\Delta^* g_A v_B g_B \delta v_B g_B v_B g_A \Delta\,|\varphi_c\rangle\right], \tag{4.54}$$

$$U^{Z'G}_{11,sc} = -2\mathrm{Im}\sum_{B(\neq A)}\left[\langle\varphi_c|\,\Delta^* g_A \left(\sum_{\alpha(\neq A,B)} t_\alpha + \cdots\right) g_B \delta v_B \left(g_A + g_B v_B g_A\right)\Delta\,|\varphi_c\rangle\right.$$
$$\left.\times\,\langle\varphi_c|\,\Delta^*\left(g_A + g_A v_B g_B\right)\delta v_B g_B \left(\sum_{\alpha(\neq A,B)} t_\alpha + \cdots\right) g_A \Delta\,|\varphi_c\rangle\right] \tag{4.55}$$

$$U^{Z'Z'}_{11,sc} = -2\mathrm{Im}\sum_{\alpha}\langle\varphi_c|\,\Delta^* g_A \left(\sum_{\beta(\neq A,\alpha)} t_\beta + \cdots\right)$$
$$\times\, g_\alpha \delta v_\alpha g_\alpha \left(\sum_{\beta'(\neq A,\alpha)} t_{\beta'} + \cdots\right) g_A \Delta\,|\varphi_c\rangle\,. \tag{4.56}$$

$U^{GG}_{11,sc}$

- $\langle\varphi_c|\,\Delta^* g_A \delta v_B g_A \Delta\,|\varphi_c\rangle$

From $\langle\varphi^s|\varphi^{\bar{s}}\rangle = 0$ ($s = \pm$, $\bar{s} = -s$) and eq.(B.16), only diagonal terms survive in spin space.

$$\begin{aligned}
&\langle\varphi_c|\,\Delta^* g_A \delta v_B g_A \Delta\,|\varphi_c\rangle \\
&\quad= \langle\varphi_c^+|\,\Delta^* g_A^+ \xi_B^+ L_z^B g_A^+ \Delta\,|\varphi_c^+\rangle + \langle\varphi_c^+|\,\Delta^* g_A^+ \xi_B^+ L_-^B g_A^- \Delta\,|\varphi_c^-\rangle \\
&\qquad\quad + \langle\varphi_c^-|\,\Delta^* g_A^- \xi_B^- L_+^B g_A^+ \Delta\,|\varphi_c^+\rangle - \langle\varphi_c^-|\,\Delta^* g_A^- \xi_B^- L_z^B g_A^- \Delta\,|\varphi_c^-\rangle \\
&\quad= \langle\varphi_c^+|\,\Delta^* g_A^+ \xi_B^+ L_z^B g_A^+ \Delta\,|\varphi_c^+\rangle - \langle\varphi_c^-|\,\Delta^* g_A^- \xi_B^- L_z^B g_A^- \Delta\,|\varphi_c^-\rangle \qquad (4.57) \\
&\quad= \sum_s s\,\langle\varphi_c^s|\,\Delta^* g_A^s \xi_B^s L_z^B g_A^s \Delta\,|\varphi_c^s\rangle\,. \qquad (4.58)
\end{aligned}$$

Since site potentials are assumed as diagonal in spin space, propagators conserve spin states. The other terms also satisfy this spin diagonal. By using abbreviation $G_{LL'}(k\mathbf{R}_{\alpha\beta}) \equiv$

$G^{\alpha\beta}_{LL'}$, the explicit form is obtained.

$$
\begin{aligned}
&\langle\varphi_c|\,\Delta^* g_A \delta v_B g_A \Delta\,|\varphi_c\rangle \\
&\quad= \sum_s s \int g_{1s}(r) Y_{00} r Y^*_{1m_p}(\hat{\mathbf{r}}) 2 \sum_{L_1 L_1'} i^{l_1 - l_1'} G^{AB}_{L_1 L_1'} e^{i\delta^A_{l_1}} \tilde{R}^A_{l_1}(kr) Y_{L_1}(\hat{\mathbf{r}}) d\mathbf{r} \\
&\qquad\times \int j_{l_1'}(kr') Y^*_{L_1'}(\hat{\mathbf{r}}') \xi^s_B(r') L^B_z 2 \sum_{L_2 L_2'} i^{l_2 - l_2'} G^{BA}_{L_2 L_2'} j_{l_2}(kr') Y_{L_2}(\hat{\mathbf{r}}') d\mathbf{r}' \\
&\qquad\times \int e^{i\delta^A_{l_2'}} \tilde{R}^A_{l_2'}(kr'') Y^*_{L_2'}(\hat{\mathbf{r}''}) r'' Y_{1m_p}(\hat{\mathbf{r}''}) g_{1s}(r'') Y_{00} d\mathbf{r}'' \\
&\quad= 4Y_{00}^2 \sum_s s \sum_{L_1 L_1'} \sum_{L_2 L_2'} i^{l_1 - l_1' + l_2 - l_2'} e^{i(\delta^A_{l_1} + \delta^A_{l_2'})} \\
&\qquad\times \int g_{1s}(r) r \tilde{R}^A_{l_1}(kr) r^2 dr \int Y^*_{1m_p}(\hat{\mathbf{r}}) Y_{L_1}(\hat{\mathbf{r}}) d\hat{\mathbf{r}} \\
&\qquad\times m_2 G^{AB}_{L_1 L_1'} \left(\int j_{l_1'}(kr') \xi^s_B(r') j_{l_2}(kr') r'^2 dr' \int Y^*_{L_1'}(\hat{\mathbf{r}}') Y_{L_2}(\hat{\mathbf{r}}') d\hat{\mathbf{r}}' \right) G^{BA}_{L_2 L_2'} \\
&\qquad\times \int \tilde{R}^A_{l_1}(kr'') r'' g_{1s}(r'') r''^2 dr'' \int Y_{L_1}(\hat{\mathbf{r}''}) Y_{1m_p}(\hat{\mathbf{r}''}) d\hat{\mathbf{r}''} \\
&\quad= \frac{1}{\pi} \sum_s s {\rho_{>,1}}^2 \sum_L m G^{AB}_{1m_p,L} [\xi^s_B]^{jj}_l G^{BA}_{L,1m_p},
\end{aligned}
\tag{4.59}
$$

where

$$
[\xi^s_B]^{\phi_1\phi_2}_l = \int \phi_{1,l}(kr) \xi^s_B(r) \phi_{2,l}(kr) r^2 dr. \tag{4.60}
$$

- $\langle\varphi_c|\,\Delta^* g_A v_B g_B \delta v_B g_A \Delta\,|\varphi_c\rangle$

The major difference of $g_A v_B g_B \delta v_B g_A$ from $g_A \delta v_B g_A$ is that g_B propagates only in B site by the expression of eq.(4.48).

$$
\begin{aligned}
&\langle\varphi_c|\,\Delta^* g_A v_B g_B \delta v_B g_A \Delta\,|\varphi_c\rangle \\
&\quad= \sum_s \int d\mathbf{r} d\mathbf{r}' d\mathbf{r}'' d\mathbf{r}''' g_{1s}(r) Y_{00} r Y^*_{1m_p}(\hat{\mathbf{r}}) \\
&\qquad\times 2 \sum_{L_1 L_1'} i^{l_1 - l_1'} G^{AB}_{L_1 L_1'} R^s_{A,l_1}(kr) Y_{L_1}(\hat{\mathbf{r}}) j_{l_1'}(kr') Y^*_{L_1'}(\hat{\mathbf{r}}') \\
&\qquad\times v_B(r')(-2ik) \sum_L R^s_{B,l}(kr_<) \hat{f}^s_{B,l}(kr_>) Y_L(\hat{\mathbf{r}}') Y^*_L(\hat{\mathbf{r}''}) \\
&\qquad\times s \xi^s_B(r'') L^B_z \; 2 \sum_{L_2 L_2'} i^{l_2 - l_2'} G^{BA}_{L_2 L_2'} j_{l_2}(kr'') Y_{L_2}(\hat{\mathbf{r}''}) R^s_{A,l_2'}(kr''') Y^*_{L_2'}(\hat{\mathbf{r}'''}) \\
&\qquad\times r''' Y_{1m_p}(\hat{\mathbf{r}'''}) g_{1s}(r''') Y_{00}
\end{aligned}
$$

$$
\begin{aligned}
&= 4Y_{00}^2 \sum_s s \sum_{L_1 L_1'} \sum_{L_2 L_2'} \sum_L i^{l_1 - l_1' + l_2 - l_2'} \\
&\quad \times \int g_{1s}(r) r \tilde{R}_{l_1}^A(kr) r^2 dr \int Y_{1m_p}^*(\hat{\mathbf{r}}) Y_{L_1}(\hat{\mathbf{r}}) d\hat{\mathbf{r}}\ m_2 G_{L_1 L_1'}^{AB} \\
&\quad \times \left(\int j_{l_1'}(kr') v_B(r') (-2ik) R_{B,l}^s(kr_<) \hat{f}_{B,l}^s(kr_>) \xi_B^s(r'') j_{l_2}(kr'') r'^2 r''^2 dr' dr'' \right) \\
&\quad \times G_{L_2 L_2'}^{BA} \int Y_{L_1'}^*(\hat{\mathbf{r}}') Y_L(\hat{\mathbf{r}}') d\hat{\mathbf{r}}' \int Y_L^*(\hat{\mathbf{r}}'') Y_{L_2}(\hat{\mathbf{r}}'') d\hat{\mathbf{r}}'' \\
&\quad \times \int R_{A,l_2'}^s(kr''') r''' g_{1s}(r''') r'''^2 dr''' \int Y_{L_2'}(\hat{\mathbf{r}}''') Y_{1m_p}(\hat{\mathbf{r}}''') d\hat{\mathbf{r}}''' \\
&= \frac{1}{\pi} \sum_s s {\rho_{>,1}}^2 \sum_L m G_{1m_p,L}^{AB} \left(-2ik [(v\xi)_B^s]_l^{jj} \right) G_{L,1m_p}^{BA}, \qquad (4.61) \\
&= \langle \varphi_c | \, \Delta^* g_A \delta v_B g_B v_B g_A \Delta \, | \varphi_c \rangle \qquad (4.62)
\end{aligned}
$$

where

$$
[(v\xi)_B^s]_l^{\phi_1 \phi_2} = \int \phi_{1,l}(kr) v_B(r) R_{B,l}^s(kr_<) \hat{f}_{B,l}^s(kr_>) \xi_B^s(r') \phi_{2,l}(kr') r^2 r'^2 dr dr' \qquad (4.63)
$$

- $\langle \varphi_c | \, \Delta^* g_A v_B g_B \delta v_B g_B v_B g_A \Delta \, | \varphi_c \rangle$

Similar expansion from $g_A \delta v_B g_A$ to $g_A v_B g_B \delta v_B g_A$, we obtain the last term of $U_{11,sc}^{GG}$ in eq. (4.55).

$$
\begin{aligned}
&\langle \varphi_c | \, \Delta^* g_A v_B g_B \delta v_B g_B v_B g_A \Delta \, | \varphi_c \rangle \\
&\quad = \frac{1}{\pi} \sum_s s {\rho_{>,1}}^2 \sum_L m G_{1m_p,L}^{AB} \left(-4k^2 [(v\xi v)_B^s]_l^{jj} \right) G_{L,1m_p}^{BA} \qquad (4.64)
\end{aligned}
$$

where

$$
\begin{aligned}
[(v\xi v)_B^s]_l^{jj} = &\int j_l(kr) v_B(r) r^2 dr \int R_{B,l}^s(kr_<) \hat{f}_{B,l}^s(kr_>) \xi_B^s(r') r'^2 dr' \\
&\times \int R_{B,l}^s(kr'_<) \hat{f}_{B,l}^s(kr'_>) v_B^s(r'') j_l(kr'') r''^2 dr''. \qquad (4.65)
\end{aligned}
$$

Therefore, the single scattering term $U_{11,sc}^{GG}$ becomes:

$$
\begin{aligned}
U_{11,sc}^{GG}(m_p) = &-\frac{2}{\pi} \mathrm{Im} \sum_s s {\rho_{>,1}}^2 \sum_{B(\neq A)} \sum_{l>0} \left\{ [\xi_B^s]_l^{jj} - 4ik [(v\xi)_B^s]_l^{jj} - 4k^2 [(v\xi v)_B^s]_l^{jj} \right\} \\
&\times \sum_{m(\neq 0)} m G_{1m_p,L}^{AB} G_{L,1m_p}^{BA}. \qquad (4.66)
\end{aligned}
$$

$U^{Z'G}_{11,sc}$

- $\langle\varphi_c|\,\Delta^* g_A \left(\sum_{\alpha(\neq A,B)} t_\alpha + \sum_{\beta(\neq\alpha,A)} t_\beta g_0 \sum_{\alpha(\neq B)} t_\alpha + \cdots\right) g_B \delta v_B g_A \Delta\,|\varphi_c\rangle$

We firstly consider the first order of t. Comparison with $g_A\delta v_B g_A$, the photoelectron migration from B to A via α is added. This change corresponds to $G^{AB} \to G^{(1)AB}$. Notice that g_B in $g_A t_\alpha g_B \delta v_B g_A$ propargates between different sites α and B by the expression of eq. (4.46).

$$\langle\varphi_c|\,\Delta^* g_A \sum_{\alpha(\neq)A,B} t_\alpha g_B \delta v_B g_A \Delta\,|\varphi_c\rangle = \frac{1}{\pi}\sum_s s\rho_{>,1}{}^2 \sum_L m \hat{G}^{(1)AB}_{1m_p,L}[\xi^s_B]^{Rj}_l G^{BA}_{L,1m_p}. \tag{4.67}$$

To expand this term to the infinite scattering, we replace $G^{(1)}$ to Z'.

$$\hat{G}^{AB(1)}_{L_1,L_2} \to Z'^{AB}_{L_1,L_2} = t^A_{l_1}(k)^{-1}\left[(1-X)^{-1}-1\right]^{AB}_{L_1L_2} - G^{AB}_{L_1L_2} = \hat{G}^{AB(1)}_{L_1L_2} + \hat{G}^{AB(2)}_{L_1L_2} + \cdots, \tag{4.68}$$

where

$$t^\alpha_l(k) = 2\int dr r^2 j_l(kr) t^\alpha_l(r,r') j_l(kr') \tag{4.69}$$

$$\hat{G}^{\alpha\beta(1)}_{L_1,L_2} = \sum_L \sum_{\gamma(\neq A,B)} G^{\alpha\gamma}_{L_1,L} t^\gamma_l(k) G^{\gamma\beta}_{L,L_2} = t^\alpha_{l_1}(k)^{-1}\left[X^2\right]^{\alpha\beta}_{L_1L_2} \tag{4.70}$$

$$X^{\alpha\beta}_{L_1L_2} = t^\alpha_{l_1}(k) G^{\alpha\beta}_{L_1L_2}(1-\delta_{\alpha\beta}) \tag{4.71}$$

The free propagator G^{AB} should be subtracted in Z'^{AB} because of $G^{AB} \neq 0$ for $A \neq B$. When $A = B$, Z'^{AA} is equal to Z owing to $G^{AA} = 0$. We obtain the infinite scattering term with Z'.

$$\begin{aligned}
&\langle\varphi_c|\,\Delta^* g_A \left(\sum_{\alpha(\neq A,B)} t_\alpha + \sum_{\beta(\neq\alpha,A)} t_\alpha g_0 \sum_{\alpha(\neq B)} t_\beta + \cdots\right) g_B \delta v_B g_A \Delta\,|\varphi_c\rangle \\
&\quad = \frac{1}{\pi}\sum_s s\rho_{>,1}{}^2 \sum_L m Z'^{AB}_{1m_p,L}[\xi^s_B]^{Rj}_l G^{BA}_{L,1m_p},
\end{aligned} \tag{4.72}$$

$$\begin{aligned}
&\langle\varphi_c|\,\Delta^* g_A \delta v_B g_B \left(\sum_{\alpha(\neq A,B)} t_\alpha + \sum_{\beta(\neq\alpha,B)} t_\alpha g_0 \sum_{\alpha(\neq A)} t_\beta + \cdots\right) g_A \Delta\,|\varphi_c\rangle \\
&\quad = \frac{1}{\pi}\sum_s s\rho_{>,1}{}^2 \sum_L m G^{AB}_{1m_p,L}[\xi^s_B]^{Rj}_l Z'^{BA}_{L,1m_p}
\end{aligned} \tag{4.73}$$

where $[\xi]^{jR} = [\xi]^{Rj}$.

- $\langle\varphi_c|\,\Delta^* g_A \left(\sum_{\alpha(\neq A,B)} t_\alpha + \sum_{\beta(\neq\alpha,A)} t_\beta g_0 \sum_{\alpha(\neq B)} t_\alpha + \cdots\right) g_B \delta v_B g_B v_B g_A \Delta\,|\varphi_c\rangle$

Similarly to the extension from (4.59) to (4.72), the first order term of t is obtained from (4.61).

$$\begin{aligned}
&\langle\varphi_c|\,\Delta^* g_A \sum_{\alpha(\neq A,B)} t_\alpha g_B \delta v_B g_B v_B g_A \Delta\,|\varphi_c\rangle \\
&\quad= \frac{1}{\pi}\sum_s s\rho_{>,1}{}^2 \sum_L m G^{(1)AB}_{1m_p,L}\left(-2ik[(\xi v)^s_B]^{Rj}_l\right) G^{BA}_{L,1m_p} \\
&\quad= \frac{1}{\pi}\sum_s s\rho_{>,1}{}^2 \sum_L m G^{(1)AB}_{1m_p,L}\left(-2ik[(v\xi)^s_B]^{jR}_l\right) G^{BA}_{L,1m_p} \qquad (4.74)
\end{aligned}$$

The infinite order term of t is obtained by replacement of $G^{(1)AB}$ to Z'.

$$\begin{aligned}
&\langle\varphi_c|\,\Delta^* g_A \left(\sum_{\alpha(\neq A,B)} t_\alpha + \sum_{\beta(\neq\alpha A)} t_\beta g_0 \sum_{\alpha(\neq B)} t_\beta + \cdots\right) g_B \delta v_B g_B v_B g_A \Delta\,|\varphi_c\rangle \\
&\quad= \frac{1}{\pi}\sum_s s\rho_{>,1}{}^2 \sum_L m Z'^{AB}_{1m_p,L}\left(-2ik[(v\xi)^s_B]^{jR}_l\right) G^{BA}_{L,1m_p} \qquad (4.75) \\
&\langle\varphi_c|\,\Delta^* g_A v_B g_B \delta v_B g_B \left(\sum_{\alpha(\neq A,B)} t_\alpha + \sum_{\beta(\neq\alpha B)} t_\beta g_0 \sum_{\alpha(\neq A)} t_\beta + \cdots\right) g_A \Delta\,|\varphi_c\rangle \\
&\quad= \frac{1}{\pi}\sum_s s\rho_{>,1}{}^2 \sum_L m G^{AB}_{1m_p,L}\left(-2ik[(v\xi)^s_B]^{jR}_l\right) Z'^{BA}_{L,1m_p} \qquad (4.76)
\end{aligned}$$

where $[(\xi v)]^{Rj} = [(v\xi)]^{jR}$

Therefore, the multiple scattering term $U^{Z'G}_{11,sc}$ is given by

$$\begin{aligned}
U^{Z'G}_{11,sc}(m_p) = -\frac{2}{\pi}\mathrm{Im}\sum_s s\rho_{>,1}{}^2 \sum_{B(\neq A)}\sum_{l>0}\left\{[\xi^s_B]^{Rj}_l - 2ik[(v\xi)^s_B]^{jR}_l\right\} \\
\times \sum_{m(\neq 0)} m\left(Z'^{AB}_{1m_p,L} G^{BA}_{L,1m_p} + G^{AB}_{1m_p,L} Z'^{BA}_{L,1m_p}\right). \qquad (4.77)
\end{aligned}$$

If we approximate $Z'G + GZ'$ as $2Z'G$, $U^{Z'G}_{11,sc}$ becomes

$$\begin{aligned}
U^{Z'G}_{11,sc}(m_p) = -\frac{2}{\pi}\mathrm{Im}\sum_s s\rho_{>,1}{}^2 \sum_{B(\neq A)}\sum_{l>0}\left\{2[\xi^s_B]^{Rj}_l - 4ik[(v\xi)^s_B]^{jR}_l\right\} \\
\times \sum_{m(\neq 0)} m Z'^{AB}_{1m_p,L} G^{BA}_{L,1m_p}. \qquad (4.78)
\end{aligned}$$

$U^{Z'Z'}_{11sc}$

- $\langle\varphi_c|\,\Delta^* g_A \left(\sum_{\beta(\neq A,\alpha)} t_\beta + \cdots\right) g_\alpha \delta v_\alpha g_\alpha \left(\sum_{\beta'(\neq A,\alpha)} t_{\beta'} + \cdots\right) g_A \Delta\,|\varphi_c\rangle$

The lowest order term is obtained by small changes of (4.72). The photoelectron migration from A to α via β' relaces $G^{\alpha A}$ and $[\xi]^{Rj}$ with $G^{(1)\alpha A}$ and $[\xi]^{RR}$, respectively. The replacement of $G^{(1)}$ by Z' provides the infinite order term.

$$\begin{aligned}
&\langle\varphi_c|\,\Delta^* g_A \left(\sum_{\beta(\neq A,\alpha)} t_\beta + \cdots\right) g_\alpha \delta v_\alpha g_\alpha \left(\sum_{\beta'(\neq A,\alpha)} t_{\beta'} + \cdots\right) g_A \Delta\,|\varphi_c\rangle \\
&\quad = \frac{1}{\pi}\sum_s s{\rho_{>,1}}^2 \sum_L m Z'^{A\alpha}_{1m_p,L}[\xi^s_\alpha]^{RR}_l Z'^{\alpha A}_{L,1m_p} \qquad (4.79)
\end{aligned}$$

The infinite multiple scattering term $U^{Z'Z'}_{11,sc}$ is obtained by (4.56).

We summarize the results as

$$\begin{aligned}
U^{GG}_{11,sc}(m_p) &= -\frac{2}{\pi}\mathrm{Im}\sum_s s{\rho_{>,1}}^2 \sum_{B(\neq A)}\sum_{l>0}\left\{[\xi^s_B]^{jj}_l - 4ik[(v\xi)^s_B]^{jj}_l - 4k^2[(v\xi v)^s_B]^{jj}_l\right\} \\
&\quad\times \sum_{m(\neq 0)} m G^{AB}_{1m_p,L} G^{BA}_{L,1m_p}, \qquad (4.66)\\
U^{Z'G}_{11,sc}(m_p) &= -\frac{2}{\pi}\mathrm{Im}\sum_s s{\rho_{>,1}}^2 \sum_{B(\neq A)}\sum_{l>0}\left\{[\xi^s_B]^{Rj}_l - 2ik[(v\xi)^s_B]^{jR}_l\right\} \\
&\quad\times \sum_{m(\neq 0)} m\left(Z'^{AB}_{1m_p,L} G^{BA}_{L,1m_p} + G^{AB}_{1m_p,L} Z'^{BA}_{L,1m_p}\right), \qquad (4.78)\\
U^{Z'Z'}_{11,sc}(m_p) &= -\frac{2}{\pi}\mathrm{Im}\sum_s s{\rho_{>,1}}^2 \sum_\alpha\sum_{l>0}[\xi^s_\alpha]^{RR}_l \sum_{m(\neq 0)} m Z'^{A\alpha}_{1m_p,L} Z'^{\alpha A}_{L,1m_p}. \qquad (4.80)
\end{aligned}$$

In the summation of m, the homogeneous terms of G and Z' satisfy:

$$\begin{aligned}
\sum_m m G^{AB}_{1m_p,L} G^{BA}_{L,1m_p} &= \sum_m m G^{BA}_{\overline{L},1\overline{m}_p} G^{AB}_{1\overline{m}_p,\overline{L}} \\
&= \sum_m (-1)\overline{m} G^{AB}_{1\overline{m}_p,\overline{L}} G^{BA}_{\overline{L},1\overline{m}_p} \\
&= -\sum_m m G^{AB}_{1\overline{m}_p,L} G^{BA}_{L,1\overline{m}_p}, \qquad (4.81)\\
\sum_m m Z'^{AB}_{1m_p,L} Z'^{BA}_{L,1m_p} &= -\sum_m m Z'^{AB}_{1\overline{m}_p,L} Z'^{BA}_{L,1\overline{m}_p}. \qquad (4.82)
\end{aligned}$$

Furthermore,

$$\sum_m m Z'^{AB}_{1m_p,L} G^{BA}_{L,1m_p} = -\sum_m m G^{AB}_{1\overline{m}_p,L} Z'^{BA}_{L,1\overline{m}_p}, \tag{4.83}$$

$$\sum_m m \left(Z'^{AB}_{1m_p,L} G^{BA}_{L,1m_p} + G^{AB}_{1m_p,L} Z'^{BA}_{L,1m_p} \right)$$

$$= -\sum_m m \left(Z'^{AB}_{1\overline{m}_p,L} G^{BA}_{L,1\overline{m}_p} + G^{AB}_{1\overline{m}_p,L} Z'^{BA}_{L,1\overline{m}_p} \right) \tag{4.84}$$

$$\approx -2\sum_m m Z'^{AB}_{1\overline{m}_p,L} G^{BA}_{L,1\overline{m}_p}. \tag{4.85}$$

By using this relation, we obtain the XMCD intensity by the difference between up and down spin components with same helicity of incident X-rays.

$$\Delta U_{11,sc} = U_{11,sc}(m_p = +1) - U_{11,sc}(m_p = -1) = 2U_{11,sc}(m_p = +1) \tag{4.86}$$

$$= 2(U^{\uparrow}_{11,sc}(m_p = +1) - U^{\downarrow}_{11,sc}(m_p = +1)) \tag{4.87}$$

If the incident X-rays are linearly polarized (for instance, $m_p = 0$ with polarization parallel to the z-axis), $U_{11,sc}$ vanish. For instance, from (4.81),

$$\sum_m m G^{AB}_{1m_p,L} G^{BA}_{L,1m_p} = \sum_{m>0}^{l} m \left(G^{AB}_{1m_p,L} G^{BA}_{L,1m_p} - G^{AB}_{1\overline{m}_p,L} G^{BA}_{L,1\overline{m}_p} \right), \tag{4.88}$$

and this becomes zero when $m_p = 0$. The other relations (4.82) and (4.84) give the same result.

The radial integrals $[\cdots]^{\phi_1,\phi_2}$ are also summarized here with photoelectron wave functions ϕ_1 and ϕ_2, which are either the spherical Bessel function j corresponding to the free photoelectron solution, or the numerical regular solution R.

$$[\xi^s]^{\phi_1\phi_2}_l = \int \phi_{1,l}(r)\xi^s(r)\phi_{2,l}(r)r^2 dr, \tag{4.89}$$

$$[(v\xi)^s]^{\phi_1\phi_2}_l = \int \phi_{1,l}(r)v^s(r)r^2 dr \int R^s_l(r_<)\hat{f}^s_l(r_>)\xi^s(r')\phi_{2,l}(r')r'^2 dr', \tag{4.90}$$

$$[(v\xi v)^s]^{\phi_1,\phi_2}_l = \int \phi_{1,l}(r)v^s(r)r^2 dr \int R^s_l(r_<)\hat{f}^s_l(r_>)\xi^s(r')r'^2 dr'$$

$$\times \int R^s_l(r'_<)\hat{f}^s_l(r'_>)v^s(r'')\phi_{l,1}(kr'')r''^2 dr''. \tag{4.91}$$

where the scattering site index is omitted. The MS factor $Z'^{\alpha A}$ includes single or more scatterings in a photoelectron path from A to α sites: G^{BA} is not included. The single scattering $U^{GG}_{11,sc}$ has three different radial integrals include the SOI on a scattering site.

The scattering factor $G^{AB}G^{BA}$ corresponds to the single scattering between A and B sites, while $Z'^{AB}G^{BA}$ describes the infinite MS after the propagation from A to B sites. The scattering factor $Z'^{A\alpha}Z'^{\alpha A}$

The single, semi infinite, and infinite scattering terms $U^{GG}_{11,sc}$, $U^{Z'G}_{11,sc}$ and $U^{Z'Z'}_{11,sc}$ are calculated in the next section, respectively.

4.3 Fe K-edge for BCC iron

Firstly, I apply the present XMCD theory to the BCC iron system to compared with the previous one [23, 21].

4.3.1 Calculation

The calculation cluster radius is about 7 Å, including 113 Fe atoms. The lattice constant 2.87 Å is adopted. The each site potential and electron density are calculated by using the STUTTGART-TB-LMTO-ASA program [90, 91] with von Barth-Hedin local exchange correlation [92, 93]. The linear muffin-tin orbital (LMTO) method use the muffin-tin approximation, and has similarity to the MS calculation. The calculated magnetic moment of BCC iron with no hole is 2.217 μ_B which is very close to the observed one (2.216 μ_B) [94]. The partial wave in MS matrix is taken up to $l = 3$, which provide converged results in XAS and XMCD energetic region. In this calculation, photoelectron damping effects are not considered to show spectral structure clearly.

4.3.2 Results & Discussion

Figures 4.1(a) and (b) show calculated Fe K-edge XAS and XMCD spectra for BCC iron, respectively. The experimental results [79] are also shown in Fig. 4.1. The XAS spectra are normalized to main peak intensity. XMCD intensity is obtained in percentage of the main peak of the corresponding XAS spectrum.

In Fig. 4.1(a), the calculated spectrum is obtained by T_{11} in eq. (2.14a), and shows features of the experimental one. In Fig. 4.1(b), the three calculated spectra are obtained by $\Delta I = \Delta U_{11} + 2\Delta T_{12}$ (all), $\Delta U_{11,A} + 2\Delta T_{12}$ (non-scattering) and $\Delta U_{11,sc}$ (scattering). Note that the non-scattering term $\Delta U_{11,A} + 2\Delta T_{12}$ includes usual MS, but not the SOI in

scattering process. The experimental result is shown as tenfold one for comparison. The most important point is the comparable scattering term to the non-scattering one. In addition, the total XMCD term ΔI is improved by the scattering term though the scale factor is still needed. These results indicate that the SOI in scattering processes is still important for K-edge XMCD spectra of TM. This contradicts to the previous analysis with single scattering calculations: the SOI on scatterer sites was negligible [23]. Figure 4.2 shows $\Delta U_{11,sc}$ and its components $\Delta U^{GG}_{11,sc}$, $\Delta U^{Z'G}_{11,sc}$ and $\Delta U^{Z'Z'}_{11,sc}$. The all components are comparable in intensity: the single scattering term $\Delta U^{GG}_{11,sc}$ neglected before still has contribution.

To investigate the discrepancy, I check the integrants of $U^{GG}_{11,sc}$, $U^{Z'G}_{11,sc}$ and $U^{Z'Z'}_{11,sc}$. Figures 4.3(a) and (b) show the radial integrals $[\xi]^{jj}$ and $-4ik[(\xi v)]^{jj}$, and $-4k^2[(v\xi v)]^{jj}$ in the single scattering term $U^{GG}_{11,sc}$ with $l = 1$ and 2, respectively. The integral $[\xi]^{jj}$ is real value, while the others are complex. In Fig. 4.3, $-4k^2[(v\xi v)]^{jj}$ shows dominant contribution. On the other hand, $[\xi]^{jj}$ and $[(\xi v)]^{jj}$ are negligible compared with $[(v\xi v)]^{jj}$. In particular, the negligible intensity of $[\xi]^{jj}$ agrees with the previous result. In eqs. (4.89) and (4.90), $[\xi]^{jj}$ and $[(\xi v)]^{jj}$ have a direct overlap between the free solution j and SOI ξ. Because the intensity of the SOI ξ is proportional to the gradient of the site potential v, ξ is strong only near the nucleus. The free photoelectron described by the spherical Bessel function j with $l \neq 0$ has small amplitude near the nucleus. Thus, the direct overlap is negligible. In eq. (4.91), $[(v\xi v)]^{jj}$ has the indirect j-ξ overlap mediated by site potential v, the numerical solution R and $\hat{f}$. Since the solutions R and $\hat{f}$ are already affected by site attractive potential v, they have larger amplitudes near the nucleus and overlap with ξ than the free solution j. This makes $[(v\xi v)]^{jj}$ as the dominant contribution to the U^{GG} terms. Note that dispersion peaks of $[(v\xi v)]^{jj}$ with $l = 2$ in Fig. 4.3(b) is resonance of photoelectron d-wave corresponding to a step of phase shift with no singular point.

I also check the radial integrals of $U^{Z'G}$ and $U^{Z'Z'}$. Figure 4.4 shows the radial integral $[\xi]^{Rj}$ and $-4ik[(v\xi)]^{jR}$ in $U^{Z'G}$. In Figs. 4.4(a) and (b) ($l = 1$ and 2), the integral $-4ik[(v\xi)]^{jR}$ is dominant. Similarly to $[(v\xi)v]^{jj}$, the potential v mediates between j and ξ in $[(v\xi)]^{jR}$. As described above, the direct overlap between R and ξ has substantial intensity since the numerical solution R is attracted to the nucleus by v. That result is also obtained from the radial integral $[\xi]^{RR}$ in $U^{Z'Z'}$ in Figure 4.5.

I conclude that the SOI at scatterer sites are still important to understand XMCD spectra. Moreover, when a photoelectron is affected by the SOI, the site potential also affects it simultaneously. Otherwise, the SOI at scatterer sites only has negligible contribution.

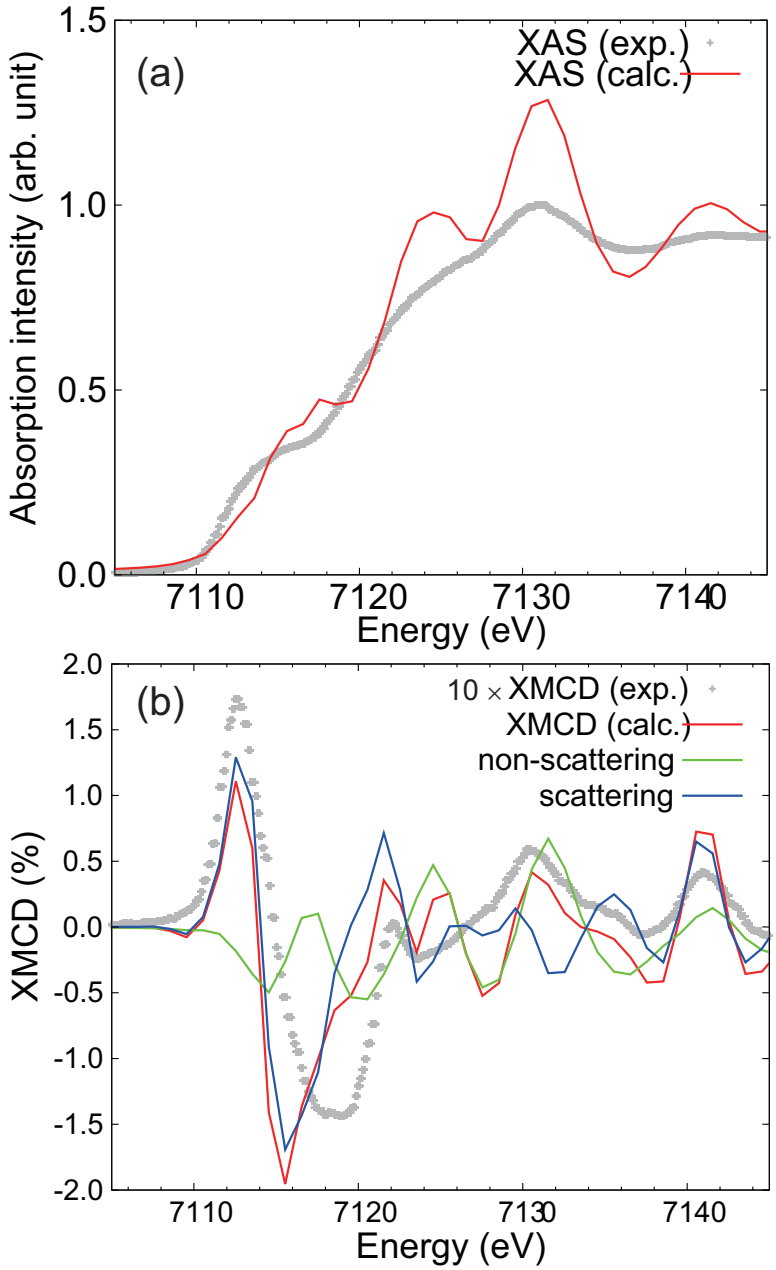

Figure 4.1: Calculated Fe K-edge (a) XAS and (b) XMCD spectra for BCC iron. The calculated XAS spectrum is obtained by T_{11} averaged in ±helicity of incident lights. The non-scattering and scattering XMCD spectra correspond to $U_{11,A} + 2T_{12}$ and $U_{11,sc}$, respectively. The total calculated XMCD spectrum is the sum of the non-scattering and scattering ones. The observed results are also shown for comparison [79]

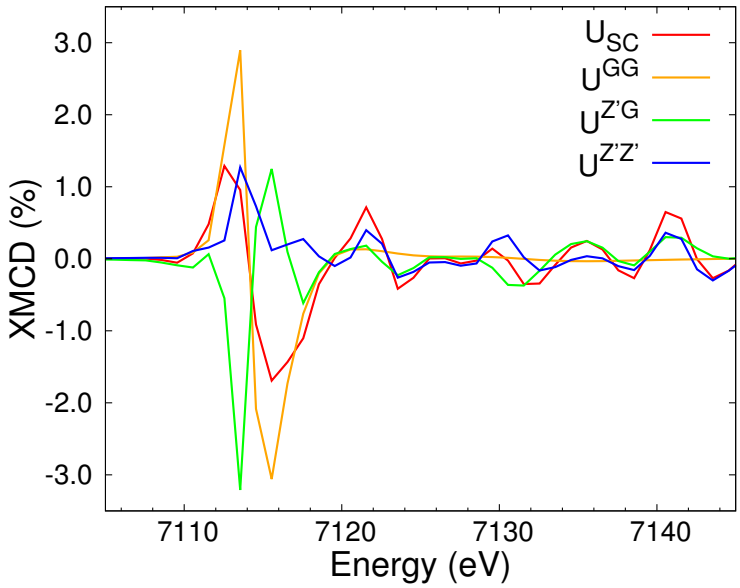

Figure 4.2: The scattering term $U_{11,sc}$ and its components: $U^{GG}_{11,sc}$, $U^{Z'G}_{11,sc}$ and $U^{Z'Z'}_{11,sc}$.

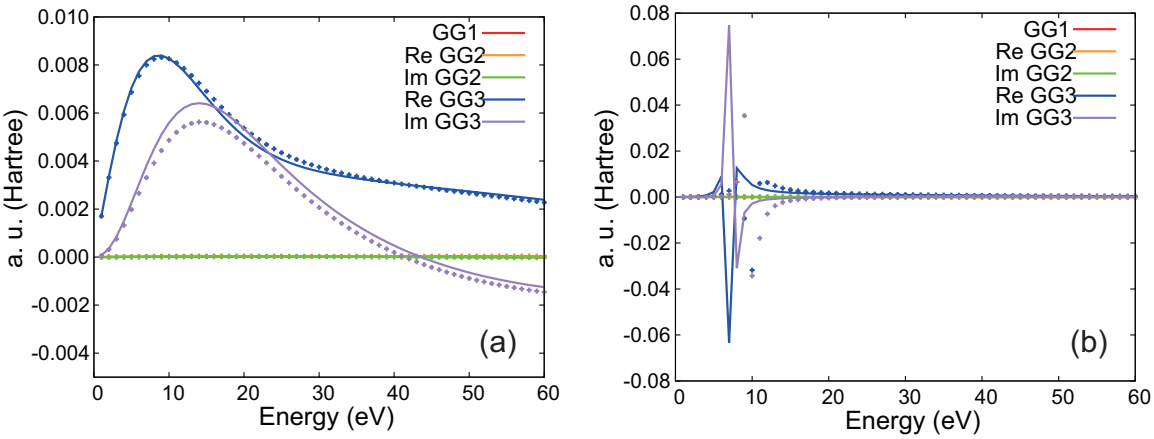

Figure 4.3: The components of $U^{GG}_{11,sc}$ with partial waves $l = 1$ (a) and 2 (b) at a scatterer Fe site. The terms $GG1$, 2 and 3 are $[\xi]^{jj}$, $-4ik[(\xi v)]^{jj}$ and $-4k^2[(v\xi v)]^{jj}$, respectively. The lines and points show for up and down spin, respectively.

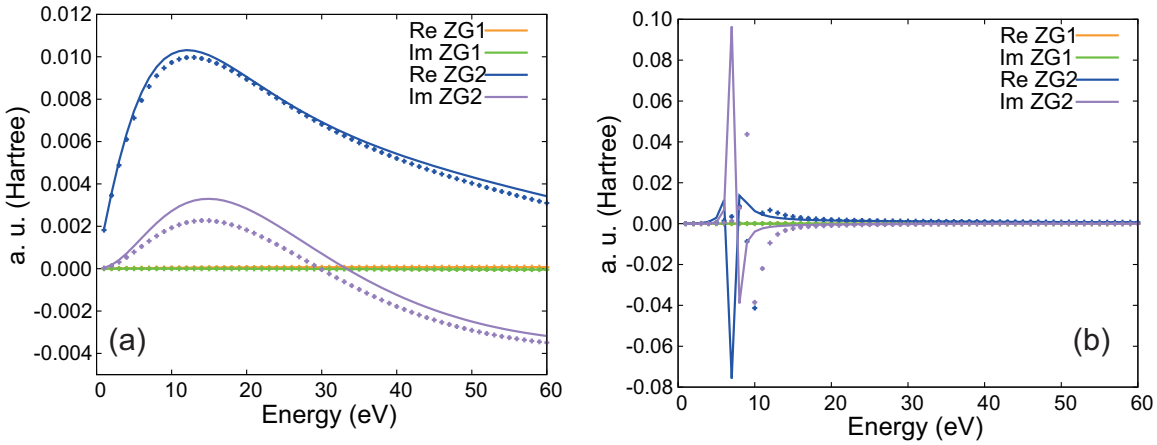

Figure 4.4: The components of $U^{ZG}_{11,sc}$ with partial waves $l = 1$ (a) and 2 (b) at a scatterer Fe site. The terms $ZG1$ and 2 are $[\xi]^{Rj}$ and $-4ik[(v\xi)]^{jR}$, respectively. The lines and points show for up and down spin, respectively.

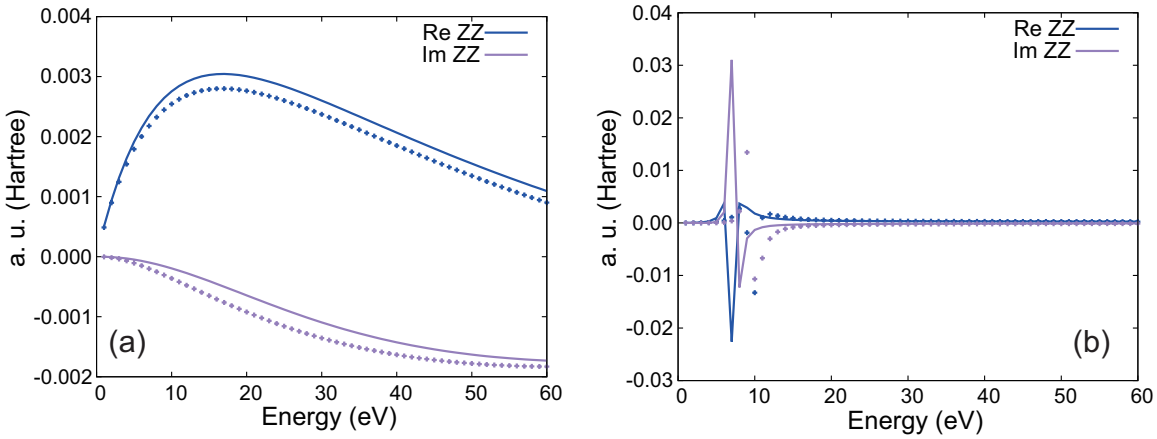

Figure 4.5: The component $[\xi]^{RR}$ of $U^{ZZ}_{11,sc}$ with partial waves $l = 1$ (a) and 2 (b) at a scatterer Fe site. The terms ZZ shows $[\xi]^{RR}$. The lines and points show for up and down spin, respectively.

4.4 C K-edge for graphene/Ni(111)

4.4.1 Introduction

Graphene is an almost 2-dimensional material composed of carbon atoms. Its characteristic band structure, called the Dirac cone, provides extremely high electron mobility in principle because of linear band dispersion indicating that electrons obey relativistic theory. The graphene's Dirac cone where valence and conduction bands contact at point is originated from the honey comb structure: two carbon atoms in a unit cell have C-C bonds with only the counterpart sites. To control band gaps at Dirac cones, structural changes or other perturbation to disturb symmetry are required. Many researchers have been struggling to control the Dirac cone in particular opening and closing band gaps at the Dirac cone. For spintronic fields, a theoretical work indicates that graphene on ferromagnetic metal (Ni and Co) interface acts as a spin filter [95]. In addition, since the SOI on carbon is small, long spin relaxation times on graphene was expected. However, short relaxation (50 $\sim$ 200 ps) involved with contact-induced relaxation was reported in the graphene/Co system [96]. The low spin injection efficiency ($\sim$ 1 %) due to the conduction mismatch between graphene and ferromagnetic metal is also problem [96]. The problems of the spin relaxation and injection efficiency is improved to 400-600 ps and 26 $\sim$ 30 %, respectively, at 300 K by tunnel contact with MgO tunnel barrier [96].

To understand fundamental physical properties of these systems for further application development, many experimental measurements and ab-initio calculations have been performed in particular the graphene on Ni(111) system. STM and low-energy electron diffraction (LEED) results show small lattice mismatch (about 1.3 %) between graphene and Ni substrate [97, 98]. Thus, a well-ordered $p(1\times1)$ overstructure with graphene can be relatively easily obtained on Ni surface than other transition metal one. Impact collision ion scattering spectroscopy, LEED and angle-scanned photoelectron diffraction (PED) experiments indicate the distance between the graphene and Ni surface about 2.11 Å [97, 99, 100]. This distance is shorter than an ordinary physisorption one (cf. $\sim$ 3.3 Å for graphene on Cu [101]). XAS measurements for graphene/Ni(111) confirmed the orbital orientation and hybridization at the surface and interface [86, 98]. The depth-resolved Ni $L_{2,3}$-edge XMCD spectra indicates that the first and deeper Ni layers have the out-of-

and in-plane easy-axis, respectively [86]. The XMCD experimental setting is shown in Figure 4.6. Auger electrons which accompany with X-ray absorption were detected with their emission angles θ by an imaging type detector composed of a phosphor screen and a micro-channel plate. The XMCD intensity was obtained by fixing circular polarization of incident X-rays in remanence, and changing the direction of pulsed magnetic fields. The incident angle α of the X-rays and magnetic field is defined with respect to the sample surface. Moreover, in Figure 4.7, C K-edge XAS and XMCD spectra of graphene on Ni(111) was also obtained by using the same setting with a partial electron yield mode [86]. The similar spectra were also reported in another paper [98]. From the α sensitivity, the A_1 and A_2 (A_3 and A_4) peaks are assigned as excitation to π^* (σ^*) states. Remarkably, the C K-edge XMCD intensity with the order of 10 % (cf. 0.2 % for Fe K-edge XMCD of BCC iron) clearly appears at the π^* peak region in spite of the small SOI on carbon atoms. This result suggests that carbon atoms have large orbital moments due to strong hybridization with Ni d orbitals; however theoretical studies for the XMCD spectra have not been done yet .

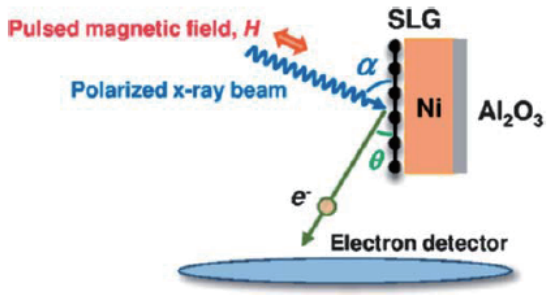

Figure 4.6: The schematic figure of the set-up of the XAS and XMCD measurements for the graphene/Ni(111) system [86] - Reproduced by permission of The Royal Society of Chemistry.

Ab-initio calculations for the graphene/Ni(111) systems have attracted much attention because the adsorption mechanism of graphene on Ni(111) surface is still ambiguous due to the interface distance about $\sim$ 2.1 Å described above: it is difficult to decide whether the physisorption or chemisorption (cf. $\sim$ 3.3 and 1.9 Å for graphene on Cu, and Nickel carbides [102], respectively). To discuss the adsorption, construction of the structural model for graphene on Ni(111) is quite important. Figures 4.8 and 4.9 show

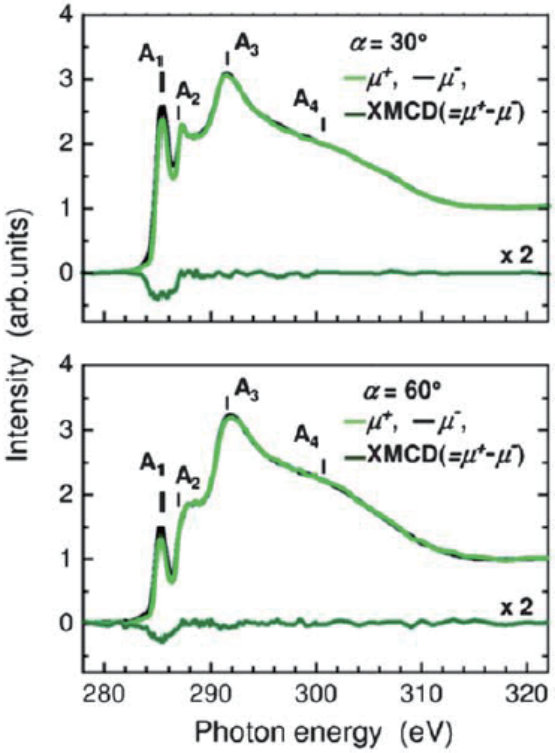

Figure 4.7: C K-edge XAS (μ^+: light green, μ^-: black) and XMCD (dark green) spectra [86] - Reproduced by permission of The Royal Society of Chemistry. The upper and lower panels show $\alpha = 30°$ and 60°, respectively, defined in Fig. 4.6.

the proposed structural models, which neglect the lattice mismatch to keep the unit cell small and reduce the calculation cost. Ni atoms in the first (green), second (yellow) and third (red) layers are designated as top, hcp and fcc sites, respectively. Carbon atoms are above any Ni sites for top-hcp, top-fcc and hcp-fcc structures in Fig. 4.8, while one C-C bond is above a Ni site and C atoms locate above between two any nonequivalent Ni sites for bridge-top, bridge-hcp and bridge-fcc in Fig. 4.9. The earlier LEED result suggests that the top-fcc structure is most preferable. After that, many studies have been done on the basis of the top-fcc structure [86, 95, 98, 100]. The earlier density functional theory (DFT) calculation support the LEED results and indicated that the top-fcc structure is more stable than the top-hcp and hcp-fcc [103]. That calculation also suggested that two different carbon atoms in an unit cell have opposite spin magnetic moments each other. On the other hand, possibility of the bridge-top structure was discussed by using DFT calculations [104]. The bridge-top structure provides the parallel spin polarization on graphene carbon and Ni atoms at the Fermi energy, which agrees with spin polarized

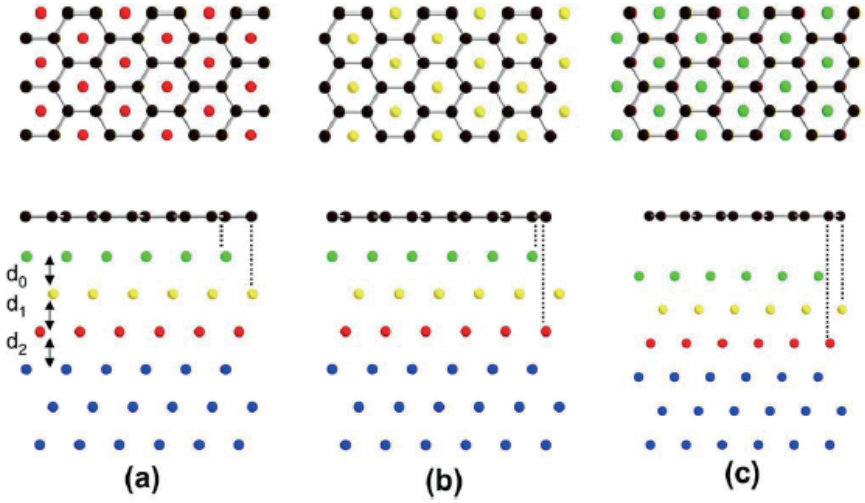

Figure 4.8: Structures of graphene/Ni(111) defined as (a) top-hcp, (b) top-fcc and (c) hcp-fcc. The upper and lower panels show the top and side views of them, respectively. Ni atoms in the first (green), second (yellow) and third (red) layers are designated as top, hcp and fcc sites, respectively. The dashed lines show the correspondence between carbon (black) and Ni sites. Reprinted figure with permission from [104] Copyright(2008) by the American Physical Society.

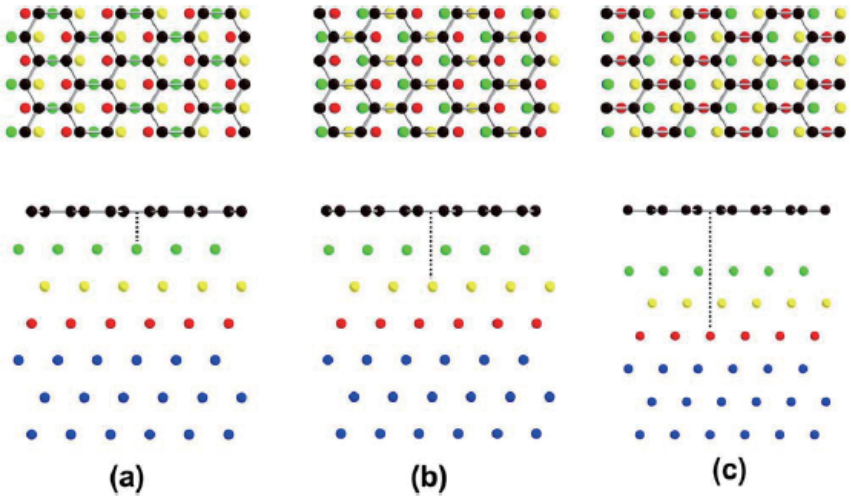

Figure 4.9: Structures of graphene/Ni(111) defined as (a) bridge-top, (b) bridge-hcp and (c) bridge-fcc. The dashed lines show the correspondence between a C-C bond and a Ni site. Reprinted figure with permission from [104] Copyright(2008) by the American Physical Society.

metastable deexcitation spectroscopy measurements [105] Recently, DFT calculations including van der Waals interaction has been performed: the top-fcc and bridge-top structures are nearly degenerate [106, 107]. LEED, XPD, XPS and STM measurements support the updated result and indicates the coexistence of the several structures [97, 106, 108]. Furthermore, a comprehensive DFT study on the partial density of state with various structures shows that two nonequivalent carbons with the top-fcc and bridge-top structures have antiparallel and parallel spin polarization each other, respectively, at the Fermi energy [106]. This coincides with the previous calculated results [103, 105].

In this section, I calculate C K-edge XMCD spectra for graphene on Ni(111) by using the theory described in the previous section. The SOI at Ni sites shows the dominant contribution to the XMCD spectra.

4.4.2 Calculation

I employ the top-fcc and bridge-top structures as shown in Figs. 4.8 and 4.9 for calculation clusters. Two nonequivalent carbon sites above the first and third layer Ni atoms in the top-fcc structure are defined as C(top) and C(fcc), respectively. While, the carbon sites C(hcp) (C(fcc)) in the bridge-top structure is located between the first and second (first and third) layer Ni atoms viewed from the top. Distances between graphene and the first Ni layers are set to 2.11 and 2.07 Å, and between the first and second Ni layers are 1.98 and 2.00 Å in the top-fcc and bridge-top structures, respectively, obtained by DFT calculations [106]. The lattice constant 3.52 Å is used for FCC Ni. Then, the Ni interlayer distance bellow the second Ni layer is about 2.03 Å. The lattice constant of graphene on Ni(111) is commensurate to Ni(111) surface for simplicity. Empty spheres (ES) are put above the graphene to consider the surface potential. In the first ES layer, the ES-C distance is the same as the C-C bond. Each ES interlayer distance is set to the same as the one between the first ES layer and graphene. For MS calculations, the cluster radii are about 10 Å, which is not enough to obtain the size convergence of the calculated spectra for free-standing graphene systems [109]. Note that the requirement of the huge cluster radius is particular for graphene because of its honeycomb structure and long core hole lifetime of carbon. However, in the graphene on Ni system, the C-Ni distance is close and may partially break the pure graphene symmetry, which would assist

the cluster-size convergence. Thus, the cluster size convergence is interesting at the 10 Å radius. Moreover, qualitative discussion about effects of the scattering site SOI on XMCD spectra could be available.

The each site potential and electron density to calculate XAS and XMCD spectra are obtained by using the STUTTGART TB-LMTO-ASA program [90, 91] in the same way as Sec. 4.3.1. The site potential V_C at the absorbing carbon and its nearest carbon sites in the system with a core hole is obtained by follows:

$$V_C(gNi; c) = \frac{V_C(gNi)}{V_C(fg)} \times V_C(fg; c). \tag{4.92}$$

The potential $V_C(gNi)$ and $V_C(fg)$ means the one in graphene on Ni and free-standing graphene commensurate to the Ni(111) surface, respectively. The additional symbol c represents the core hole. The potential at Ni, ES and farther C sites are chosen as the one in graphene on Ni systems with no core hole. I have already checked that the core hole effect on potential and electron density is important only on the absorbing site and the first nearest neighbors in bulk Ni and free-standing graphene, respectively. The number of vacuum (ES) and Ni layers in calculation slabs are 5 and 9 layers (about 7.5 and 20 Å), respectively, as shown in Figs. 4.8 and 4.9. I employ a $36 \times 36 \times 2$ k-point grid. For the free-standing graphene calculation, the configuration of ESs are the same as graphene on Ni surface, i.e. graphene sheets are sandwiched by ES layers.

4.4.3 Results & Discussion

Before analyses for XMCD spectra, I calculate the spin-resolved projected density of states (PDOS) of carbon atoms and the first Ni layer in the top-fcc and bridge top-fcc structural systems with the no core hole ground state, as shown in Figure 4.12. For comparison, the total and p component of DOSs of free-standing graphene carbon are also shown with no spin polarization. All the calculated results of graphene/Ni DOS without Van der Waals interaction are similar to the reported calculation [106], indicating that Van der Waals interaction largely influences only on structural optimization. The calculated free-standing graphene DOS reproduce its linear energy-band dispersion near E_F. Every carbon atom has strong hybridization with Ni states at about 0.5 eV in Fig. 4.12. For the top-fcc, the carbon site C(fcc) has large spin polarization parallel to the

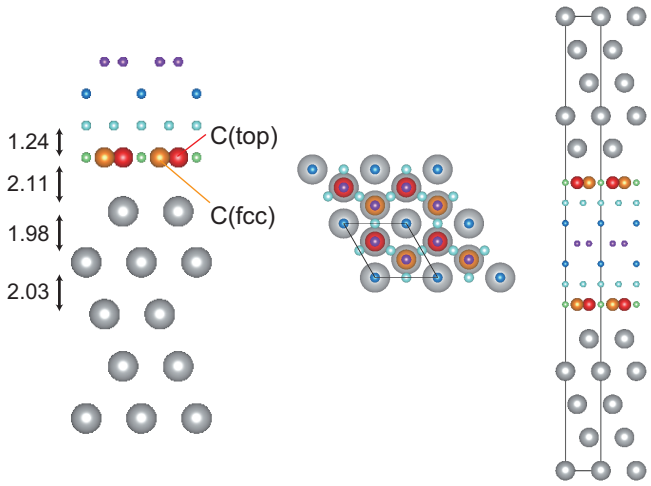

Figure 4.10: Side (left, right) and top (center) views of the top-fcc structural model of graphene on Ni(111) surface. The right figure shows the slab for the LMTO calculation. The nonequivalent carbon and Ni atoms shown by red, orange and grey balls, respectively. The ESs are represented by light green, light blue, blue and purple balls. The ES in the graphene layer (light green) is beneath the second ES layer (blue). The interlayer distances C-C and Ni-Ni near the surface are obtained from Ref. [106].

.

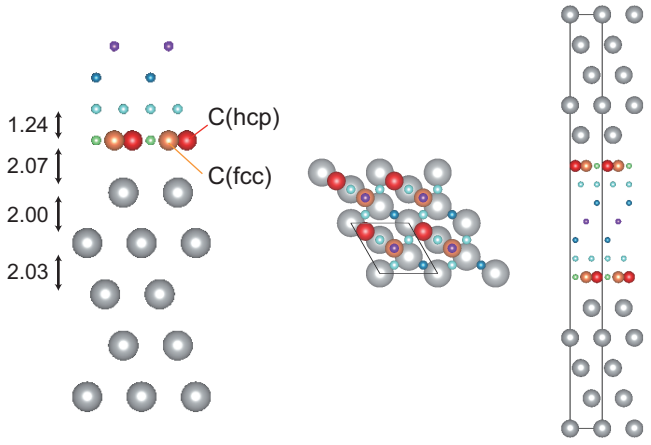

Figure 4.11: Side (left, right) and top (center) views of the bridge-top structural model of graphene on Ni(111) surface in the same way of Fig. 4.10.

.

Ni one at E_F, whereas C(top) has hybridization states at about -2.5 eV alternatively. Magnetic moments -0.01 and 0.006 μ_B on C(top) and C(fcc) are obtained, respectively. The magnetic moment are estimated by the difference between majority and minority spin electrons in the atomic sphere. The plus sign of magnetic moments are defined as parallel to Ni one. The first, second and deeper layer Ni atoms have 0.12, 0.66 and 0.59 μ_B, respectively. The magnetic moment of deeper Ni layers is close to the calculated and observed ones of FCC nickel (0.6070 and 0.6155 μ_B) [94]. For the bridge-top, both C(hcp) and C(fcc) have the same DOS structure ,and spin polarization parallel to the Ni one at E_F in Fig. 4.12, which is consistent with the previous result [105]. The two DOSs indicate that hybridization characters with Ni atoms are similar between C(hcp) and C(fcc). Moreover, a sharp peak of free-standing graphene at -2.5 eV merges with Ni states, and disperses for the bridge-top structure. Their magnetic moments -0.001 (C(hcp)) and -0.003 (C(fcc)) μ_B antiparallel to the Ni one are obtained though the values are negligibly small. The first, second and deeper layer Ni atoms have 0.17, 0.60 and 0.57 μ_B, respectively, which shows the similar trend for the top-fcc case. By using the potential which provide these calculated results, I calculate XMCD spectra.

Figure 4.13 shows calculated C K-edge XAS and XMCD spectra for the top-fcc and bridge-top graphene/Ni systems with the incident X-ray angles $\alpha = 30$ and 60°. The observed spectra [86] which normalized by the XAS spectra at about 292 eV (σ^* peak) also shown for comparison. The π^* and σ^* peaks of the observed XAS spectra at about 285 and 292 eV are assigned by the polarization (incident X-ray angle α) dependence. The calculated spectra are shifted to adjust their σ^* peak position, and normalized in the same way as the observed ones. In Fig. 4.13, one notices the α dependence of the calculated spectra similar to the observed ones. Incident circularly polarized X-rays with $\alpha = 30°$ relatively has out-of-plane polarization compared with the X-rays with $\alpha = 60°$. The out-of-plane polarization component mainly excites π^* orbitals. Therefore, π^* peaks and components with 30° are larger than those with 60°. In Fig 4.13, from α dependence, I assign the calculated XAS spectra from 285 to 295 eV as π^* states though this range is larger than the observed one (from 285 to 290 eV). Top Ni atoms under carbon σ bonds in the bridge-top structure hybridize with C p_z orbital as well as C $p_{x,y}$ orbitals which form σ bonds. Since σ^* and π^* states merge, this hybridization results the weak π^* peak

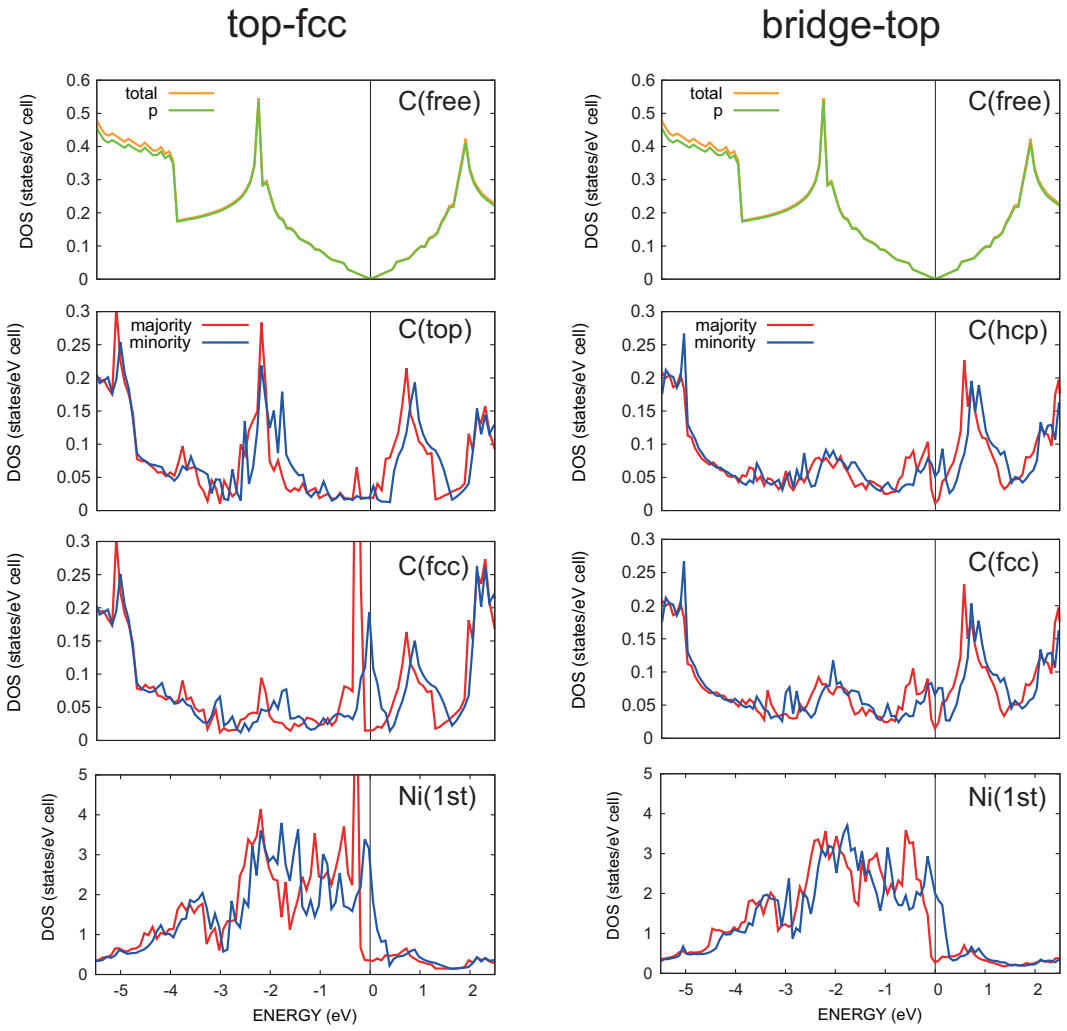

Figure 4.12: The calculated spin-resolved PDOS of the carbon atoms and the first Ni layer in the top-fcc and bridge-top structure. Energies are relative to the Fermi energy. For comparison, the total and p component DOSs of free-standing graphene carbon are also shown.

at about 285 eV, the enhancement of peaks between the π^* and σ^* energy region, and the strong α dependence at 294 eV for the bridge-top structure. On the other hand, this dependence at 294 eV is negligible in the calculated top-fcc spectra. Top Ni atoms in the top-fcc structure is under the C(top) sites, i.e. C(top) p_z and Ni(top) $3d$ orbitals form a strong bonding state as shown by the C(top) PDOS at about -2.5 eV in Fig. 4.12. Note that XAS spectra does not correspond to the PDOS shown in Fig. 4.12 directly because of its absence of a core hole. Furthermore, the large π^* peak in C(fcc) XAS spectra well corresponds to the observed one. For the observed XAS spectra, the α dependence of π^* is large; however changes of the σ^* peak is negligibly small. From these calculated and observed α dependence, I conclude that the top-fcc structure is dominant in graphene/Ni samples which show substantial XMCD intensity. This result consists with the findings from STM images: the ratio of the top-fcc, bridge-top and top-hcp structure is about 65, 22 and 13 % for the reported sample [106]. Although the structural ratio, of course, can be deviated by sample preparing conditions, the majority structure does not change according to reports which determine the graphene-Ni interface distance [97, 99, 100].

The calculated spectra show strong oscillation, indicating the cluster size convergence is not obtained by using at 10 Å cluster radii in spite of the close distance between graphene and Ni surface. This implies that we should use larger clusters ($\sim$ 25 Å indicated by ref. [109]) even if a graphene sheet locates on other compounds for MS calculations. Fortunately, calculated graphene XANES spectra by using FPMS with 10 Å cluster radii showed similar π^* and σ^* peaks to those with 30 Å cluster radii [109], indicating that main spectral features are possessed even for small cluster radii. The major spectral difference for 30 Å cluster radii was the absence of spectral oscillations that are not observed. If a cluster size is not sufficiently large, a photoelectron feels cluster edges or boundaries which behave like walls of a quantum well. Then, unnatural oscillations may be observed in calculated spectra with a small size cluster as some resonant states. While, a strong spectral peak would be attributed to a resonant state, which is less influenced by effects of cluster edges than non resonant states corresponding to flat or smooth parts of spectra. Hence, calculated π^* and σ^* peaks may still survive even if the cluster radius is 10 Å. Compared with calculations by using the MT approximation, the FPMS calculated results for free-standing graphene improved π^* and σ^* peak positions

and fine spectral shapes following above π^* and σ^* peaks. However, the MS calculations with the MT approximation also provide us similar π^* and σ^* peaks to those calculated by using FPMS schemes. Thus, we could discuss XAS and XMCD spectra for graphene on Ni systems at π^* and σ^* peak energy positions by using the calculated results in this thesis.

In Fig. 4.13, the observed XMCD spectra mainly show their intensity at the π^* peak energy, and rippled background. The calculated prominent π^* peak of the XMCD spectra absorbed at the C(fcc) site in the top-fcc structure show good agreement with the observed one. While, one notices calculated XMCD spectral oscillations or dispersion shapes in the π^* energy region absorbed at the other carbon sites, which do not correspond to the observed spectral structure. Thus, the C(fcc) site in the top-fcc structure has a dominant contribution for XMCD spectra of graphene/Ni systems. This can be interpreted by the hybridization of the C(fcc) p_z orbital with Ni(top) d orbitals as shown by the PDOS near the Fermi energy in Fig. 4.12. Since the C(fcc) site locates above the center of the triangle consisted by three Ni(top) sites, the hybridized C(fcc) p_z orbital could borrows Ni $3d_{zx,zy}$ orbital moments which provide the substantial XMCD intensity. For the other carbon sites, the peak energy of the hybridized p_z state deviates from the observed π^* energy dut to their stronger hybridization with Ni $3d$ than the top-fcc C(fcc) one. This results less importance of carbon sites except for the top-fcc C(fcc) for XMCD spectra. XMCD spectra absorbed at the C(hcp) may be similar to those at the C(fcc) because the local geometry of the C(hcp) and C(fcc) sites is similar. However, the configuration ratio of the top-hcp structure is sufficiently lower than that of the top-fcc [106].

To investigate the origin of the calculated XMCD intensity, contribution of the SOI at scattering sites to XMCD spectra is shown in Figure 4.14 with the total calculated spectra. The scattering site SOI and total terms are represented by solid lines and points, respectively. Because their terms are almost perfectly same, contribution of the absorbing atom, i.e. carbon atoms can be neglected. Hence, the calculated XMCD intensity is produced by the SOI at Ni sites. This indicates that the scattering-site SOI has a dominant contribution to light-element XMCD spectra for systems in which absorbing atoms surrounded by TM or heavier magnetic atoms.

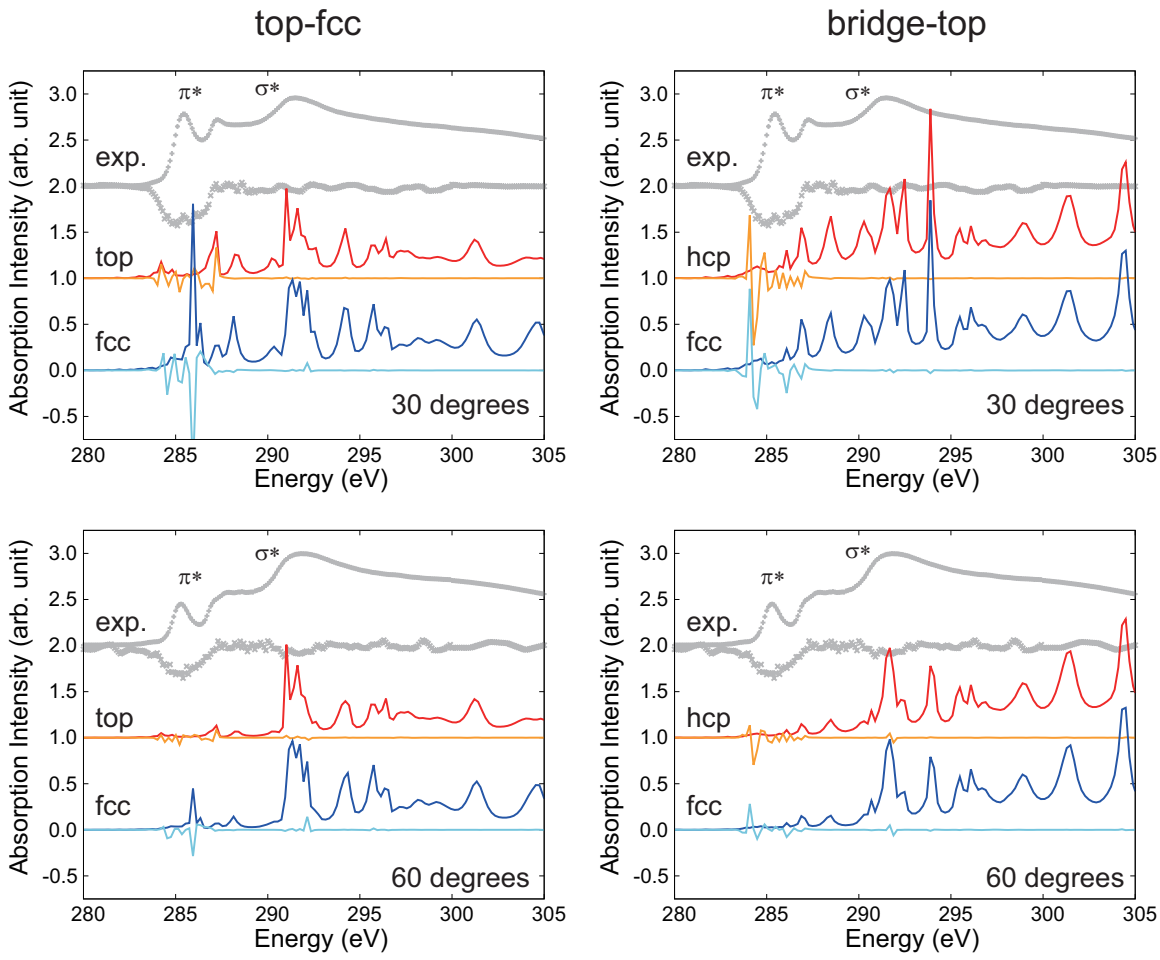

Figure 4.13: The calculated C K-edge XAS and XMCD spectra of graphene on Ni(111) surface systems with the top-fcc and bridge-top structures. Desplayed angles 30 and 60 ° are the incident X-ray angles α relative to the surface as shown in Fig. 4.6. The observed spectra are also shown for comparison [86]. All the XMCD spectra are multiplied by ten.

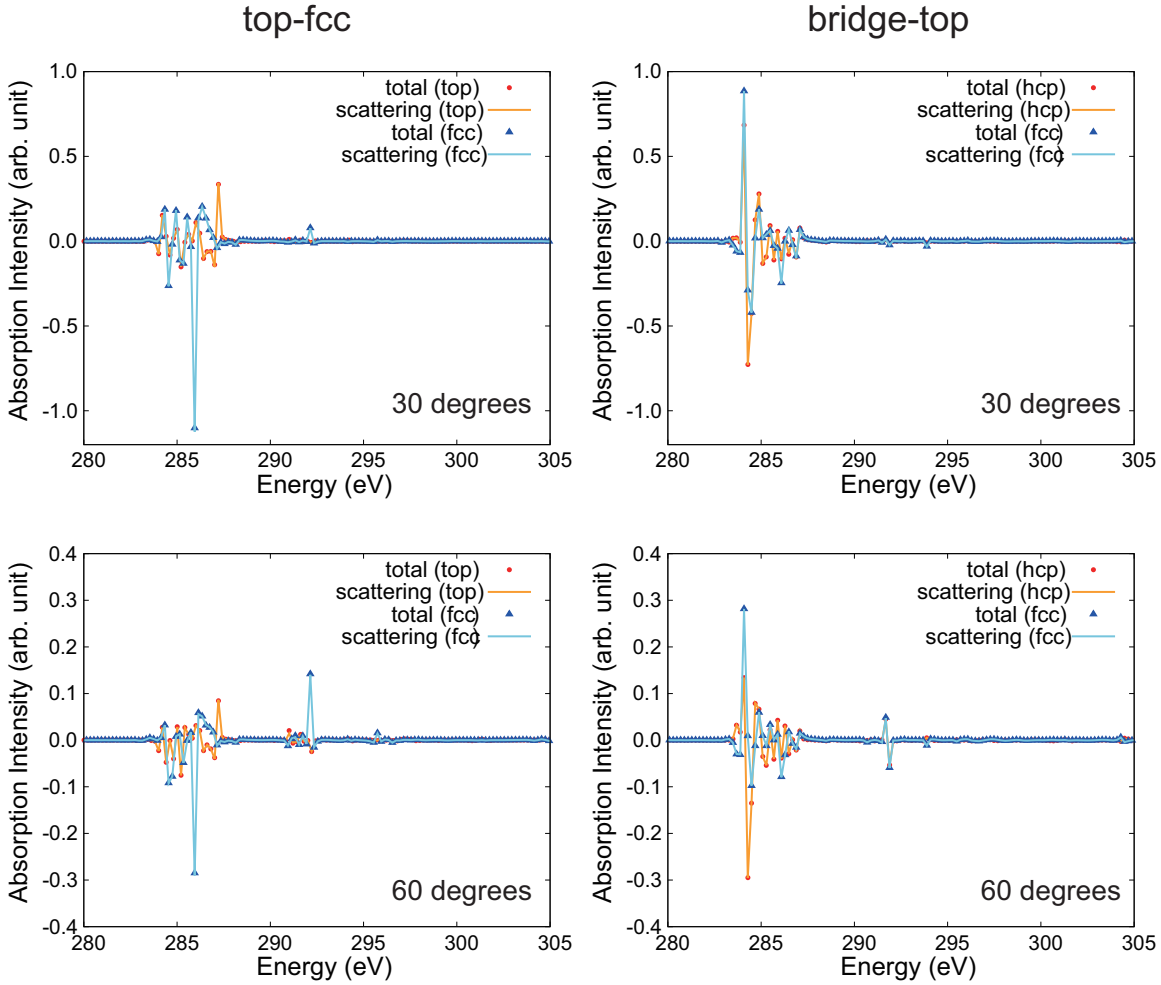

Figure 4.14: The calculated XMCD spectra of total (points) and the scattering SOI term (solid line) for the top-fcc and bridge-top structure with α= 30° and 60°. The spectra are multiplied by ten.

4.5 Conclusion

I derive the XMCD theory including the SOI at scattering sites, which was either neglected or not studied deeply. The scattering-site SOI has substantial contribution to calculated XMCD spectra for not only light atoms adjacent to TM atoms but bulk TM. This is resulted by photoelectron scattering by the SOI and site potential at the same time. On the other hand, the contribution of photoelectron scattering only by the SOI is negligibly small in the same way as the previous result for MEXAFS. The inclusion of the scattering-site SOI improves calculated results of BCC iron though scale factors are still needed to compare the calculated XMCD spectra with the observed ones. For graphene

on Ni surface systems, the SOI at Ni sites yields the calculated C K-edge XMCD intensity. In addition, the absorption at the top-fcc C(fcc) site has dominant contribution to the π^* peak in C K-edge XAS and XMCD spectra. This conclusion is achieved by combining XMCD and PDOS analyses indicating the hybridization of the carbon $2p$ orbital with the Ni $3d$ ones. Therefore, both spectroscopic and electron structural approaches are needed to fully understand complicated systems.

Chapter 5

Conclusion

In this thesis I investigated the applicability of XAS technique for RE doped GaN and a graphene sheet on Ni surface as functional materials which include complicate structures, such as impurities, vacancies, surface, interface, and light and heavy element complexes. To extract information about local structure, I performed theoretical calculations by using a MS theory mainly, and a multiplet theory partially.

RE L_3- and L_1-edge XANES spectra were measured for GaN:RE systems to explore existence of nitrogen vacancies adjacent to doped RE ions. In addition, polarization-dependent measurements were performed for GaN:Dy systems. I observed Dy L_1-edge XANES spectra for GaN:Dy for the first time as far as I know. The prominent pre-edge peak in the L_1-edge spectra indicates non inversion symmetry around doped Dy ion, which has no discrepancy with the Dy ion occupying at a Ga site in GaN. The observed spectra and their polarization dependences are analyzed with structural models which include nitrogen vacancies. As a result, the large displacement of doped RE ions from its occupied lattice site toward space created by nitrogen vacancies is not so prominent. This indicates that the orbital mixing between RE and N, or Ga is substantial, and its bonding characters does not change very much by the vacancies. On the basis of small multiplet effects on XANES spectra of RE nitride, the band effects on XANES spectra of GaN:RE spectra are dominant, indicating the itinerant character of RE d (and of course s) electrons. Moreover, small structural difference of GaN:RE among the RE elements suggests that various doped RE ions could be embedded in GaN without any singular behaviors.

The spectral polarization dependence is quite useful condition to judge which plausible models are reasonable in addition to the spectral structure when we compare observed spectra with calculated ones. This reduces errors of analyses of XANES spectra with *ab-initio* calculations. From the polarization dependence analysis for the Ga-rich GaN:Dy (solid solution phase), I reveal the anisotropy of the nitrogen vacancy position next to doped RE ions: a N^a site is more plausible than the N^c site if the vacancy exists. The N-rich GaN:Dy spectra show smaller polarization dependence than those of the Ga-rich ones, which could be explained by the segregation of RE nitride. It is known that crystals grown under the N-rich condition have lower quality compared with the Ga-rich or stoichiometric condition. Moreover, GaN:RE inherently prefers to dissolve to GaN and RE nitride in terms of the thermodynamic stability. The segregation of RE nitride therefore seems to be reasonable. Note that the N-rich GaN:Dy sample also has the solid solution phase and includes a nitrogen vacancy adjacent to doped Dy ions.

The XRD profile of GaN:RE grown under the N-rich condition shows only a peak assigned to the reflection from a GaN template. Two possibilities lay: the RE doped GaN has the same XRD profiles as GaN, or negligible contribution. The concept of segregated RE nitride could adapt to both the possibilities. The reduction of the amount of RE ions in the solid solution by the segregation shift energies of the GaN:RE peak to GaN template in according to the Vegald's law, and also decrease its intensity. Moreover, the segregation may make the crystal quality of the GaN:RE layer worse, which broadens the XRD peak from the GaN:RE layer. One problem of the concept of the segregation is that there are no report of the segregation of bulk RE nitride crystals by XRD and EXAFS measurements. If RE nitride segregates as nanocrystals, its XRD peaks will be broadened and its EXAFS oscillations suppressed. Then, these would be buried by signals of GaN or the solid solution phase. In contrast, XANES spectra less suffer effects of Debye-Waller factor compared with EXAFS spectra since the photoelectron wavenumber is relatively low. This suggests that the contribution of nanocrystals of RE nitride to XANES spectra would be survive. The volume ratio of RE nitride crystals with respect to total sample layers is roughly estimated less than 0.7 % on the basis of XANES analyses. Note that I neglected anharmonic effects enhanced by the nitrogen vacancy, which would displace the doped RE ion toward the vacancy from its equilibrium position. Since I only measured

the XANES spectra at room temperature, further experiments or theoretical studies are required to consider such vibrational effects.

I also investigated the SOI effect of scattering sites on XMCD spectra within MS theory in which the first order of the SOI as a perturbation is taken into account. The scattering site SOI had not been studied in detail, and considered as negligible in according to the previous report for MEXAFS. I modify the MS XMCD theory to include the scattering-site SOI, and classify it in terms of processes of photoelectron scattering. As a result, I found that the previous MEXAFS calculation neglected the single scattering process in which the photoelectron is influenced by the SOI and site potential at the same time. I confirm that the term neglected before has dominant contributions and improves calculated results by Fe K-edge XMCD calculation. The other MS processes in the same as the important single scattering one also show substantial contribution to the calculated XMCD spectra. This indicates that a site potential enhances the overlap between a photoelectron and the SOI in a atomic sphere. I also calculated C K-edge XMCD spectra of graphene on Ni(111) surface systems to show the importance of surrounding magnetic atoms contributions for XMCD on light elements. I found that graphene on Ni(111) systems still require huge cluster radii ($\sim$ 30 Å) for well converged MS calculations, in spite of their close interlayer distance with respect to the physisorption. However, major spectral features could be discussed by using relatively smaller cluster radii($\sim$ 10 Å). The calculated XAS and XMCD spectra show that the absorption at the C(fcc) site in the top-fcc structure well agree with the observed ones. By dividing the contribution to C K-edge XMCD spectra into the atomic and scattering terms, I reveal that the scattering-site SOI at Ni atoms dominates the calculated XMCD intensity. Combining with PDOS results, I conclude that the hybridization of the top-fcc C(fcc) p_z orbital with the Ni(top) $d_{zx,zy}$ orbitals is essential to yield the observed XMCD spectra. This suggests that XAS and XMCD analyses can be used for the confirmation of the theoretical prediction such as calculated PDOSs. However, for the absorption of light elements, the surrounding atoms such as TM atoms contribution to XMCD spectra should be checked carefully.

Appendix A

Site t-matrix expansion

The total T-matrix describes the infinite scattering by the total potential.

$$T = V + Vg_0T = V + Vg_0V + Vg_0Vg_0V + Vg_0Vg_0Vg_0V + \cdots$$

We assume that the total potential $V(\mathbf{r})$ can be represeted by the summation of each site potential $v_i(\mathbf{r}_i)$ ($\mathbf{r}_i = \mathbf{r} - \mathbf{R}_\imath$).

$$V(\mathbf{r}) = \sum_i v_i(\mathbf{r}_i),$$
$$T = \sum_i v_i + \sum_{ij} v_i g_0 v_j + \sum_{ijk} v_i g_0 v_j g_0 v_k + \cdots .$$

The indice *i, j, k* in the summation include same sites. The site t-matrix t_α at α site is defined by

$$t_\alpha = v_\alpha + v_\alpha g_0 v_\alpha + v_\alpha g_0 v_\alpha g_0 v_\alpha + \cdots = v_\alpha + v_\alpha g_0 t_\alpha.$$

To show the site t-matrix expansion, we define some tools as follows:

$$\alpha = \sum_\alpha v_\alpha \ , \qquad \alpha\alpha = \sum_\alpha v_\alpha g_0 v_\alpha \ , \qquad \alpha\beta = \sum_{\alpha\neq\beta} v_\alpha g_0 v_\beta = \beta\alpha,$$
$$\alpha\beta\beta = \sum_{\alpha\neq\beta} v_\alpha g_0 v_\beta g_0 v_\beta = \beta\alpha\alpha \ , \qquad \alpha\beta\gamma = \sum_{\alpha\neq\beta\neq\gamma} v_\alpha g_0 v_\beta g_0 v_\gamma,$$
$$\alpha\beta\alpha' = \sum_{\alpha\alpha'} \sum_{\beta(\neq\alpha,\alpha')} v_\alpha g_0 v_\beta v_{\alpha'} = \alpha\beta\alpha + \alpha\beta\gamma = \alpha\beta(\alpha+\gamma).$$

The same characters indicate to take same summation, while the different characters mean individual summations with no same indice. The relation between with and without prime

is individual summations allowed to take same indice. This rule is adopted for higher oreder characters. When we consider the terms in the total T-matrix up to the forth order of V,

$$\begin{aligned}
\sum_i v_i &= \alpha, \\
\sum_{ij} v_i g_0 v_j &= \alpha\alpha + \alpha\beta \ (= \alpha\alpha'), \\
\sum_{ijk} v_i g_0 v_j g_0 v_k &= \alpha\alpha\alpha + \alpha\beta\gamma + (\alpha\alpha\beta + \alpha\beta\alpha + \alpha\beta\beta) \\
&= \alpha\alpha\alpha + (\alpha\alpha\beta + \alpha\beta\beta) + \alpha\beta\alpha', \\
\sum_{ijkl} v_i g_0 v_j g_0 v_k g_0 v_l &= \alpha\alpha\alpha\alpha + \alpha\beta\gamma\delta + (\alpha\alpha\alpha\beta + \alpha\alpha\beta\alpha + \alpha\beta\alpha\alpha + \alpha\beta\beta\beta) \\
&\quad + (\alpha\alpha\beta\beta + \alpha\beta\beta\alpha + \alpha\beta\alpha\beta) \\
&\quad + (\alpha\beta\gamma\gamma + \alpha\beta\beta\gamma + \alpha\alpha\beta\gamma + \alpha\beta\gamma\beta + \alpha\beta\alpha\gamma + \alpha\beta\gamma\alpha) \\
&= \alpha\alpha\alpha\alpha + (\alpha\alpha\alpha\beta + \alpha\beta\beta\beta + \alpha\alpha\beta\beta) \\
&\quad + (\alpha\alpha\beta\alpha' + \alpha\beta\alpha'\alpha' + \alpha\beta\beta\alpha') + \alpha\beta\alpha'\bar{\alpha}',
\end{aligned}$$

where

$$\alpha\beta\alpha'\bar{\alpha}' = \alpha\beta\gamma(\alpha + \beta + \delta) + \alpha\beta\alpha(\beta + \gamma).$$

The charater $\bar{\alpha}'$ include same sites with α and β but not with α'. We therefore obtain the T-matrix up to the forth order.

$$\begin{aligned}
T^{(4)} &= \{\alpha + \alpha\alpha + \alpha\alpha\alpha + \alpha\alpha\alpha\alpha\} + \{(\alpha + \alpha\alpha)(\beta + \beta\beta) + \alpha\alpha\alpha\beta + \alpha\beta\beta\beta\} \\
&\quad + \{\alpha\beta\alpha' + \alpha\alpha\beta\alpha' + \alpha\beta\alpha'\alpha' + \alpha\beta\beta\alpha'\} + \{\alpha\beta\alpha'\bar{\alpha}'\}
\end{aligned}$$

This represetation is expanded to the infinite order.

$$\begin{aligned}
T &= (\alpha + \alpha\alpha + \cdots) + (\alpha + \alpha\alpha + \cdots)(\beta + \beta\beta + \cdots) \\
&\quad + (\alpha + \alpha\alpha + \cdots)(\beta + \beta\beta + \cdots)(\alpha' + \alpha'\alpha' + \cdots) \\
&\quad + (\alpha + \alpha\alpha + \cdots)(\beta + \beta\beta + \cdots)(\alpha' + \alpha'\alpha' + \cdots)(\bar{\alpha}' + \bar{\alpha}'\bar{\alpha}' + \cdots) + \cdots \\
&= \sum_\alpha t_\alpha + \sum_\alpha t_\alpha g_0 \sum_{\beta(\neq\alpha)} t_\beta + \sum_\alpha t_\alpha g_0 \sum_{\beta(\neq\alpha)} t_\beta g_0 \sum_{\alpha'(\neq\beta)} t_{\alpha'} \\
&\qquad + \sum_\alpha t_\alpha g_0 \sum_{\beta(\neq\alpha)} t_\beta g_0 \sum_{\alpha'(\neq\beta)} t_{\alpha'} g_0 \sum_{\bar{\alpha}'(\neq\alpha')} t_{\bar{\alpha}'} + \cdots .
\end{aligned}$$

The total T-matrix is expressed by the site t-matrix t describing inner-atomic infinite scattering and the free propagator g_0 between different sites.

Appendix B

Spin-orbit interaction

The Pauli matrix σ has the relationship between arbitrary vectors $\mathbf{A}$ and $\mathbf{B}$.

$$(\sigma \cdot \mathbf{A})(\sigma \cdot \mathbf{B}) = \mathbf{A} \cdot \mathbf{B} + i\sigma \cdot (\mathbf{A} \times \mathbf{B}) \tag{B.1}$$

By using this relation, $Q(V - \varepsilon)Q$ in eq. (2.14d) becomes:

$$Q = \frac{\sigma \cdot \mathbf{p}}{2c}, \tag{B.2}$$

$$\mathbf{p} = -i\nabla, \tag{B.3}$$

$$Q(V - \varepsilon)Q = \frac{1}{4c^2}\{(\sigma \cdot \mathbf{p})V(\sigma \cdot \mathbf{p}) - \varepsilon(\sigma \cdot \mathbf{p})^2\} = \frac{1}{4c^2}\{(\sigma \cdot \mathbf{p})V(\sigma \cdot \mathbf{p}) - \varepsilon p^2\} \tag{B.4}$$

$$= -\frac{1}{4c^2}\{(\sigma \cdot \nabla)V(\sigma \cdot \nabla) - \varepsilon\nabla^2\} \tag{B.5}$$

$$= -\frac{1}{4c^2}\{(\sigma \cdot \nabla V)(\sigma \cdot \nabla) + V(\sigma \cdot \nabla)^2 - \varepsilon\nabla^2\} \tag{B.6}$$

$$= -\frac{1}{4c^2}\{\nabla V \cdot \nabla + i\sigma \cdot (\nabla V \times \nabla) + V\nabla^2 - \varepsilon\nabla^2\} \tag{B.7}$$

$$= -\frac{1}{4c^2}\{\nabla V \cdot \nabla + (V - \varepsilon)\nabla^2\} + \frac{1}{4c^2}\sigma \cdot (\nabla V \times (-i\nabla)) \tag{B.8}$$

$$= -\frac{1}{4c^2}\{\nabla V \cdot \nabla + (V - \varepsilon)\nabla^2\} + \frac{1}{4c^2}\sigma \cdot (\nabla V \times \mathbf{p}). \tag{B.9}$$

We assume the total potential V as superposition of spherical (muffin-tin) site potential v.

$$\nabla V(\mathbf{r}) = \sum_\alpha \nabla v_\alpha(r_\alpha) = \sum_\alpha \nabla_\alpha v_\alpha(r_\alpha) = \sum_\alpha \frac{1}{r_\alpha}\frac{dv(r_\alpha)}{dr_\alpha}\mathbf{r}_\alpha, \tag{B.10}$$

$$\frac{1}{4c^2}\nabla V(r)\times\mathbf{p} = \frac{1}{4c^2}\sum_\alpha \frac{1}{r_\alpha}\frac{dv_\alpha(r_\alpha)}{dr_\alpha}\mathbf{r}_\alpha\times\mathbf{p}_\alpha = \frac{1}{4c^2}\sum_\alpha \frac{1}{r_\alpha}\frac{dv_\alpha(r_\alpha)}{dr_\alpha}\mathbf{L}_\alpha \tag{B.11}$$

$$= \sum_\alpha \xi_\alpha(r_\alpha)\mathbf{L}_\alpha, \tag{B.12}$$

$$\xi(r) \equiv \frac{1}{4c^2}\frac{1}{r}\frac{dv(r)}{dr}. \tag{B.13}$$

The last term of $Q(V-\varepsilon)Q$ describes the spin-orbit interaction. The other terms are not important for XMCD intensity.

$$Q(V-\varepsilon)Q \;\sim\; \sum_\alpha \xi_\alpha \sigma\cdot\mathbf{L}^\alpha = \sum_\alpha \delta v_\alpha, \tag{B.14}$$

$$\delta v_\alpha \equiv\; \xi_\alpha\sigma\cdot\mathbf{L}^\alpha = \xi_\alpha \begin{pmatrix} L_z^\alpha & L_-^\alpha \\ L_+^\alpha & -L_z^\alpha \end{pmatrix}, \tag{B.15}$$

Strictly, the site potential is 2×2 matrix in spinor representation. In the present thesis, the potential v is assumed diagonal in the spin space.

$$v_\alpha = \begin{pmatrix} v_\alpha^+ & 0 \\ 0 & v_\alpha^- \end{pmatrix}, \qquad \xi_\alpha = \begin{pmatrix} \xi_\alpha^+ & 0 \\ 0 & \xi_\alpha^- \end{pmatrix}, \qquad \delta v_\alpha = \begin{pmatrix} \xi_\alpha^+ L_z^\alpha & \xi_\alpha^+ L_-^\alpha \\ \xi_\alpha^- L_+^\alpha & -\xi_\alpha^- L_z^\alpha \end{pmatrix} \tag{B.16}$$

In addition, the operator Q has another representation multiplied by $(\sigma\cdot\mathbf{r})$.

$$Q(\sigma\cdot\mathbf{r}) = \frac{1}{2c}(\sigma\cdot\mathbf{p})(\sigma\cdot\mathbf{r}) = \frac{1}{2c}\left((\mathbf{p}\cdot\mathbf{r}) + i\sigma\cdot(\mathbf{p}\times\mathbf{r})\right) \tag{B.17}$$

$$= \frac{1}{2c}\left(-3i + (\mathbf{r}\cdot\mathbf{p}) - i\sigma\cdot(\mathbf{r}\times\mathbf{p})\right) \tag{B.18}$$

$$= \frac{1}{2c}\left(-3i + (\mathbf{r}\cdot\mathbf{p}) - i\sigma\cdot\mathbf{L}\right) \tag{B.19}$$

Only the last term contributes to XMCD intensity. Then,

$$Q(\sigma\cdot\mathbf{r}) \;\sim\; -\frac{i}{2c}\sigma\cdot\mathbf{L}. \tag{B.20}$$

This relation is important for the XMCD intensity from T_{12} and T_{21}, which include the small compotent χ_c.

Appendix C

Expansion of g with g_A and/or g_B

The propagator g_A includes the infinite inner scattering at the A site, respectively.

$$g_A = g_0 + g_0 t_A g_0 = g_0 + g_0 v_A g_0 + g_0 v_A g_0 v_A g_0 + \cdots$$

By using these propagator and the site T-matrix expansion, the full propagator g involved the infinite scattering by the total potential V becomes:

$$\begin{aligned}
g &= g_0 + g_0 V g = g_0 + g_0 \sum_\alpha v_\alpha g = g_0 + g_0 T g_0 \left(\neq g_0 + g_0 \sum_\alpha t_\alpha g_0 \right) \\
&= g_0 + g_0 \sum_\alpha t_\alpha g_0 + g_0 \sum_{\beta(\neq\alpha)} t_\beta g_0 \sum_\alpha t_\alpha g_0 + g_0 \sum_{\gamma(\neq\beta)} t_\gamma g_0 \sum_{\beta(\neq\alpha)} t_\beta g_0 \sum_\alpha t_\alpha g_0 + \cdots \\
&= g_0 + \left(g_0 t_A g_0 + g_0 \sum_{\alpha(\neq A)} t_\alpha g_0 \right) + \left(g_0 \sum_{\beta(\neq A)} t_\beta g_0 t_A g_0 + g_0 \sum_{\beta(\neq\alpha)} t_\beta g_0 \sum_{\alpha(\neq A)} t_\alpha g_0 \right) \\
&\qquad + \left(g_0 \sum_{\gamma(\neq\beta)} t_\gamma g_0 \sum_{\beta(\neq A)} t_\beta g_0 t_A g_0 + g_0 \sum_{\gamma(\neq\beta)} t_\gamma g_0 \sum_{\beta(\neq\alpha)} t_\beta g_0 \sum_{\alpha(\neq A)} t_\alpha g_0 \right) + \cdots \\
&= (g_0 + g_0 t_A g_0) + g_0 \sum_{\alpha(\neq A)} t_\alpha (g_0 + g_0 t_A g_0) + g_0 \sum_{\beta(\neq\alpha)} t_\beta g_0 \sum_{\alpha(\neq A)} t_\alpha (g_0 + g_0 t_A g_0) + \cdots \\
&= g_A + g_0 \sum_{\alpha(\neq A)} t_\alpha g_A + g_0 \sum_{\beta(\neq\alpha)} t_\beta g_0 \sum_{\alpha(\neq A)} t_\alpha g_A + \cdots ,
\end{aligned} \tag{C.1}$$

or

$$g = g_A + g_A \sum_{\alpha(\neq A)} t_\alpha g_0 + g_A \sum_{\beta(\neq A)} t_\beta g_0 \sum_{\alpha(\neq\beta)} t_\alpha g_0 + \cdots . \tag{C.2}$$

These expansions terminated by g_0 and g_A is useful for photoemission phenomena. For

X-ray absorption spectra, we terminate each side of g by g_A and/or g_B.

$$\begin{aligned} g &= g_A + g_0 \sum_{\alpha(\neq A)} t_\alpha g_A + g_0 \sum_{\beta(\neq\alpha)} t_\beta g_0 \sum_{\alpha(\neq A)} t_\alpha g_A + \cdots \\ &= g_A + \left(g_0 t_B g_A + g_0 \sum_{\alpha(\neq A,B)} t_\alpha g_A \right) \\ &\qquad + \left(g_0 t_B g_0 \sum_{\alpha(\neq A,B)} t_\alpha g_A + g_0 \sum_{\beta(\neq\alpha,B)} t_\beta g_0 \sum_{\alpha(\neq A)} t_\alpha g_A \right) + \cdots \\ &= g_A + g_0 t_B g_A (1 - \delta_{AB}) + (g_0 + g_0 t_B g_0) \sum_{\alpha(\neq A,B)} t_\alpha g_A \\ &\qquad + (g_0 + g_0 t_B g_0) \sum_{\beta(\neq\alpha,B)} t_\beta g_0 \sum_{\alpha(\neq A)} t_\alpha g_A + \cdots . \end{aligned} \tag{C.3}$$

Therefore, we obtained the expansion of g propargating from A to B.

$$g = g_A + g_B v_B g_A (1 - \delta_{AB}) + g_B \sum_{\alpha(\neq A,B)} t_\alpha g_A + g_B \sum_{\beta(\neq\alpha,B)} t_\beta g_0 \sum_{\alpha(\neq A)} t_\alpha g_A + \cdots \tag{C.4}$$

$$= g_A + g_A v_B g_B (1 - \delta_{AB}) + g_A \sum_{\alpha(\neq A,B)} t_\alpha g_B + g_A \sum_{\beta(\neq\alpha,A)} t_\beta g_0 \sum_{\alpha(\neq B)} t_\alpha g_B + \cdots , \tag{C.5}$$

where

$$\begin{aligned} g_0 t_B g_A &= g_0 v_B g_A + g_0 v_B g_0 v_B g_A + \cdots = (g_0 + g_0 v_B g_0 + \cdots)\, v_B g_A \\ &= g_B v_B g_A \end{aligned} \tag{C.6}$$

These expansion with $A \neq B$ is useful to calculate XMCD intensity arisen from the SOI on scatterer sites. When we calculate XANES spectra, the expansion with $A = B$ is only needed.

$$g = g_A + g_A \sum_{\alpha(\neq A)} t_\alpha g_A + g_A \sum_{\beta(\neq\alpha,A)} t_\beta g_0 \sum_{\alpha(\neq A)} t_\alpha g_A + \cdots . \tag{C.7}$$

Reference

[1] A typical Fe K-edge XAFS spectrum is obtained from XAFS database presented by Institute for Catalysis, Hokkaido University. http://133.50.165.193/catdb/

[2] M. Oishi, T. Fujimoto, Y. Takanashi, Y. Orikasa, A. Kawamura, T. Ina, H. Yamashige, D. Takamatsu, K. Sato, H. Murayama, H. Tanida, H. Arai, H. Ishii, C. Yogi, I. Watanabe, T. Ohta, A. Mineshige, Y. Uchimoto and Z. Ogumi, J. Power Source 222 (2013) 45.

[3] Z. Bayindir, P.N. Duchesne, S.C. Cook, M.A. MacDonald and P. Zhang, J. Chem. Phys. **131** (2009) 244716.

[4] B.K. Teo: *EXAFS: Basic Principles and Data Analysis*, eds. C.K. Jørgensen, M.F. Lappert, S.J. Lippard, J.L. Margrave, K. Niedenzu, H. Nöth, R.W. Parry and Hideo Yamata (Springer-Verlag, Berlin 1986), pp181.

[5] G. Bunker: *Introdcution to XAFS: a practical guide to X-ray absorption fine structure Spectroscopy* (Cambridge University Press, Cambridge, 2010) pp37-39.

[6] A.L. Ankudinov, J.J. Rehr, Phys. Rev. B **51** (1995) 1282.

[7] C.T. Chen, Y.U. Idzerda, H.-J. Lin, N.V. Smith, G. Meigs, E. Chaban, G.H. Ho, E. Pellegrin and F. Sette, Phys. Rev. Lett. **75** (1995) 152.

[8] J. Igarashi and K. Hirai, Phys. Rev. B **50** (1994) 17820.

[9] B.T. Thole, P. Carra, F. Sette and G. van der Laan, Phys. Rev. Lett. **68** (1992) 1943.

[10] P. Carra, B.T. Thole, M. Altarelli and X. Wang, Phys. Rev. Lett. **70** (1993) 694.

[11] J.J. Rehr and R.C. Albers, Rev. Mod. Phys. **72** (2000) 621.

[12] A. Koide, T. Fujikawa and N. Ichikuni J. Electron Spectrosc. Relat. Phenom. **195** (2014) 375.

[13] F.M.F. de Groot, J. Electron Spectrosc. Relat. Phenom. **67** (1994) 529.

[14] F.M.F. de Groot, Chem. Rev. **101** (2001) 1779.

[15] F.M.F. de Groot, Coord. Chem. Rev. **249** (2005) 31.

[16] P. Krüger and C.R. Natoli, Phys. Rev. B **70** (2004) 245120.

[17] P. Krüger, Phys. Rev. B **81** (2010) 125121.

[18] K. Hatada, K. Hayakawa, M. Benfatto and C.R. Natoli, Phys. Rev. B **88** (2007) 060102(R).

[19] K. Hatada, K. Hayakawa, M. Benfatto and C.R. Natoli, J. Phys: Condens. Matter **21** (2010) 104206.

[20] K. Hatada, K. Hayakawa, M. Benfatto and C.R. Natoli, J. Phys: Condens. Matter **22** (2010) 185501.

[21] T. Fujikawa and S. Nagamatsu J. Electron Spectrosc. Relat. Phenom. **129** (2003) 55.

[22] A. Koide, D. Abe, S. Emura and T. Fujikawa, e-J. Surf. Sci. Nanotech. **10** (2012) 661.

[23] T. Fujikawa and S. Nagamatsu, Jpn. J. Appl. Phys. **41** (2002) 2005.

[24] T. Fujikawa and I. Hojo, In: Circular Dichroism: Theory and Spectroscopy, Editor: David S. Rodgers, (Nova Science Publisher, New York, 2011) pp. 1-81.

[25] C. Brouder and Muhammad Hikam, Phys. Rev. B **43** (1991) 3809.

[26] C. Brouder, M. Alouani and K. H. Bennemann, Phys. Rev. B **54** (1996) 7334.

[27] A.L. Ankudinov, B. Ravel, J.J. Rehr and S.D. Conradson, Phys. Rev. B **58** (1998) 7565.

[28] A.L. Ankudinov, C.E. Bouldin, J.J. Rehr, J. Sims and H. Hung, Phys. Rev. B **65** (2002) 104107.

[29] F. Gesztesy, H. Grosse and B. Thaller, Ann. Inst. Henri. Poincaré **40** (1984) 159.

[30] A.L. Ankudinov, A.I. Nesvizhskii and J.J. Rehr, Phys. Rev. B **67** (2003) 115120.

[31] T. Fujikawa and H. Arai, AIP Conf. Proc. **882** (2007) 75.

[32] T. Fujikawa, J. Phys. Conf. Ser. **190** (2009) 012014.

[33] W. B. Fowler, Physics of Color Centers, edited by W. B. Fowler, Academic Press (New York and London), 1968.

[34] N. Mizuochi, T. Makino, H. Kato, D. Takeuchi, M. Ogura, H. Okushi, M. Nothaft, P. Neumann, A. Gali, F. Jelezko, J. Wrachtrup an S. Yamasaki, Nature Photonics **6** (2012) 299.

[35] N. Teraguchi, A. Suzuki, Y. Nanishi, Y.-K. Zhou, M. Hashimoto and H. Asahi, Solid State Commun. **122** (2002) 651.

[36] S. Dhar, O. Brandt, M. Ramsteiner, V.F. Sapega, and K.H. Ploog, Phys. Rev. Lett. **94** (2005) 037205.

[37] S. Dhar, T. Kammermeier, A. Ney, L. Prez, K. H. Ploog, A. Melnikov and A.D. Wieck, Appl. Phys. Lett. **89** (2006) 112504.

[38] Y. Gohda and A. Oshiyama, Phys. Rev. B **78** (2008) 161201(R).

[39] L. Liu, P.Y. Yu, Z. Ma and S.S. Mao, Phys. Rev. Lett. **100** (2008) 127203.

[40] C. Mitra and W.R.L. Lambrecht Phys. Rev. B **80** (2009) 081202(R).

[41] A. Ney, T. Kammermeier, K. ollefs, V. Ney, S. Ye, S. Dhar, K. H. Ploog, M. Röver, J. Malindretos, A. Rizzi, F. Wilhelm and A. Rogalev, J. Mag. Mag. Mat. **322** (2010) 1162.

[42] T. Kammermeler, S. Dhar, V. Ney, E. Manuel, A. Ney, K.H. Ploog, F.-Y. Lo, A. Melnkov and A.D. Wleck, Phys. Stat. Sol. (a) **8** (2008) 1872.

[43] Y. Nakatani, Y. K. Zhou, M. Sato, S. Emura, S. Hasegawa and H. Asahi, e-J. Surf. Sci. Nanotech. **10** (2012) 499.

[44] M. Sano, Y.K. Zhou, S. Emura, S. Hasegawa, and H. Asahi, J. Cryst. Growth **378** (2013) 137.

[45] Y.K. Zhou, M. Takahashi, S. Emura, S. Hasegawa and H. Asahi, J. Supercond. Nov. Magn. **23** (2010) 103.

[46] Y. Hashimoto, H. Amano, Y. Iye and S. Katsumoto, Appl. Phys. Express **4** (2011) 063004.

[47] L. Vegard, Z. Phys. **5** (1921) 17.

[48] J.C. Mikkelsen, Jr. and J.B. Boyce, Phys. Rev. B **28** (1983) 7130.

[49] M. Roever, J. Malindretos, A. Bedoya-Pinto and A. Rizzi, Phys. Rev. B **84** (2011) 081201(R).

[50] F. Tuomisto, J. Phys. Conf. Ser. **265** (2011) 012003.

[51] M. Hashimoto, S. Emura, R. Asano, H. Tanaka, N. Teraguchi, A. Suzuki, Y. Nanishi, T. Honma, N. Umesaki and H. Asahi, Phys. Stat. Sol. (c) **0** (2003) 2650.

[52] M. Azeem, B.J. Ruck, Binh Do Le, H. Warning, H.J. Trodahl, N.M. Strickland, A. Koo, V. Goian and S. Kamba, J. Appl. Phys. **113** (2013) 203509.

[53] K. Khazen, H.J. von Bardeleben, J.L. Cantin, A. Bittar, S. Granville, H.J. Trodahl and B.J. Ruck, Phys. Rev. B **74** (2006) 245330.

[54] G. Martínez-Criado, O. Sancho-Juan, N. Garro, J.A. Sans, A. Cantarero, J. Susini, M. Roever, D.-D. Mai, A. Bedoya-Pinto, J. Malindretos and A. Rizzi, Appl. Phys. Lett. **93** (2008) 021916.

[55] A. Ney, T. Kammermeier, E. Manuel and V. Ney, S. Dhar, K. H. Ploog, F. Wilhelm and A. Rogalev, Appl. Phys. Lett. **90** (2007) 252515.

[56] G. Mountjoy, J.M. Cole, T. Brennan, R.J. Newport, G.A. Saunders and G.W. Wallidge, J. Non-Cryst. Solids **279** (2001) 20.

[57] M.W. Haverkort, M. Zwierzycki and O.K. Andersen, Phys. Rev. B **85** (2012) 165113.

[58] J.A. Bearden and A.F. Burr, Rev. Mod. Phys. **39** (1967) 125.

[59] J.A. Bearden, Rev. Mod. Phys. **39** (1967) 78.

[60] F. Leuenberger, A. Parge, W. Felsch, K. Baudelet, C. Giorgetti, E. Dartyge and F. Wilhelm, Phys. Rev. B **73** (2006) 214430.

[61] H. Yamada, T. Fukawa, T. Muro, Y. Tanaka, S. Imada, S. Suga and T. Suzuki, J. Phys. Soc. Jpn. **65** (1996) 1000.

[62] C.-G. Duan, R.F. Sabirianov, W.N. Mei, P.A. Dowben, S.S. Jaswal and E.Y. Tsymbal, J. Phys.: Condens. Matter **19** (2007) 315220.

[63] E. Stavitski and F.M.F. de Groot, Micron **41** (2010) 687.

[64] MCDFGME, a MultiConfigulation Dirac Fock and General Matrix Elements program, release 2005, written by J.P. Desclaux and P. Indelicato (http://dirac.spectro.jussieu.fr/mcdf)

[65] M.O. Krause and J.H. Oliver, J. Phys. Chem. Ref. Data **8** (1979) 329.

[66] F. Leuenberger, A. Parge, W. Felsch, K. Fauth and M. Hessler, Phys. Rev. B **72** (2005) 014427.

[67] C.M. Balkas, C. Basceri and R.F. Davis, Powder Diffraction **10** (1995) 266.

[68] W. Paszkowicz, S. Podsiadło and R. Minikayev, J. Alloys Compd. **382** (2004) 100.

[69] T. A. Nugraha, K. Shirai and T. Oguchi, unpublished.

[70] J. E. Hahn, R.A. Scott, K.O. Hodgson, S. Doniach, S.R. Desjardins and E. I. Solomon, Chem. Phys. Lett. **88** (1982) 595.

[71] K. Asakura, M. Nomura and H. Kuroda, Bull. Chem. Soc. Jpn. **58** (1985) 1543.

[72] N. Kosugi, T. Yokoyama, K. Asakura, H. Kuroda, Chem. Phys. **91** (1984) 249.

[73] N. Kosugi, H. Kondoh, H. Tajima and H. Kuroda, Chem. Phys. **135** (1989) 149.

[74] T. Yokoyama, N. Kosugi, H. Kuroda, Chem. Phys. **103** (1986) 101.

[75] K.T. Jacob and G. Rajitha, J. Cryst. Growth **311** (2009) 3806.

[76] A.M. Mulokozi, J. Less-Common Met. **80** (1981) 235.

[77] M. Almokhtar, S. Emura, A. Koide, T. Fujikawa and H. Asahi, J. Alloys Compd. **628** (2015) 401.

[78] F. Baudelet, S. Pascarelli, O. Mathon, J.P. Itié, A. Polian, M. d'Astuto and J.C. Chervin, J. Phys.: Condens. Matter **17** (2005) S957.

[79] O. Mathon, F. Baudelet, J.-P. Itié, S. Pasternak, A. Polian and S. Pascarelli, J. Synchrotron Rad. **11** (2004) 423.

[80] R. Torchio, S. Pascarelli, O. Mathon, C. Marini, S. Anzellini, P. Centomo, C. Meneghini, S. Mobilio, N.A. Morley and M.R.J. Gibbs, High Pressure Res. **31**, (2011) 148.

[81] E. Goering, A. Bayer, S. Gold, G. Schütz, M. Rabe, U. Rüdiger and G. Güntherodt, Europhys. Lett. **58** (2002) Europhys. Lett. 906.

[82] C. Sorg, N. Ponpandian, A. Scherz, H. Wende, R. Nünthel, T. Gleitsmann and K. Baberschke, Surf. Sci. **565** (2004) 197.

[83] C. Sorg, N. Ponpandian, M. Barnien, K. Baberschke and H. Wende, Phys. Rev. B **73** (2006) 064409.

[84] C. Sorg, N. Ponpadian, J. Luo, R.Q. Wu, M. Bernien, K. Baberschke and H. Wende, AIP Conf. Proc. **882** (2007) 541.

[85] V.N. Antonov, B.N¿ Harmon, A.N. Yaresko and A.P. Shpak, Phys. Rev. B **75** (2007) 184422.

[86] Y. Matsumoto, S. Entani, A. Koide, M. Ohotomo, P.V. Avramov, H. Naramoto, K. Amemiya, T. Fujikawa and S. Sakai, J. Mater. Chem. C **1** (2013) 5533.

[87] J.J. Rehr, J. J. Kas, F. D. Vila, M. P. Prange and K. Jorissen, Phys. Chem. Chem Phys. **12** (2010) 5503.

[88] H. Ebert, D. Ködderitzsch and J Minár, Rep. Prog. Phys. **74** (2011) 096501.

[89] Y. Joly, S.D. Martteo and C.R. Natoli, Phys. Rev. B **69** (2004) 224401.

[90] O.K. Andersen, Phys. Rev. B **12** (1975) 3060.

[91] O.K. Andersen and O. Jepsen, Phys. Rev. Lett. **53** (1984) 2571.

[92] U. von Barth and L. Hedin, J. Phys. C: Solid State Phys. **5** (1972) 1629.

[93] L. Hedin and B.I. Lundqvist, J. Phys. C: Solid St. Phys. **4** (1971) 2064.

[94] H. Danan, A. Herr and A.J.P. Meyer, J. Appl. Phys. **39** (1968) 669.

[95] V.M. Karpan, G. Giovannetti, P.A. Khomyakov, M. Talanana, A.A. Starikov, M. Zwierzycki, J. van den Brink, G. Brocks and P.J. Kelly, Phys. Rev. Lett. **99** (2007) 176602.

[96] W. Han, K.M. McCreary, K. Pi. W.H. Wang, Y. Li, H. Wen, J.R. Chen and R.K. Kawakami, J. Magn. Magn. Mater. **324** (2012) 369.

[97] D.E. Parreiras, E.A. Soares, G.J.P. Abreu, T.E.P. Bueno, W.P. Fernandes, V.E. de Carvalho, S.S. Carara, H. Chacham and R. Paniago, Phys. Rev. B **90** (2014) 155454.

[98] M. Weser, Y. Rehder, K. Horn, M. Sicot, M. Fonin, A.B. Preobrajenski, E.N. Voloshina, E. Goering and Y. S. Dedkov, Appl. Phys. Lett. **96** (2010) 012504.

[99] Y. Gamo, A. Nagashima, M. Wakabayashi, M. Terai, C. Oshima, Sur. Sci. **374** (1997) 61.

[100] H. Kawanowa, H. Ozawa, T. Yazaki, Y. Gotoh and R. Souda, Jpn. J. Appl. Phys. **41** (2002) 6149.

[101] G. Giovanneti, P.A. Khomyakov, G. Brocks, V.M. Karpan, J. van den Brink and P.J. Kelly, Phys. Rev. Lett. **101** (2008) 026803.

[102] J.S. Gibson, J. Uddin, T.R. Cundari, N.K. Bodiford and A.K. Wilson, J. Phys.: Condens. Matter. **22** (2010) 445503.

[103] G. Bertoni, L. Calmels, A. Altibelli and V. Serin, Phys. Rev. B **71** (2004) 075402.

[104] M. Fuentes-Cabrera, M.I. Baskes, A.V. Melechiko and M.L. Simpson, Phys. Rev. B **77** (2008) 035405.

[105] S. Entani, M. Kurahashi, X. Sun and Y. Yamauchi, Carbon **61** (2013) 134.

[106] F. Bianchini, L.L. Patera, M. Peressi, C. Africh and G. Comelli, J. Phys. Chem. Lett. **5** (2014) 467.

[107] P.L. Silvestrelli and and A. Ambrosetti, Phys. Rev. B **91** (2015) 195405.

[108] W. Zhao, S.K. Kozlov, O. Höfert, K. Gotterbarm, M.P.A. Lorenz, F. Viñes, C. Papp, A. Görling and H.P. Steinrück, J. Phys. Chem. Lett. **2** (2011) 759.

[109] J. Xu, P. Krüger, C.R. Natoli, K. Hayakawa, Z. Wu and K. Hatada, Phys. Rev. B **92** (2015) 125408.